

# **Preparation and characterization of sulfated zirconia catalysts**

vorgelegt von  
Diplom Ingenieurin (Angewandte Mineralogie)  
Nicole Giliard  
aus Berlin

Von der Fakultät II - Mathematik und Naturwissenschaften  
der Technischen Universität Berlin  
zur Erlangung des akademischen Grades  
Doktor der Ingenieurwissenschaften  
Dr.-Ing.

genehmigte Dissertation

Promotionsausschuss:

Vorsitzender: Prof. Dr. rer. nat. R. Schomäcker

1. Gutachter: Prof. Dr. rer. nat. R. Schlögl

2. Gutachter: Prof. Dr. rer. nat. M. Lerch

3. Gutachter: PD Dr. habil T. Schedel-Niedrig

Tag der wissenschaftlichen Aussprache: 28.01.2011

Berlin 2011

D 83





## Zusammenfassung

Motiviert durch die Hypothese, dass die katalytische Aktivität von sulfatiertem Zirkoniumdioxid (SZ) wesentlich durch Defekte in der tetragonalen Struktur beeinflusst wird, verwendet diese Studie die *n*-Butanisomerisierung als Modellsystem um den Einfluss von strukturellen Imperfektionen im Material auf seine Eigenschaften, katalytische Wirksamkeit und Langzeitstabilität zu untersuchen. Dabei werden Defekte als hochenergetische Plätze auf der Katalysatoroberfläche als Voraussetzung für die Bildung von aktiven Zentren angesehen. Es wird vermutet, dass sich diese Zentren aus einer Kombination von Oberflächendefekten und nahegelegenen Disulfatgruppen zusammensetzen.

Die Präparation und, im Besonderen, die Calcinierung wurden systematisch untersucht. Die chemischen Eigenschaften wurden graduell variiert durch den Promoter Gehalt (Thulium) in der Struktur durch automatische Co-Fällung und der Sulfatgehalt auf der Katalysatoroberfläche durch eine nachfolgende "incipient wetness"-Imprägnierung. Die Proben wurden durch Stickstoffadsorptionsisothermen, Röntgenstrukturverfeinerung, SEM, EDX, TEM, HRTEM, IR UV-vis und *n*-Butanisomerisierung charakterisiert. Zusätzliche Methoden wurden für das untersuchte System neu angepasst: für die Bestimmung der Defektdichte (Kombination von TEM und XRD), für das Verhältnis von Lewis- zu Brønsted-sauren Zentren (L/B Verhältnis) (CO-Adsorption und IR-Spektroskopie) und für die Langzeitdesaktivierungskonstante.

Die untersuchten Katalysatoren zeigen hohe Aktivitäten, aber selbst nach 250 h noch keinen stationären Zustand. Sie konnte mit einer linearisierten Form einer Deaktivierungskinetik zweiter Ordnung beschrieben werden, welche nach der Initialisierung der Reaktion mit genauen Konstanten für die Desaktivierungsrate bestimmt werden konnten.

Intrinsische Defekte in der tetragonalen Struktur – und nicht, wie bisher gedacht, die tetragonale Phase selbst – bestimmen die Oberflächeneigenschaften eines aktiven SZ-Katalysators und damit seine katalytische Wirksamkeit in der Isomerisierung von leichten Alkanen. Die Defektdichte im tetragonalen Gitter, wie auch die Isolierung der dieser Phase selbst, können durch kontrollierte Präparation und Calcinierung gesteuert werden.

Eine stabilisierte Defektstruktur sowie ein besonders niedriges Verhältnis von Lewis- zu Brønsted-Säurezentren auf der Katalysatoroberfläche sind der Schlüssel zu leistungsstarken SZ-Katalysatoren. Mit diesem Wissen können nun gezielt SZ-Katalysatoren mit definiert eingestellten Volumen- und Oberflächeneigenschaften für industrielle Anwendungen synthetisiert werden.



## Abstract

Motivated by the hypothesis that catalytic activity of sulfated zirconia (SZ) is essentially governed by defects in the materials tetragonal structure, this study uses the *n*-butane isomerization as a model system to analyze the effect of structural imperfections of the material on its properties, catalytic performance, and long term stability. Defects, as high energy sites on the catalyst surface, are considered as a prerequisite for the formation of active centers. These centers are thought to be composed of a combination of surface defects and nearby closely spaced disulfate groups.

The preparation and, in particular, the calcination were investigated systematically. The chemical properties were varied gradually through the promoter content (thulium) inside the structure with automated co-precipitation and the sulfate content on the catalyst's surface with a subsequent incipient wetness impregnation. The samples were characterized by nitrogen adsorption isotherms, XRD refinement, SEM, EDX, TEM, HRTEM, IR, UV-vis, and *n*-butane isomerization. Additionally, characterization methods newly for the system adapted were used: for the relative apparent defect density (combination of TEM and XRD), for the Lewis to Brønsted acid site (L/B) ratio (CO adsorption and IR spectroscopy), and for the long term deactivation rate constant.

The investigated catalysts are highly active but do not show a steady state even after 250 h. It could be characterized with a linearized form of a second order deactivation model starting after the initialization of the reaction, from which precise deactivation rate constants could be determined.

It was found that intrinsic defects in the tetragonal structure and not the structure itself determine the surface properties of an active SZ catalyst, and-, accordingly, its catalytic performance and stability in the isomerization of light alkanes is controlled by lattice imperfections. The defect density inside the tetragonal lattice, as well as side isolation of this phase, can be governed by controlled preparation and calcination.

A stabilized defect structure together with a low L/B ratio of surface acid sites are the key features of high-performance SZ catalysts. This knowledge can be used to tune-, and tailor highly active catalysts with specifically desired bulk and surface characteristics for industrial applications.



# Table of Contents

<b>List of Figures</b>	<b>iii</b>
<b>List of Tables</b>	<b>viii</b>
<b>List of Abbreviations</b>	<b>xi</b>
<b>1. Introduction</b>	<b>1</b>
1.1. Outline of the work . . . . .	1
1.2. Zirconia structure . . . . .	2
1.3. Defects in zirconia . . . . .	4
1.4. Role of the zirconia phase for catalytic activity . . . . .	4
1.5. Control of defect type and concentration . . . . .	6
1.5.1. Calcination . . . . .	6
1.5.2. Role of metal promoters . . . . .	8
1.6. Surface properties of SZ . . . . .	11
1.7. Deactivation . . . . .	13
<b>2. Methodology</b>	<b>15</b>
2.1. Nitrogen adsorption-desorption . . . . .	15
2.1.1. Pore size analysis . . . . .	16
2.1.2. BET surface area . . . . .	17
2.2. X-ray diffraction . . . . .	17
2.2.1. Rietveld refinement . . . . .	18
2.2.2. Diffraction line profile analysis . . . . .	19
2.2.3. New method of the determination of the apparent faulting probability in SZ . . . . .	20
2.2.4. Variance method . . . . .	21
2.3. Electron microscopy . . . . .	22
2.3.1. Transmission electron microscopy . . . . .	23
2.3.2. Scanning electron microscopy . . . . .	23
2.4. Determination of sulfate content . . . . .	23
2.4.1. Thermogravimetry analysis . . . . .	23
2.4.2. Ion chromatography . . . . .	25
2.5. Gas chromatography . . . . .	25

## Table of Contents

---

2.6. Infrared spectroscopy . . . . .	26
2.6.1. New method of the determination of the relative Lewis/ Brønsted ratio . . . . .	27
2.7. Determination of the long term deactivation rate constant . . . . .	29
<b>3. Experimental</b>	<b>33</b>
3.1. Catalyst preparation . . . . .	33
3.1.1. Unpromoted sulfated zirconia . . . . .	33
3.1.2. Promoted sulfated zirconia . . . . .	34
3.2. Catalyst calcination . . . . .	35
3.2.1. Calcination in a vertical tubular furnace . . . . .	35
3.2.2. Calcination in a horizontal rocking furnace . . . . .	36
3.3. Catalyst storage conditions . . . . .	38
3.4. Catalyst characterization . . . . .	39
3.4.1. Determination of sulfate content . . . . .	39
3.4.2. BET . . . . .	39
3.4.3. XRD . . . . .	39
3.4.4. Transmission FTIR spectroscopy/CO adsorption . . . . .	40
3.4.5. Electron microscopy . . . . .	41
3.5. Isomerization of <i>n</i> -butane . . . . .	42
<b>4. Catalyst aging</b>	<b>47</b>
4.1. Results and Discussion . . . . .	47
4.2. Conclusion . . . . .	51
<b>5. The evolution of an active catalyst material in the course of thermal treatment</b>	<b>53</b>
5.1. Results and discussion . . . . .	54
5.2. Conclusion . . . . .	59
<b>6. Optimization of the calcination procedure</b>	<b>61</b>
6.1. Results and discussion . . . . .	62
6.1.1. <i>n</i> -Butane isomerization . . . . .	62
6.1.2. Determination of the BET surface area . . . . .	64
6.1.3. Determination of the sulfate content . . . . .	65
6.1.4. SEM results . . . . .	65
6.1.5. XRD and TEM analysis . . . . .	67
6.1.6. Determination of relative L/B-ratios . . . . .	70
6.2. Conclusion . . . . .	73

<b>7. Influence of gas phase loading during thermal treatment of unpromoted SZ</b>	<b>77</b>
7.1. Results and discussion . . . . .	77
7.1.1. Catalytic results . . . . .	77
7.1.2. Sulfate loading and BET surface area . . . . .	79
7.1.3. SEM results . . . . .	81
7.1.4. CO adsorption on post-treatment SZ samples at -196°C . . .	82
7.2. Conclusion . . . . .	84
<b>8. Effect of promoters and sulfate content on catalytic performance</b>	<b>85</b>
8.1. Results and discussion . . . . .	86
8.1.1. <i>n</i> -Butane isomerization . . . . .	87
8.1.2. Nitrogen adsorption isotherm . . . . .	89
8.1.3. SEM . . . . .	93
8.1.4. XRD analysis . . . . .	96
8.1.5. TEM particle size determination . . . . .	100
8.1.6. Determination of the Lewis and Brønsted acid sites . . . . .	106
8.2. Conclusion . . . . .	111
<b>9. Final conclusion</b>	<b>115</b>
<b>10. Outlook</b>	<b>121</b>
<b>A. Appendix</b>	<b>123</b>
A.1. Tables of the deactivation properties . . . . .	123
A.2. Tables of the determination of the sulfate content . . . . .	124
A.3. Aging-correction . . . . .	125
A.4. Figures of sulfate series of promoted SZ . . . . .	126
A.5. Identification of the samples . . . . .	130





# List of Figures

2.1. Nitrogen adsorption-desorption isotherm of unpromoted SZ. . . . .	16
2.2. Sketch of Bragg diffraction from a crystal lattice. . . . .	18
2.3. Powder X-ray diffraction pattern of tetragonal unpromoted SZ. . . . .	19
2.4. Interaction between primary electrons and the sample in electron microscopy. . . . .	22
2.5. Thermal analysis of SZ showing the weight loss which is attributed to sulfate. . . . .	24
2.6. Deconvolution of IR peaks . . . . .	28
2.7. Test for first-order deactivation kinetics . . . . .	30
2.8. Test for second-order deactivation kinetics . . . . .	31
2.9. Measured versus calculated rate of isobutane formation. . . . .	32
2.10. Measured and calculated rate of isobutane formation versus time. . . . .	32
3.1. (a) Preparation of SZ and TmSZ (b) Co-precipitation and aging in an automated laboratory reactor system ( <i>Mettler-Toledo Labmax</i> ) . . . . .	34
3.2. Conditions of co-precipitation and aging in an automated laboratory reactor system ( <i>Mettler-Toledo Labmax</i> ) . . . . .	35
3.3. Comparison of the two calcination set ups . . . . .	36
3.4. Calcination program for quenching experiments in a vertical tubular furnace . . . . .	37
3.5. Double container technique . . . . .	38
3.6. Linear correlation between the intensity of the bands due to CO adsorption on Brønsted sites and the pellet density . . . . .	41
3.7. Tubular reactor . . . . .	43
3.8. Flow-chart of the experimental set-up . . . . .	44
3.9. Reproducibility test of the catalytic reaction . . . . .	45
4.1. Aging of an SZ sample . . . . .	48
4.2. TG curves of SZ of the gas flow series measured 3 and 12 months after preparation . . . . .	49
4.3. Successful avoidance of catalyst aging . . . . .	50
5.1. Calcination program with indicated points of quenching experiments . . . . .	54
5.2. Development of the BET surface area during calcination . . . . .	55
5.3. Development of the phase composition during calcination . . . . .	55

5.4.	Evolution of lattice parameters during the calcining program . . . .	56
5.5.	Development of the crystalline size during calcination . . . . .	57
5.6.	Evolution of the band gap in SZ during calcination . . . . .	57
5.7.	Evolution of the catalytic performance during calcination . . . . .	58
6.1.	Comparison of the rate of isobutane formation after 20 h with the deactivation rate constant for different conditions during calcination	63
6.2.	Comparison of the BET surface area for different series of varied conditions during calcination . . . . .	64
6.3.	Calcination (a) temperature and (b) time of unpromoted SZ catalysts versus its sulfate content after calcination . . . . .	65
6.4.	SEM images of the endpoints of the different calcination series . . .	66
6.5.	(a) Shaping of XRD lines and (b) increasing TEM grain sizes. . . .	67
6.6.	Particle size distribution in TEM and XRD of the optimized catalyst	68
6.7.	TEM image of the optimized catalyst . . . . .	69
6.8.	Increasing relative amount of Lewis acid sites for increasing calcination temperature . . . . .	70
6.9.	IR difference spectra of CO adsorption on unpromoted SZ at $-196^{\circ}\text{C}$	71
6.10.	Comparison of the relative L/B ratio for different calcination conditions versus the rate of isobutane formation after 20 h. . . . .	73
7.1.	Influence of different gas phase treatment during and after the thermal treatment on the <i>n</i> -butane isomerization of unpromoted SZ samples.	78
7.2.	Influence of different gas phase treatment on the rate of isobutane formation after 20 h on stream and on the deactivation rate constant of unpromoted SZ samples . . . . .	78
7.3.	Influence of increasing surface sulfate content on the BET surface area.	80
7.4.	SEM images for different gas phase treatments during or / and after calcination. . . . .	81
7.5.	L/B ratios for unpromoted SZ samples of the gas saturation series versus their rate of isobutane formation after 20 h . . . . .	82
8.1.	Co-precipitated samples: thulium and sulfate series with their intersection at 2 mol% Tm and 10 wt% sulfate . . . . .	86
8.2.	<i>n</i> -butane isomerization for (a) the Tm series and (b) the sulfate series	87
8.3.	Deactivation rate constants and rates of isobutane formation after 40 h on stream for the Tm and sulfate series . . . . .	88
8.4.	Nitrogen adsorption isotherms of the Tm series . . . . .	89
8.5.	Nitrogen adsorption isotherms of the sulfate series . . . . .	90
8.6.	Total pore volumes and deactivation rate constants for (a) the Tm series, (b) the sulfate series . . . . .	91

8.7. Deactivation rate constant versus total pore volume for (a) for the complete Tm series, (b) for Tm contents between 1-5 mol% . . . . .	92
8.8. Bimodal pore size distribution for (a) the Tm series and (b) the sulfate series . . . . .	92
8.9. SEM images of the Tm series . . . . .	93
8.10. SEM images of the sulfate series . . . . .	94
8.11. Element mapping of 2TmSZ . . . . .	95
8.12. BET surface area and unit cell volume for (a) the Tm series,(b) the sulfate series . . . . .	96
8.13. Mixing parameter $\mu$ of (a) Tm series, (b) sulfate series . . . . .	98
8.14. Full width at half maximum and integral width . . . . .	99
8.15. Comparison of particle sizes derived from TEM and XRD. . . . .	100
8.16. HRTEM images of the 2Tm10SZ sample displaying different types of crystal lattice imperfections. . . . .	101
8.17. Apparent faulting probability for the (a) Tm series, (b) sulfate series	102
8.18. Correlation between apparent faulting probability and unit cell volume	103
8.19. Size and strain for increasing Tm content, calculated with the variance method. . . . .	104
8.20. Cottrell atmosphere model applied for Tm in tetragonal sulfated zirconia with Tm migrating to a dislocation line . . . . .	105
8.21. IR difference spectra of CO adsorption on SZ at $-196^{\circ}\text{C}$ illustrating the relevant spectra ranges for the determination of Lewis and Brønsted acid sites. . . . .	106
8.22. Individual investigated pressures for the Tm series . . . . .	107
8.23. CO adsorption on 2TmSZ . . . . .	108
8.24. Concentration of Lewis and Brønsted acids sites versus Tm content	109
8.25. Correlation between bulk and surface properties . . . . .	110
8.26. Correlation between surface properties and deactivation rate constants	111
9.1. Model for Tm promoted SZ . . . . .	118
A.1. Corrections for catalyst aging of catalysts which were often in use .	125
A.2. Relative L/B ratios for all investigated SZ samples of the calcination and gas series before and after aging corrections . . . . .	126
A.3. Standard deviations of the particle size determined by TEM analysis (a) Tm series, (b) sulfate series . . . . .	126
A.4. Saturation of adsorbed CO for (a) the Tm series,(b) sulfate series up to the highest investigated CO partial pressure. . . . .	127
A.5. Integrated peak areas for increasing pressure of CO adsorption on samples with varied sulfate contents. . . . .	127
A.6. Concentration of Lewis and Brønsted acids sites versus sulfate content	128
A.7. Correlation between bulk and surface properties . . . . .	129

A.8. Correlation between surface properties and deactivation rate constants	129
---	-----

# List of Tables

6.1. Varied parameters . . . . .	62
6.2. Deactivation: temperature series . . . . .	69
6.3. Sample properties: time series . . . . .	69
7.1. Influence of the hydration state on BET surface area and sulfate content . . . . .	80
A.1. Deactivation: gas flow series . . . . .	123
A.2. Sample properties: oxygen partial pressure series . . . . .	123
A.3. Varied parameters . . . . .	124
A.4. Varied parameters . . . . .	124
A.5. Evolution . . . . .	130
A.6. Optimization: temperature series . . . . .	130
A.7. Optimization: time series . . . . .	130
A.8. Optimization: oxygen partial pressure series . . . . .	131
A.9. Optimization: gas flow series . . . . .	131
A.10. Gas saturation . . . . .	131
A.11. Promoter Series . . . . .	132
A.12. Sulfate series . . . . .	132



# List of Abbreviations

**BET** adsorption isotherm model of Brunauer, Emmet and Teller

**EDX** energy dispersive X-ray spectroscopy

**fcc** face centered cubic

**HRTEM** high resolution transmission electron microscopy

**IC** Ion chromatography

**IR** infrared

**KF** Kleinflansch

**L/B ratio** Lewis-Brønsted ratio

**REE** rare earth elements

**SEM** scanning electron microscopy

**SZ** sulfated zirconia

**TEM** transmission electron microscopy

**TGA** thermogravimetry analysis

**XRD** X-ray diffraction





# 1. Introduction

## 1.1. Outline of the work

Sulfated zirconia (SZ) is a solid catalyst for the isomerization of straight chain alkanes into their branched isomers. In this study the isomerization was used as test reaction to test the influence of defects in the structure of the catalyst on the materials properties and the catalytic performance. This reaction is catalyzed by acidic sites on the surface of the material. Among solid acids, SZ systems attract considerable interest because they are environmentally friendly, highly active and quite selective for the transformation of hydrocarbons. SZ has been shown to be very active for *n*-butane isomerization at low temperatures between 50-100 °C [1]. Holm and Baily[2], in 1962, found that platinum-containing sulfate-treated zirconia gel exhibits a higher catalytic performance compared to commercial Pt/chlorided alumina. The skeletal isomerization is interesting because alkanes are not very reactive molecules and the thermodynamic equilibrium becomes even less favorable at higher temperatures. The transformation of *n*-butane into *iso*-butane is thermodynamically favored at low temperatures up to 220 °C. In 1979 and 1980, Hino and Arata showed that the isomerization of *n*-butane over SZ is possible at room temperature [3, 4]. Since butane is extremely difficult to isomerize, Hino and Arata's findings led to a great interest in SZ. Addition of a promoter to SZ often leads to a very high initial activity of the catalyst. This high activity is often followed by rapid deactivation. Tungstated zirconia was tested as an alternative to SZ due to its superior stability under reducing and oxidizing conditions, but its activity is not satisfying compared to SZ [5].

After more than 30 years of research into the mechanism for the industrially important skeletal isomerization, the structure-activity relationship for sulfated zirconia is not well understood. The aim of the present work was to find a relationship

between material properties and catalytic performance. Emphasis was put on the investigation of the influence of defects in the material's structure on the catalyst's properties. Similar investigations were done before for copper and mixed metal oxides. For Cu/ZnO/Al catalysts, which are used for methanol synthesis, the catalytic activity is proportional to the abundance of non-equilibrium structures in Cu, such as planar defect (twins and stacking faults) and strain [6]. Recently it was reported for M1 phase MoVTaNbOx catalysts that special assemblies of metal-oxo clusters in the M1 structure are responsible for the activity in the partial oxidation to acrylic acid [7, 8]. As the size and shape of the needles define the quantity of the assemblies exposed to the catalyst's surface, the catalytic activity depends on the morphology of the M1 needles. Methodical knowledge of these studies was used to investigate the properties of SZ catalysts in the present study.

The development of the active phase during catalyst synthesis was investigated by variation of the thermal heat treatment program and quenching experiments during this program. Defect concentration was modified by variation of the preparation technique, the calcination program, and by the addition of a promoter (Tm). The impact of bulk and surface modifications was investigated. Activities were measured with a three channel sand bed flow reactor at atmospheric pressure. Modifications in the bulk structure were investigated by XRD, SEM and TEM. Surface modifications were detected by BET measurements, IR spectroscopy and desorption measurements.

## 1.2. Zirconia structure

Under standard conditions, zirconia crystallizes in a monoclinic baddeleyite structure (space group  $P2_1/c$ ), a distorted fluorite type with a sevenfold coordinated zirconium. At temperatures between 1170 °C and 2370 °C, zirconia exists in a distorted tetragonal form (space group  $P4_2/nmc$ ) with a coordination number between seven and eight. At even higher temperatures towards the melting point at about 2680 °C zirconia crystallizes in a well-defined cubic fluorite structure (space group  $Fm3m$ ) with eightfold coordinated zirconium. Furthermore, an orthorhombic high temperature modification is known.

In the cubic fluorite structure, zirconium atoms are ideally surrounded by eight oxygen atoms. The distances between the zirconium and the oxygen atoms are

different in the tetragonal structure. In an undistorted tetragonal zirconia lattice, the two types of oxygen bonds are crystallographically equivalent. However, the outer oxygen atoms show lower vibrational frequencies and greater levels of distortion for the Zr-O and Zr-Zr bonds, which means that the outer oxygen atoms are less strongly bonded than the inner ones [9]. Four of the Zr-O distances increase, whereas they are shortened for the remaining four Zr-O bonds. X-ray studies conducted on SZ and Y-stabilized zirconia have shown that interatomic distances, coordination number, and phase stability in the different modifications have an important influence on the observed distortions. The level of distortion defines, inter alia, the level of defect density in a crystalline structure. The tetragonal zirconia cation network shows the softest vibrational frequency of all modifications, despite the short bond lengths, reflecting phase instability [9]. Instable phases are often rich in defects. For catalytic reactions zirconia is needed in the tetragonal phase at low temperatures, since fully monoclinic catalysts have no meaningful activity level in *n*-butane isomerization [10], which is the reaction of interest in the present work. The high temperature phases are normally not quenchable; only particles smaller than 30 nm are quenchable [11]. For these small particles, the tetragonal phase can be stabilized [11]. Different aspects are discussed in the literature in order to describe the inhibition of the phase transformation from the tetragonal phase to the monoclinic one: surface strain energy effects [11], stabilization by OH groups, structural similarities between an amorphous precursor phase and the tetragonal phase [12], stabilization by oxygen vacancies [13]. The tetragonal or cubic structure can be produced as metastable phases for small particles by using special calcination conditions, by using silica or alumina as supporting materials [14, 15], or by addition of cations (di-, tri- and tetravalent). For example, oversized  $\text{Ce}^{4+}$  and undersized  $\text{Ge}^{4+}$  tetravalent dopants have significantly different oxygen coordinations from that of the host cation. Ce forms a random substitutional solid solution with Zr, while Ge dissolves in the cation sublattice but is arranged in ordered domains [14].

Hence, catalytic active systems made out of nanometer-sized particles cannot be compared to a stable crystalline tetragonal zirconia system with impurities, because this stable system would be a high temperature system in which defects would tend to heal.

### 1.3. Defects in zirconia

Defects in zirconia play an important role in industrial applications; examples are oxygen ion conducting solid electrolytes in fuel cells or sensors like the lambda probe in cars. For this purpose, it is important that there exist oxygen vacancies in the crystal lattice, so that ions are able to move through the lattice. In materials which are used for industrial purpose this is achieved by doping the zirconia with cations like  $\text{Mg}^{2+}$ ,  $\text{Ca}^{2+}$  or  $\text{Y}^{3+}$ , which makes it possible to stabilize high temperature phases (tetragonal or cubic). The concentration and distribution of the oxygen vacancies is an important factor for the stabilization of high temperature phases, phase transformation temperatures, and physical properties [9]. As a function of substituent concentration, these so-called stabilized zirconias usually show a conductivity maximum at the low substitution side of the cubic phase field for an anion defect concentration of about 5% [16]. Nowadays, the materials that are technically used are mainly those with a doping content of up to 15 mol%.

### 1.4. Role of the zirconia phase for catalytic activity

Defects play a key role in catalysis because the surface of a crystal itself can be regarded as a defect, and because catalytic reactions take place on surfaces. Provided that defects play an important role in the isomerization of *n*-butane, they should mainly be found in the tetragonal, or cubic, phase of  $\text{ZrO}_2$ , which are metastable at room temperature. The tetragonal phase is very active in the isomerization of *n*-butane, in contrast to the low temperature stable monoclinic phase. According to Klose et al. [17], monoclinization of an active tetragonal catalyst by physical treatments, like milling, leads to serious declines in catalytic activity. Another structural aspect is that the higher density of tetragonal to monoclinic zirconia results in higher volume based activity for the tetragonal systems provided that the weight based activities are similar. Several authors stated that the stabilization of the tetragonal phase is a result of defects in the crystalline structure of the catalyst and that, with the transformation of the catalyst to the monoclinic phase, the number of defects decreases: Vera et al. [10] remarked that the presence of the tetragonal phase is a consequence of the stabilization of anionic vacancies. They believed that during a calcination procedure in air, surface sulfate groups would

prevent oxygen from diffusing into the lattice, so that defects would remain at or near the surface. Srinivasan et al. [18] claimed that when the surface loses sulfate in form of  $\text{SO}_3$ , the transformation to the monoclinic phase starts from surface to bulk material. Bobricheva et al. [19] observed that the transformation of the tetragonal to the monoclinic phase of  $\text{ZrO}_2$  entails a decrease in the concentration of F-centers. F-centers (color centers) are defects in which an anionic vacancy in a crystal is filled by one or more electrons.

Vacancies in the outer layers of the crystal can be caused either by charge compensation or by distortion in the network imposed by size effects. The presence of vacancies lowers the average coordination number of Zr and therefore favors the tetragonal structure. As a consequence, catalytic activity should be related to anionic vacancies and not to the tetragonal structure itself [10]. Vera and Shimizu [20] prepared a completely tetragonal SZ with no catalytic activity for the isomerization of *n*-butane. Boyse et al. [21] showed how  $\text{SiO}_2$  doping of  $\text{WO}_x\text{-ZrO}_2$  catalysts enhanced the stability of the tetragonal phase and increased the surface area of the sample but decreased its activity.

Besides the structural properties, surface properties play a key role for the catalytic activity of SZ. Nascimento et al. [22] claimed for unpromoted SZ that couples of Lewis and Brønsted acid sites are necessary for catalytic activity in the *n*-butane isomerization. Lewis acidity is attributed to coordinatively unsaturated  $\text{Zr}^{4+}$  ions located in defective surface sites, whereas Brønsted acidity is associated with surface sulfate groups. Cerrato et al. [23] suggested that an optimum ratio of Lewis and Brønsted acid sites is relevant for catalytic activity. Defects and neighboring sulfate groups seem to be interdependent and influenced by the preparation of the catalyst. Impurities and little changes to the preparation procedure may yield different catalysts and therefore may deliver unrelated analytical data. For example, if the sulfate content is changed, surface area and phase composition [24], namely the ratio of tetragonal to monoclinic phase and therewith the defect concentration is changed. That explains why reproducibility of the material is poor and careful preparation is very important.

To sum up what has been said so far, we know that not all tetragonal SZ samples are highly active. Our working hypothesis is that defects play a key role in the isomerization of straight-chain alkanes. Only the combination of defects and neighboring sulfate groups seems to result in an active catalyst.

## 1.5. Control of defect type and concentration

In the present work, different ways of controlling of defect type and concentration will be evaluated: variation of the calcination conditions and variation of the promoter content.

### 1.5.1. Calcination

Calcination is the final step in the catalyst preparation. In the IUPAC Compendium of Chemical Terminology, calcination is defined as “heating in air or oxygen”; the term is most likely to be applied to a step in the preparation of a catalyst“. In the present work, this definition is understood in a broader sense in order to include heat treatment in argon. Many processes which are important for the definition of the final product already appear while the raw material is heated to the appropriated calcination temperature. These processes are: water loss, decomposition of precursor species (ammonium, nitrates), crystallization and sintering. The sulfate in the bulk of amorphous precursor material is expelled onto the surface of SZ during crystallization. This process is linked to sulfate loss and some dehydroxylation [25]. Comelli et al. [26] stated that the presence of crystalline structure and sulfur were not sufficient to produce an active material. Consequently, the calcination step modifies the surface species of the solid, thereby improving its catalytic properties.

Water plays an important role during the calcination procedure. According to Norman et al. [27], the transformation of a hydroxide to a crystalline oxide can be divided into three steps:

1. Dehydration and loss of terminal hydroxyl groups
2. Oxolation of OH bridges and formation of oxide nuclei
3. Growth of the nuclei

They proposed that at a high water pressure, water loss through oxolation is favorable and fewer oxide nuclides are formed. Hahn et al. [28] found that, since water evaporates early on, this fact should affect nucleation but not growth. In general, water limits nucleation and improves diffusion processes. Therefore, it often leads to fewer but larger particles. Murase and Kato [29] found water vapor to increase surface diffusion and to enhance crystallite growth for pure zirconia. Li

et al. [30] found water steam during the calcination procedure to be negative for the catalytic activity. They believed that water and  $\text{SO}_3$  compete for adsorption sites on the surface of SZ during calcination [30]. Cerrato et al. [23] found a dependency between couples of Lewis and Brønsted acid sites which are needed for catalytic activity, and dehydration rates during calcination. They claimed that the water content is optimal when the catalyst is brought to a intermediate level of dehydration. It is noteworthy that SZ loses only part of its surface hydroxyl groups during calcination [31].

Highly active SZ catalysts are produced in a small temperature range in order to form crystalline samples consisting of 100% tetragonal structures. Above this range, the fraction of monoclinic phase increases. For promoted samples at a calcination temperature of  $720^\circ\text{C}$ , the amount of sulfate on the catalyst surface decreased dramatically [32]. Temperatures lower than  $350^\circ\text{C}$  lead to amorphous, fully hydroxylated  $\text{Zr}(\text{OH})_4$  samples [10], [12]. A maximum defect concentration of  $\text{Zr}^{3+}$  is to be found at a calcination temperature of about  $550^\circ\text{C}$  for pure  $\text{ZrO}_2$  [33].

Most authors keep the sample at the calcination temperature for 3 h, but it has not yet been proven that this is really necessary. According to Hahn et al. [28], all important steps that are necessary to create an active catalyst are finished after the glow phenomenon. The glow phenomenon is an exothermic reaction which can lead to visible light emission - hence the name - and which is typical of calcination during heating period of SZ. Between  $480 - 630^\circ\text{C}$ , a spontaneous overheating of the sample bed is possible. The rapid temperature change outside a thermodynamic equilibrium allows for the chemical conditions to be reflected in the final catalyst. It is during the "glow effect" within a few minutes of temperature overshoot, that the metastable crystalline phase with active surface sites is built up. Thus, there is no time within the "glow effect" to form a well ordered structure. Hence, the glow effect could be said to control for the defect concentration. Three reactions could account for the temperature overshoot: decrease in the surface energy for the transition from amorphous to tetragonal zirconia with an energy difference of  $\sim 1.19 \pm 0.08 \text{ Jm}^{-2}$  [12], crystallization heat, or loss of surface area [28]. Since surface area loss is a consequence of crystallization, it is more likely that crystallization is what is mainly responsible for the temperature overshoot. Different parameters, such as batch size, are crucial for the heat transfer. These parameters influence the extent of the temperature overshoot and the oven temperature at which the overheating

of the sample bed is observed. The promoters Mn or Fe, for example, can lead to a temperature overshoot of up to 200 °C. During the glow phenomenon, heating rates of up to 60 °C min<sup>-1</sup> were measured [34]. Hahn et al. [34] found a significantly higher maximum conversion for samples calcined in a large bed than for samples taken from smaller batches. Li et al. [30] found that calcination in a shallow bed leads to a lower sulfate content and to a completely inactive sample.

### 1.5.2. Role of metal promoters

The role of metal promoters in the catalytic activity of sulfated zirconia is still unclear. Hsu et al. [35–37] were the first to report that SZ promoted with Fe and Mn exhibits significantly higher catalytic activity than unpromoted catalysts. Subsequently, many other groups confirmed the enhanced activity for promoted catalysts. Enhanced *n*-butane isomerization activities were found for: Fe, Mn, Zn, Ni, Co, Pt, W, Cr, Ni, Ti, Ga, Al, Sn, V, Mo, Re [4, 32, 38–43]. Yori and Parera [40] reported an inhibiting effect of Cu for *n*-butane isomerization, whereas Miao et al. [41] reported inhibiting effects of Mn, Sn, W and Mo.

In spite of all these findings, no consensus has yet been obtained about the role of promoters for increased catalytic activity. Different modes of operation for promoters are referred to in the literature:

- retardation of crystallization [23, 32]
- enhancement of tetragonal stability [44], of the intrinsic turnover frequency [45], and of the oxidizing ability of sulfate [32, 46]
- delay of the thermal decomposition of sulfate [32, 47]
- prevention of the coalescence of particles [28], increase of the surface area and amount of sulfates retained after calcination [23, 32]
- creation of defects [33, 48]
- control of the relative amount of oxygen deficiency [49]
- balance of distribution of Lewis and Brønsted acid sites [49]
- increase the number of active sites [42]



Due to investigative difficulties, it is still being discussed which individual cations are better promoters than others, where they are located, and which state they are in. It has already been understood that promoters have a systematic influence on the end product: They alter the chemical conditions during the calcination procedure and, by consequence, the final bulk and surface structure as well. It is noteworthy that the addition of promoters does not affect the acid strength. Adeeva et al. [50] used IR spectroscopy of adsorbed probe molecules, in order to evaluate the catalyst's surface acidity and concluded that promoted and unpromoted SZ catalysts have about the same Lewis and Brønsted acidity.

Both initial and the steady state activity of a catalyst depend on the promoter loading. The optimum promoter content is between 2 – 5 mol% [32]. N<sub>2</sub> adsorption, XRD, Raman spectroscopy, and TEM showed that the amorphous phase increases and the surface area decreases when the promoter content rises above 5 mol%. With increasing Ga<sub>2</sub>O<sub>3</sub> loadings, the typical spectral features of surface sulfates were observed, but they became more and more blurred [32]. Wang et al. [51] explained that an excessive amount of promoter on the SZ surface, may cover it and reduce the number of active sites.

#### **Location of the promoter**

The location of promoters is difficult to analyze and seems to depend on the choice of the promoter. Until now it remains to be unclear whether the promoter influence is produced indirect through lattice distortion changing atom distances, making the surface more easily accessible for sulfate groups, and creating oxygen vacancies in the bulk and therefore at the surface –, or directly by promoters on or near the surface – creating oxygen vacancies directly on the surface by local charge balance. Jentoft et al. [52] concluded from XRD, EPR, ISS and XANES data for the promoters Fe and Mn, that Fe and Mn were partly incorporated into the zirconia lattice. In a typical catalyst containing about 2 wt% of promoter metal, only Fe but no Mn was found at the surface. This indicated that a higher fraction of Mn was incorporated into the lattice than Fe. With increasing promoter content the cell volume of the Mn and Fe-promoted sample increased. Furthermore, the same authors compared the influence of the promoters Mn and Fe on the transformation of SZ. The amount of transformed crystallites and the loss of activity were higher for FeSZ than for

MnSZ [53]. Gillespie and Cohn [54] found for industrial purpose that rare earth elements (REE) promoted catalysts were more active in light alkanes conversion compared to often investigated Mn/Fe promoted catalysts and gave hints that REE elements were introduced into the tetragonal lattice of SZ. They showed a linear dependence relation between the pentane conversion over REE promoted SZ and the ionic radius, with the conversion increasing almost linearly for increasing ionic radii with a maximum for heavy REE with a ionic radius up to 115 ppm. Above 115 ppm the conversion dropped rapidly [54].

### Structural explanations for the promoting effect

As mentioned above, promoters help to stabilize the tetragonal phase and could be responsible for the creation of oxygen vacancies. This could be a very useful explanation for one side of the promoting effect of lower valent cations in the zirconia lattice. These lower valent promoter cations produce oxygen vacancies in the lattice and near the surface; such defects are equivalent to surface cations with a high degree of unsaturation. Frolova and Ivanoskaya [33] investigated the  $\text{ZrO}_2\text{--GeO}_2$  system from a ceramic point of view with  $\text{GeO}_2$  contents between 5 – 50 mol% with EPR, which is a useful method to monitor point defects on material surfaces. The intensity of signals, which is characteristic for paramagnetic centres, depended on the germanium content and calcination temperature. The concentration of paramagnetic centres reached its maximum at calcination temperatures between 500 and 600 °C (ca.  $10^{18} \text{ g}^{-1}$ ). For samples calcined at 600 °C the intensity of  $\text{Zr}^{3+}$ -centres increased with increasing Ge content and reached its maximum at 30 mol%. The authors explained the effect of Ge in the binary system  $\text{ZrO}_2\text{--GeO}_2$  with the big difference in the ionic radii, i.e. 0.082 nm for  $\text{Zr}^{4+}$  versus 0.044 nm for  $\text{Ge}^{4+}$ . Any substitution in this system caused strong lattice deformation. This deformation could be compensated for by efficient oxygen vacancy formation [33]. It should to be noteted that the investigated dopants differ contentwise from promoters usually used in catalysis. But it appears that different effects like charge balance due to lower valent dopants and differences in ionic radii between crystal ions and dopants, the latter of which are known to lead to defect formation, play a role when a promoter is introduced into a crystal lattice. Hence, it is important that defects

are created by introducing promoters into the SZ lattice but it is possible that the exact way they are introduced plays less of a role in this context.

## 1.6. Surface properties of SZ

Only liquid superacids like  $\text{FSO}_3\text{H}-\text{SbF}_5$  or  $\text{HF}-\text{SbF}_5$  can isomerize *n*-butane at room temperature [55]. Because SZ has the same capacity, it was for a long time believed to be superacidic [3, 4]. Superacids are, according to Gillespie [56], acids exceeding the strength of 100 % sulfuric acid. Normally, superacidity is measured by using Hammett indicators. Recent studies using NMR [57], UV-Vis [58], IR spectroscopy [59], and theoretical calculations [60] have shown that the acidity of SZ is not stronger than that of sulfuric acid. Direct correlations between the catalytic performance of SZ and its acidity are not consistent across the literature [61]. The techniques used to evaluate the acidity of SZ often suffer from experimental problems, such as reaction rather than desorption during temperature-programmed methods.

Based on DFT calculations, Haase and Sauer [31] found that the surface of pure zirconia is a strong base and that therefore, sulfuric acid completely dissociates on the zirconia surface, resulting in a sulfate anion. Sulfate is assumed to be located on the surface [61]. Furthermore, zirconia needs sulfate in order to be useful as active catalyst for skeletal isomerization. Therefore, activity is related to the structure and amount of sulfate. Only 20 % of the sulfate is involved in adsorption of the reactant, and only 2 % function as reaction sites [62]. Sulfate on the surface of SZ is known to have different effects:

- supply of acid reaction sites [62]
- partial reduction in the oxidative dehydrogenation (initiation step of the reaction cycle) [63]
- retardation of crystallization [25]
- retardation of transformation from tetragonal to monoclinic phase [25]
- protection from sintering [64]

Nascimento et al. [22] proposed a correlation between the ratio of Lewis to Brønsted acid sites and the catalytic activity of SZ. Many reports focus on the

identification of different surface acid sites on SZ and show the coexistence of Lewis and Brønsted acid sites on the surface. Lewis acid sites are created by coordinatively unsaturated surface metal ions of zirconium or promoters ( $\text{Zr}^{4+}$  or  $\text{M}^{3+}$ ) located in defective surface sites. Brønsted acid sites consist of hydron-donating OH groups and are associated with surface sulfate groups. It is noteworthy that SZ loses only part of its surface hydroxyl groups during calcination [31]. Lewis [65] as well as Brønsted acid sites [66] or a combination of both [67] have been suggested to be responsible for catalytic activity.

Acidity is described by the type, number, and strength of the acid sites. These quantities can be characterized by adsorption of probe molecules. The type of sites is investigated with IR or NMR, by monitoring the adsorbed species or changes of the adsorbent related to interactions with the adsorbate. Typical probe molecules for probing acid sites are small molecules of different basic strengths, such as ammonia and pyridine, which are able to provide information regarding almost any catalyst acid site; studies with weaker bases such as CO or benzene can be used to selectively probe acidic sites. Pyridine is a frequently used probe because Lewis and Brønsted acid sites can be determined simultaneously and still be distinguished in certain IR bands. The use of pyridine has several disadvantages: The adsorption of pyridine is irreversible and results in a shift in the S=O stretching vibration, a fact which suggests a change in the bonding situation of the sulfate [68]. Furthermore, pyridine is oxidized by a decreased thermal stability of the sulfate [69] and by the metal oxide lattice [70]. Morterra and Cerrato [71] claim that the Lewis sites are overestimated by pyridine due to possible ligand displacing effects of pyridine. CO is another widely used probe molecule. At room temperature only strong Lewis acid sites are probed, while at a low temperature of  $-196^\circ\text{C}$  also weak interactions of Lewis and Brønsted sites are detected. In combination with IR spectroscopy, the perturbation of the CO stretching vibration due to adsorption is monitored. Numerous studies with CO adsorption could not explain the role of promoters nor the reason for catalytic activity of SZ at temperatures close to room temperature.

Amount and strength of the adsorbed species are determined by temperature programmed desorption (TPD) or by calorimetry combined with barometric-volumetric measurements to extract differential heats of adsorption. The number of sites for butane oxidative dehydrogenation is thought to be less than  $5\text{ }\mu\text{mol/g}$  [72]. Microcalorimetric experiments proved the interaction with  $\text{C}_3$  and  $\text{C}_4$  alkanes to

be weak for the majorities of sites. Heats of adsorption for *n*-butane were about 45 – 60 kJ/mol. A large number of models surface sulfate structures on SZ can be found in literature. It can be assumed that there is no single sulfate structure but a number of different coexisting interchangeable species [73], which depend on various conditions such as the coverage, degree of hydration [74], pretreatment and measurement atmosphere. Hofmann and Sauer [75] calculated by statistical thermodynamics surface structures of tetragonal SZ for different temperatures and pressures and found that only mono- and disulfates (pyrosulfate,  $\text{S}_2\text{O}_7^{-2}$ ), but no highly condensated sulfates may occur. Recent experimental findings, have shown that active catalysts possess an IR band at  $1404\text{ cm}^{-1}$ , which is ascribed to S=O bond stretching vibrations in disulfate or adsorbed  $\text{SO}_3$  molecules [63]. The presence of a disulfate species on SZ was first proposed by Bensitel et al. [73]. They observed an IR band at  $1403\text{ cm}^{-1}$  at high sulfate coverages, which disappeared on exposure to water. Morterra et al. [74] suggested that the formation of an IR band at  $1406\text{ cm}^{-1}$  is due to disulfates. Experiments indicated these disulfates to be located on the regular patches of low index crystal planes of the zirconia surface. Increasing the sulfate loading (thus favoring the presence of disulfate species) was shown to increase the number of Brønsted acid sites, whereas lowering the number of Lewis acid sites enhanced their strength. These acidic sites were found to be liable to hydrolysis. Lloyd [76] suggests that the catalytic sites might well be generated from disulfate species, but that their catalytic activities depend on their environment rather than their total concentration.

## 1.7. Deactivation

All unpromoted and promoted SZ catalysts suffer from fast deactivation. Several mechanisms for deactivation will be discussed here:

1. formation of allylic and polyenylic cations and polycyclic aromatic compounds (coke) [77–79]
2. decay of carbenium ion species [72] (a reaction intermediate)
3. reduction of  $\text{S}^{6+}$  of surface sulfate groups to lower oxidation states [61] and chemical decomposition of sulfate groups [63], like disulfates

4. removal of sulfur in case of reduction to a volatile product [61]
5. sulfur migration into the bulk [61]
6. poisoning by water [77]
7. zirconia surface phase monoclinization [80]

Several methods have shown to retard rapid deactivation: promoting the catalyst with Pt [81] and adding H<sub>2</sub> [82] to the feed, as well as filtering out the olefin impurities from the feed [83]. It is worth mentioning that the same factors that enhance the catalytic activity in the initialization step of the reaction also increase the rate of catalyst deactivation at steady state conditions. Consequently, the use of H<sub>2</sub> in the feed stream reduces the rate of catalyst deactivation for *n*-butane isomerization, especially in the presence of Pt as a promoter, but at the same time reduces the catalytic performance [82, 84, 85], whereas no effect on *n*-hexane isomerization has been observed by Tran [84].

It has been shown that the activity of SZ catalysts can be partly regenerated in air or oxygen at 315 – 450 °C [62]. Vaudagna et al. [86] reported that coke deposited during the *n*-hexane reaction decreased the surface area of SZ and PtSZ by blockage of the small-diameter pores. Regeneration, in spite of total coke elimination, did not produce a complete surface area recovery. The authors found that sulfur loss during the reaction also contributed to the decrease in surface area, generating larger pores through the collapse of the smallest ones. A transition from the tetragonal to the monoclinic crystalline phase of the zirconia bulk structure occurred when the sulfur content dropped below a critical value. Coke removal under an oxidative atmosphere was in some cases accompanied by catalyst oxidation [45]. The oxidation treatment regenerates the surface sulfate groups, restores the original bonding configuration with the zirconia surface, and the surface phase is restored, resulting in tetragonal structures [80].

## 2. Methodology

### 2.1. Nitrogen adsorption-desorption

The surface area and its porosity strongly influence the performance of catalytic material. The standard method of determining the specific surface area is the adsorption of nitrogen at  $-196^{\circ}\text{C}$ . Sorption behavior depends on the pore size; the IUPAC gives the following definition for the inner diameter of:

- micropores: inner diameter  $< 2\text{ nm}$
- mesopores: inner diameter  $2 - 50\text{ nm}$
- macropores: inner diameter  $> 50\text{ nm}$ .

On flat surfaces, the size of macropores makes adsorption equal to desorption. In micropores, sorption behavior is mainly governed by the interactions between fluid molecules and pore walls, whereas in mesopores, in addition to the fluid-wall interaction, there also exists an interaction among the fluid molecules in the middle of the pores.

Different isotherms can be found during the adsorption-desorption process. SZ shows a typical type IV isotherm, according to the IUPAC definition, indicating mesoporous material (Fig. 2.1)[87].

The mechanism of filling mesopores can be illustrated with help of Figure 2.1: A mono-molecular layer is formed in section (a), followed by multi-molecular layers in section (b). Capillary condensation starts at a critical film thickness, as shown in (c) section. The following plateau in section (d) originates from completely filled pores with a hemispherical boundary layer. When desorption starts, the boundary layer is bent towards the inside of the pores, thus evaporation takes place at a lower pressure than condensation. In section (f), desorption reappears in multi-molecular and later in mono-molecular layers. The result of the adsorption-desorption process of a

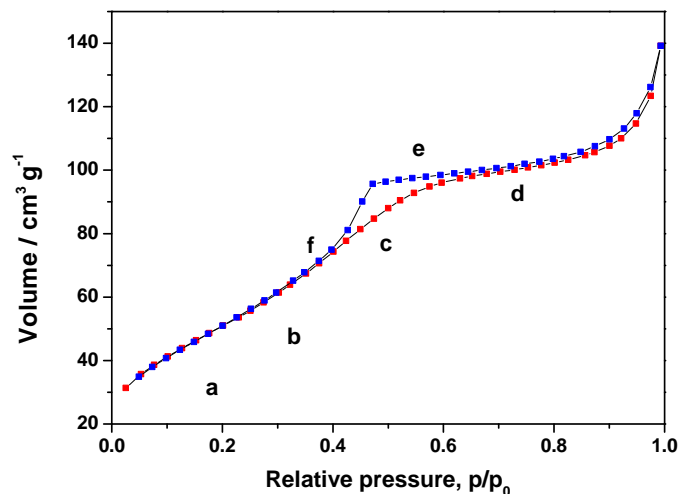


**Figure 2.1.:** Nitrogen adsorption-desorption isotherm of unpromoted SZ which displays a typical type IV isotherm indicating mesoporous material according to the IUPAC definition.

mesoporous material is a hysteresis loop. These hysteresis loops are a consequence of the network structure of the material and are generally observed for corpuscular or particular aggregates [88]. It is related to the occurrence of capillary condensation - a phenomenon during which the low density adsorbate condenses to a liquid-like phase at a chemical potential (or bulk pressure) lower than that corresponding to bulk saturation [89].

### 2.1.1. Pore size analysis

Pore size can be estimated using the nitrogen adsorption-desorption isotherm. For the investigated SZ, one generally uses the BJH method [90], named after Barrett, Joyner and Haleda. Micro- and mesopores can be determined by this method. For their analysis, the assumption is that it is assumed that the pores are cylindrical in shape. The model is based on numerical methods and uses the desorption branch of the nitrogen adsorption-desorption isotherm. Computation starts at a relative pressure of 0.967 down to a relative pressure of approximately 0.4. This means that, pores with a radius greater than 30 nm are ignored [91]. Their number is generally small when compared to the number of smaller pores, hence they do not significantly contribute to the pore size distribution. The BJH method considers an isotherm as a series of steps taking place while the pressure is lowered. The amount



of adsorbate removed in each step is composed of between inner pore emptying from liquid adsorbate and film thinning process.

### 2.1.2. BET surface area

The adsorption isotherm model of Brunauer, Emmet and Teller (BET) [92] is widely used for calculating the surface area. After several numerical transformations, the surface area ( $A$ ) of the adsorbent is given by:

$$A = A_m^{\text{eff}} n_m^s \quad (2.1)$$

where  $A_m^{\text{eff}}$  is the effective area per molecule in a mono-layer and  $n_m^s$  is expressed in units of adsorbent molecules for a mono-layer.

## 2.2. X-ray diffraction

X-ray diffraction (XRD) is a technique widely applied in order to characterize crystalline materials. In catalyst research, XRD is routinely applied for phase identification, quantitative phase analysis, as well as for the determination of size, shape and internal strain of small crystallites. In 1912, Max von Laue discovered that crystalline substances act as three-dimensional diffraction gratings for X-ray wavelengths, similar to the spacing of planes in a crystal lattice. X-ray diffraction occurs by an elastic scattering of X-ray photons on electrons. The interaction of the incident rays with the sample produces constructive interference and a diffracted ray under conditions satisfying Bragg's Law. This law relates the wavelength of electromagnetic radiation to the diffraction angle and the lattice spacing; in a crystalline sample, it is generally used to explain the interference pattern of X-rays scattered by crystals (Eq. 2.2, Fig. 2.2):

$$n\lambda = 2d_{hkl} \sin \theta \quad (2.2)$$

The variable  $d$  stands for the distance between lattice planes ( $hkl$ ) in a crystal; the variable  $\lambda$  is the wavelength of the incident X-ray beam; and  $\theta$  is the angle between the incoming X-rays and the normal to the reflection plane;  $n$  is an integer presenting the diffraction order. These diffracted X-rays may be recorded with photographic

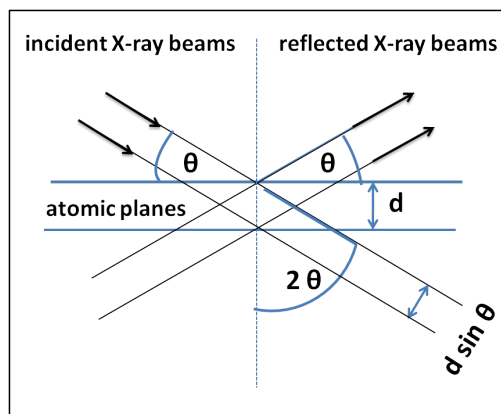


**Figure 2.2.:** Sketch of Bragg diffraction from a crystal lattice. Plane waves incident on a crystal lattice at angle  $\theta$  are partially reflected by successive parallel crystal planes of spacing  $d$ . The superposed reflected waves interfere constructively, if the Bragg condition eq. 2.2 is satisfied.

film, an area detector or with a charge-coupled device (CCD) image sensor. By scanning the sample in a range of  $2\theta$  angles, all possible diffraction directions of the lattice should be attained due to the random orientation in powdered materials. Conversion of the diffraction peaks to  $d$ -spacings allows identification of the crystal phases because each crystal has a set of unique  $d$ -spacings. This identification is typically achieved by comparison of  $d$ -spacings with standard reference patterns. Figure 2.3 shows a typical diffractogram of an unpromoted tetragonal sulfated zirconia sample derived from the industrial starting material.

### 2.2.1. Rietveld refinement

With the help of specialized techniques, XRD can be used to determine crystal structures using Rietveld refinement. The Rietveld method is a full-pattern refinement method using information of the whole diffraction pattern. For the refinement of the different crystalline phases observed in the diffraction pattern of a sample, information from a structure database is used. This makes it possible to simultaneously refine individual peaks. By taking into account certain instrument-specific parameters as well as sample and preparation effects, one is able to refine parameters like lattice constants and the positions of atoms of the specific structure. The assignment of every phase to a scaling factor allows for a quantitative phase analysis.

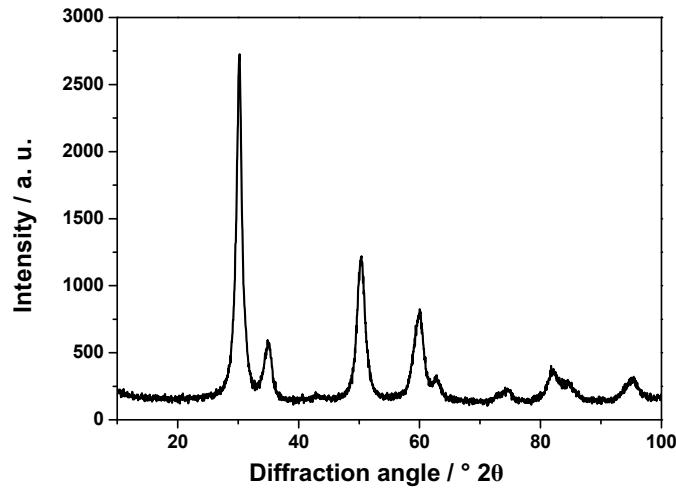


**Figure 2.3.:** Powder X-ray diffraction pattern of tetragonal unpromoted SZ derived from the industrial starting material with a 3% monoclinic phase content.

Even strongly superposed reflexes can be refined by a combination of Gaussian and Lorentzian functions. The overall process is an iterative least-square refinement by variation of the profile and crystal structure parameters. Approximation is performed until the best possible match between measured and calculated diffraction pattern is reached. Correct results can only be obtained if the least-square refinement reaches a global and not a local minimum.

### 2.2.2. Diffraction line profile analysis

Since the focus of this study is the investigation of possible defects in tetragonal SZ, information about domain size and strain within the polycrystalline powdered material is needed. It is possible to extract information about size and strain effects from the peak broadening of a particular diffraction pattern. The broadening of diffraction lines can originate from either non-ideal instrumentation, wavelength distributions of the X-ray photons or from structural imperfections of the crystalline material (as well as from a combination of at least two of these factors). Peak broadening due to lattice imperfections most often originates from size effects. Crystalline size broadening occurs when a crystal is broken up into smaller coherently diffracting domains by dislocation arrays, which are terminated by small angle boundaries, stacking faults, or other extended imperfections. Especially in nano-

structured materials, the impact of size effects needs to be considered. In Chapter 5, crystalline size is determined by using the integral breadth ( $\beta_i$ ), a concept developed by Stokes and Wilson in 1941, which presents a more generalized treatment of domain-size broadening. In this model, domain-size broadening is independent of the crystalline shape, with ( $L_{vol}$ ) being the volume weighed column height. Column height is a concept in which the crystal is divided into rectangular sections of columns, whose heights are then measured.

$$\beta_i = \alpha / L_{vol} \cos \vartheta \quad (2.3)$$

Strain is defined as  $\Delta d/d$ , the relative deviation of lattice distances from their ideal length, and results from displacements of atoms relative to their reference positions most typically caused by presence of dopants (substituting atoms), their inhomogeneous distribution, point and line defects, etc. The Bragg peak shape has to be taken from the diffractogram and fitted with the help of specific mathematical functions in order to calculate size and strain. Therefore, it has to be assumed that the model is physically correct for the material under investigation, which is otherwise not always the case.

### 2.2.3. New method of the determination of the apparent faulting probability in SZ

Most developed theoretical models relating peak broadening to certain types of defects are available for simple monoatomic structures like metallic face centered cubic (fcc) materials. Recently, the concentration of planar defects in Cu (twins and stacking faults), extracted from a combined analysis of XRD and TEM data, has been shown to play an important role in the activity of methanol synthesis catalysts [6]. Since no similar model exists for more complicated structures like tetragonal SZ, attempts have been made to adapt the existing models for cubic structures. Therefore, the Warren theory [93] for the determination of planar defects (twinning and stacking faults in cubic metals) was used and transformed in order to estimate an apparent faulting probability for SZ. Equation (2.4) is based on this theory, with ( $a$ ) being the lattice parameter  $a$ , ( $\alpha$ ) being the concentration of stacking faults and ( $\beta$ ) being the concentration of twins. It shows the true crystallite

size  $D_{\text{TEM}}$ , corrected for the presence of planar defects. This should be directly comparable to the particle size extracted from TEM images (with the help of the program *ImageJ* and particle encircling by hand), as a function of the apparent crystallite size ( $D_{111}$ ), typically extracted from XRD line broadening. The (111) peak is analyzed for fcc metals like copper.

$$D_{\text{TEM}} = \frac{a \cdot D_{111}}{a - (1.5\alpha + \beta)D_{111} \cdot \sqrt{\frac{3}{2}}} \quad (2.4)$$

Whereas the (101) peak can be used for tetragonal zirconia, because – coming from the cubic lattice – this peak does not split in the tetragonal phase, and the overall apparent faulting probability is assumed as  $(1.5\alpha + \beta)$ . The apparent size is estimated from XRD data, using a pseudo-Voigt single peak fitting of the tetragonal zirconia (101) peak, and the true size from TEM. The apparent crystallite size has been calculated using the model of Sánchez-Bajo et al. [94], who developed a model for zirconia.

By combining those sizes and using Equation (2.4), the apparent faulting probability can be extracted for cubic materials. For tetragonal zirconia, the apparent faulting probability  $(1.5\alpha + \beta)$  is transformed into:

$$1.5\alpha + \beta = \frac{a \cdot (D_{\text{TEM}} \cdot \sqrt{\frac{3}{2}} - 2 \cdot D_{101})}{\sqrt{\frac{3}{2}} \cdot D_{101} \cdot D_{\text{TEM}}}. \quad (2.5)$$

It should be noted that, in contrast to cubic copper, the observed defects in tetragonal zirconia are mainly dislocations and small angle-boundaries.

#### 2.2.4. Variance method

The variance method (or dispersion method) is an analytical model for the determination of crystallite size and crystal lattice micro strain distributions in nanocrystalline materials by XRD. It was published in 2009 for zirconia by Sánchez et al. [95]. The variance method can be used to establish analytically and, subsequently, generalize the connection between the variance coefficients of the physically broadened XRD peaks and the characteristic parameters of the particular distributions of crystallite sizes and crystal lattice microstrain. The proposed model is generic in nature and

can be used under the assumption of different mathematical functions for the two distributions, which results in a more detailed characterization of the nanocrystalline materials. The advantage is, that it can even be used in cases where a pseudo-Voigt fit is physically not correct.

### 2.3. Electron microscopy

In contrast to methods like XRD, which are based on the bulk structure of a sample, electron microscopy provides local information about the size and shape of nanoparticles and their agglomerates. Further information about structure and composition can be obtained by evaluating the interactions between the primary electron beam and the sample (Fig. 2.4). Several processes are triggered by electrons with energies between 100 and 400 keV hitting the investigated sample. When colliding with atoms, electrons can simply be scattered back or collide inelastically and transfer their energy to secondary electrons. Other electrons pass through the sample with or without suffering energy loss or they are scattered by particles. Photons in the range from UV to infrared mainly result from a recombination of electron-hole pairs in the sample.

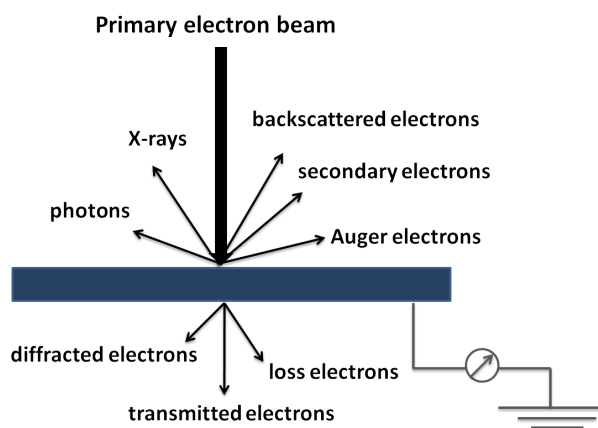


**Figure 2.4.:** Interaction between primary electrons and the sample in electron microscopy.

### 2.3.1. Transmission electron microscopy

In transmission electron microscopy (TEM) the attenuation of the electron beam depends on the density and the thickness of the investigated sample. By diffraction the diffracted beam intensity increases at the expense of the intensity of the primary electron beam. The fraction of elastically scattered electrons depends on structure, orientation, chemical composition, and defects of the crystalline sample. Accordingly, the diffracted electrons are used to obtain structural informations. The transmitted electron beam forms an image, representing a two-dimensional projection of a three-dimensional sample in direction of the electron beam. The magnified image resulting from these transmitted electrons is called bright-field image. In contrast to bright-field image, the dark-field image is produced by the diffracted electrons. The resolution is typically about 0.2 nm.

### 2.3.2. Scanning electron microscopy

Scanning electron microscopy (SEM) creates an image of the sample surface by scanning it with a high-energy beam of electrons in a raster scan pattern. The yield of either secondary electrons or backscattered electrons is determined as a function of the precisely focused primary electron beam which is scanning the sample surface. The image results from the different energies of the electrons. Its resolution is typically about 5 nm. Secondary electrons, whose energy is relatively low ( $<50$  eV), are ejected from the k-orbitals of the specimen atoms as a result of inelastic scattering interactions with beam electrons. They emerge from the sample surface and appear darker than the backscattered electrons. The latter emerge from deeper regions of the sample, and their brightness depends on the weight of the elements which the electrons are emitted from. Here, generally speaking, higher weight results in higher brightness.

## 2.4. Determination of sulfate content

### 2.4.1. Thermogravimetry analysis

Thermogravimetry analysis (TGA) uses the possibility of recording mass change as a function of temperature in a controlled atmosphere. Such an analysis relies on a high

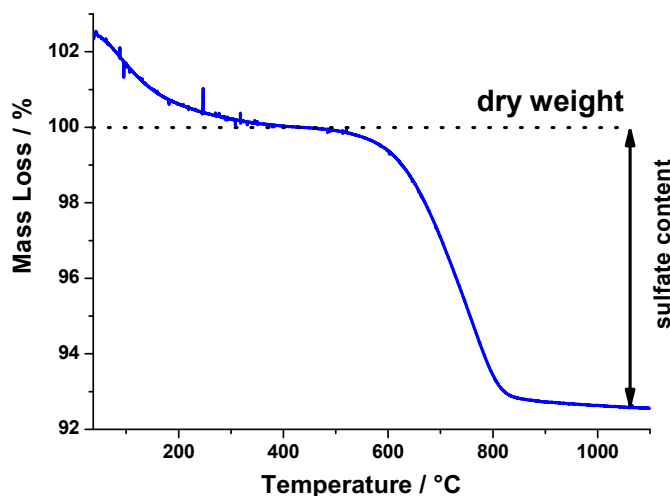


**Figure 2.5.:** Thermal analysis of SZ showing the weight loss which is attributed to sulfate. The weight at 437°C was determined as dry weight. Any weight loss beyond this temperature was assigned to the decomposition of sulfate and given as a measure for the sulfate concentration.

degree of precision in the measurement of three characteristics: weight, temperature, and temperature change. It is most often combined with a mass spectrometer and can provide information about degradation temperatures, absorbed moisture content of the respective materials, the level of inorganic and organic components in the materials, decomposition points of explosives, and solvent residues. In this study, it is predominantly used in order to determine the content of surface sulfates.

Simultaneous thermogravimetry/differential scanning calorimetry (TG/DSC) measures both heat flow and weight changes (TGA) in a material as a function of temperature or time. The complementary information obtained allows differentiation between endothermic and exothermic events which have no associated weight loss (e.g., melting and crystallization) and those which involve a weight loss (e.g., degradation).

In the literature, the TG weight losses above 500°C are associated with the decomposition of sulfate [44, 74, 96]. TG analysis of the investigated samples showed that after the first weight loss, the point of inflection is at 437°C. This weight at 437°C was determined as dry weight. Any weight loss beyond this point was assigned to the decomposition of sulfate and given as a measure for the sulfate concentration.



### **2.4.2. Ion chromatography**

Ion chromatography allows for the separation of ions and polar molecules based on their respective charge. It can be used for almost any kind of charged molecule and is often used in protein purification, water analysis, and quality control. Ion exchange chromatography retains the individually separated components (analyte anions or cations) of the column, based on coulomb (ionic) interactions. The stationary phase surface displays ionic functional groups (R-X) that interact with analyte ions of opposite charge. A buffered aqueous solution of known volume, known as the mobile phase, carries the sample from the loop, onto a column that contains some form of stationary phase material. This is typically a resin or gel matrix consisting of agarose or cellulose beads with covalently bonded charged functional groups. The target analytes are retained on the stationary phase but can be eluted by increasing the concentration of a similarly charged species that will displace the analyte ions from the stationary phase. The analytes of interest are typically analyzed with regard to their conductivity or UV/visible light absorbance.

## **2.5. Gas chromatography**

Gas chromatography (GC) is a common type of chromatography used in analytical chemistry for separating and analyzing compounds that can be vaporized without being decomposed. Typical uses of GC include testing the purity of a particular substance or splitting up a mixture of substances into their various components (the relative amounts of such components can also be determined). In GC, in contrast to ion chromatography, gas phase compounds are analyzed with the help of an inert carrier gas, for example He. The stationary phase is brought onto the inside of a small-diameter glass tube (a capillary column) or onto a solid matrix inside a larger metal tube (a packed column) covered with a microscopic layer of liquid or polymer. The gaseous compounds which are analyzed interact with the walls of the column, which are coated with different stationary phases. This results in each compound being eluted at a different time, known as the retention time of the compound. The comparison of retention times is what makes GC analytical useful. The column itself is located in an oven where temperature and vapor pressure of the gas can be controlled for. The concentration of a compound in the gas phase is essentially

a function of the vapor pressure of the gas. There are different types of detectors. In the present work, a thermal conductivity detector (TCD) was used, due to its advantage of fast detection (in this study 3 minutes for a single run ). A TCD detector consists of an electrically heated wire or thermistor. The temperature of the sensing element depends on the thermal conductivity of the gas flowing around it. Changes in thermal conductivity, as for example when organic molecules displace some of the carrier gas, cause a temperature rise in the element which is sensed as a change in resistance.

### 2.6. Infrared spectroscopy

Infrared (IR) spectroscopy takes advantage of the fact that molecules absorb specific frequencies according to their characteristic structure. These absorptions are resonant frequencies, i.e. the frequency of the absorbed radiation matches the frequency of the bond or group that vibrates. In a first approach, resonant frequencies can be related to the strength of the bond and the mass of the atoms at either end of it. Thus, the frequency of the vibrations can be associated with a particular bond type. IR spectroscopy is a tool for structural elucidation and compound identification.

The infrared region of the electromagnetic spectrum, following the region of visible light, is classified into near (with a wavelength of  $12500 - 4000 \text{ cm}^{-1}$ ), mid ( $4000 - 200 \text{ cm}^{-1}$ ), and far infrared radiation ( $200 - 10 \text{ cm}^{-1}$ ). IR radiation is absorbed when the radiation interacts with matter, thus exciting molecules to vibrate in combination with rotation, and stimulating their crystalline lattice and any existing functional groups on the material surface to vibrate. Absorption spectra are generated by plotting the intensity of the absorbed light versus its wavelength. Band positions are typically given in wavenumbers ( $\tilde{\nu}$ ), because these are directly proportional to the frequency, and therefore, with the energy of the radiation:

$$\tilde{\nu} = \frac{1}{\lambda} = \frac{\nu}{c} \quad (2.6)$$

The product of wavelength ( $\lambda$ ) and frequency ( $\nu$ ) is constant and equivalent to the propagation of the speed of light ( $c$ ). Light incident with the intensity ( $I_0$ ) is scattered by the sample and reflected at the phase boundaries, so that the intensity ( $I$ ) of the transmitted light is lower. Scattering in solids can be reduced by

embedding the sample in media with similar refractive indexes, e.g. pellets pressed with KBr. If luminescence and reflexion can be neglected adsorption capacity and transmittance taken together equal 100 %. The sample's adsorption properties can be calculated from the transmitted light by using the Lambert-Beer Law:

$$-\alpha = \tau = \frac{I}{I_0} = e^{-\kappa \cdot c \cdot l} \quad (2.7)$$

with  $\alpha$  being the adsorption factor,  $\tau$  the transmission factor,  $\kappa$  the molar extinction coefficient in units of  $\text{m}^2/\text{mol}$ ,  $c$  the molar concentration of absorbing species in units of  $\text{mol}/\text{m}^3$ , and  $l$  the sample thickness.

A vibration of a molecule is IR active, if its dipole moment changes with time as electromagnetic radiation can only interact with an oscillating dipole. Accordingly, symmetric vibrations, e.g. in linear molecules like  $\text{N}_2$ , are not observed in the IR spectrum. As CO vibrations have changing dipole moments, they absorb light in the IR spectrum. Therefore, CO can be used as probe molecule for the investigation of surface functional groups.

### 2.6.1. New method of the determination of the relative Lewis/Brønsted ratio

A new method was applied for the determination of the relative Lewis/Brønsted ratio. For the usual pyridine adsorption, the Lewis-Brønsted ratio (L/B ratio) can be determined from the spectra by using the method of Platon and Thomas [97]: The vibrational band of the pyridinium cation at  $1540\text{ cm}^{-1}$  is compared to that of the Lewis coordinated pyridine at  $1445\text{ cm}^{-1}$ . This means that the relative amounts of the peak areas are used as a measure for the L/B ratio. In order to avoid the drawbacks of pyridine adsorption (see Sect. 1.6), which could lead to questionable L/B ratios, CO was used as a probe molecule in this study. At room temperature, only strong Lewis acid sites can be probed, whereas at low temperatures it is possible to probe weaker interactions of the surface functional groups with CO as well. In order to probe Lewis and Brønsted sites under the same conditions, CO was adsorbed at liquid nitrogen temperature of  $-196^\circ\text{C}$ . In contrast to the usually investigated sulfate stretching vibration, the focus of this study is on the carbonyl stretching vibrations.

## 2. Methodology

All investigated samples were activated at 300 °C under vacuum conditions, as had been done for the catalytic reaction, before CO adsorption at  $-196^{\circ}\text{C}$ . In the present work, the influence of CO on the carbonyl stretching vibration at  $-196^{\circ}\text{C}$  was investigated between  $2100\text{--}2230\text{ cm}^{-1}$ . In this region one can observe Lewis and Brønsted acid sites as well as physisorbed CO.

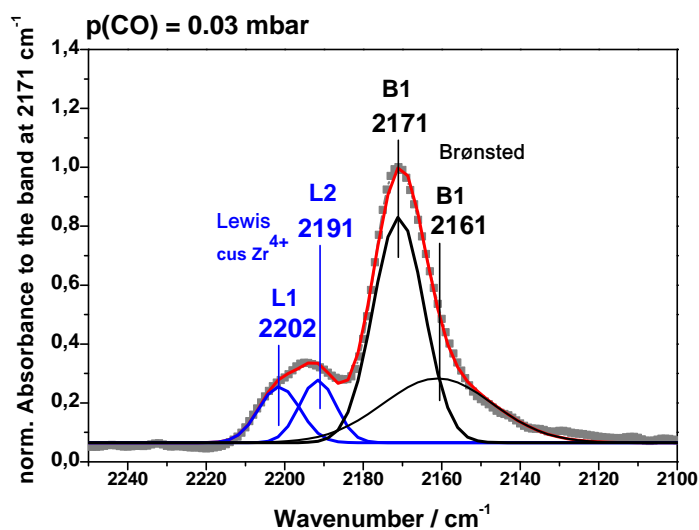


**Figure 2.6.:** Deconvolution of IR peaks: Two coordinatively unsaturated  $\text{Zr}^{4+}$  Lewis and two Brønsted acid sites were distinguished.

As reported by Spielbauer et al. [98], two coordinatively unsaturated  $\text{Zr}^{4+}$  Lewis sites and two Brønsted acid sites are detectable. In the present study, Lewis bands were found at  $2202$  and  $2192\text{ cm}^{-1}$  and Brønsted bands at  $2171$  and  $2161\text{ cm}^{-1}$ . For the determination of the relative L/B ratio, the total area was set as 100%. The relative L/B ratio was calculated from the relation of the sums of the areas of two Lewis ( $L_1$ ,  $L_2$ ) and Brønsted ( $B_1$ ,  $B_2$ ) sites, as given in equation 2.8.

$$\frac{(L_1 + L_2)}{(B_1 + B_2)} = r_{L/B} \quad (2.8)$$

Note that a relative L/B ratio of 1 would correspond to a surface where the amount of Lewis and Brønsted acid sites would be equal.

## 2.7. Determination of the long term deactivation rate constant

(Calculated by Lénárd-Istvan Csepei)

Deactivation kinetics should be seen independent of reaction kinetics [99]. The differential equation (eq. 2.9) is describing the deactivation kinetics where  $r$  is the reaction rate,  $r^0$  the initial reaction rate, and  $c_{deact}$  is the deactivation rate constant.

$$-\frac{dr}{dt} = c_{deact} \cdot r^n \quad (2.9)$$

For first order kinetics ( $n = 1$ ) after separation of variables Equation (2.9) is rewritten in eq. 2.10.

$$-\frac{dr}{dt} = c_{deact} \cdot r \quad (2.10)$$

The stepwise integration of eq. 2.10 results in eq. 2.11, with the initial rate  $t = 0 \rightarrow r^0$  and the current rate  $t = t \rightarrow r$ .

$$\begin{aligned} -\int_{r^0}^r \frac{dr}{r} &= -\ln r \Big|_{r^0} = -[\ln r - \ln r^0] = -\ln r + \ln r^0 \\ c_{deact} \int_0^t dt &= c_{deact} \cdot t \Big|_0^t = c_{deact}(t - 0) = c_{deact} \cdot t \end{aligned} \quad (2.11)$$

Equation (2.12) is representing the resulting integral rate law for first-order deactivation kinetics.

$$\ln r = \ln r^0 - c_{deact} \cdot t \quad (2.12)$$

Figure 2.7 shows that an apparent linear regime starts only after 26 h. This cannot be explained by initiation of the reaction with oxidative dehydrogenation, which is

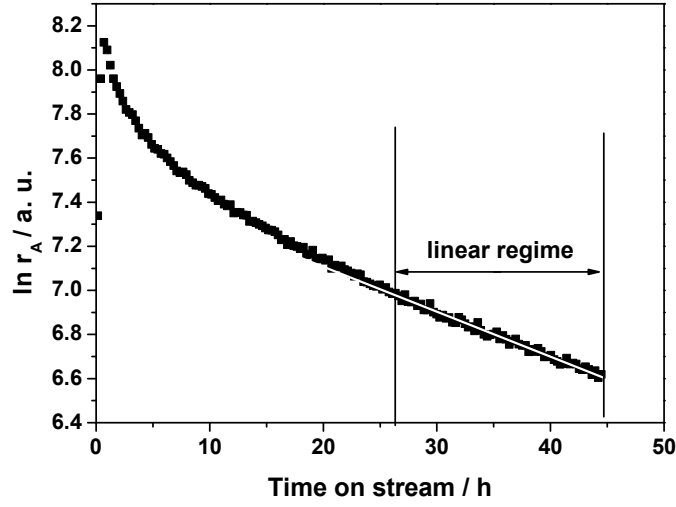


**Figure 2.7.:** Test for first-order deactivation kinetics. Since an apparent linear regime starts only after 26 h, which cannot be explained by initiation of the reaction with oxidative dehydrogenation (which is thought to be completed after 2 to 5 h) first-order deactivation kinetics is implausible.

thought to be completed after 2 to 5 h. Since oxidative dehydrogenation is thought to initiate of the catalytic reaction [100] first-order deactivation kinetics is implausible. For second-order deactivation kinetics after separation of variables eq. 2.9 can be rewritten as eq. 2.13.

$$-\frac{dr}{r^2} = c_{deact} \cdot dt \quad (2.13)$$

Analogue to first order kinetics a stepwise integration was done in eq. 2.14

$$\begin{aligned} -\int_{r^0}^r r^{-2} dr &= -r^{-1} \Big|_{r^0}^r = -\frac{1}{r} \Big|_{r^0}^r = \frac{1}{r} - \frac{1}{r^0} \\ c_{deact} \int_0^t dt &= c_{deact} \cdot t \Big|_0^t = c_{deact} \cdot t \end{aligned} \quad (2.14)$$

Based on these integrations a linear equation (eq. 2.15) is obtained as the rate law for second order kinetics.

$$\frac{1}{r} = \frac{1}{r^0} + c_{deact} \cdot t \quad (2.15)$$

Applying the latter equation on the investigated system (*n*-butane isomerization over SZ) the reciprocal reaction rate was plotted versus time on stream (Fig. 2.8). The figure shows a long linear segment. The segment starts after ca. 5 h, the time in which the reaction cycle is thought to be initiated with oxidative dehydrogenation. This confirms that the deactivation kinetics is of second-order. Accordingly, the deactivation rate constant ( $c_{deact}$ ) can be determined from the slope.

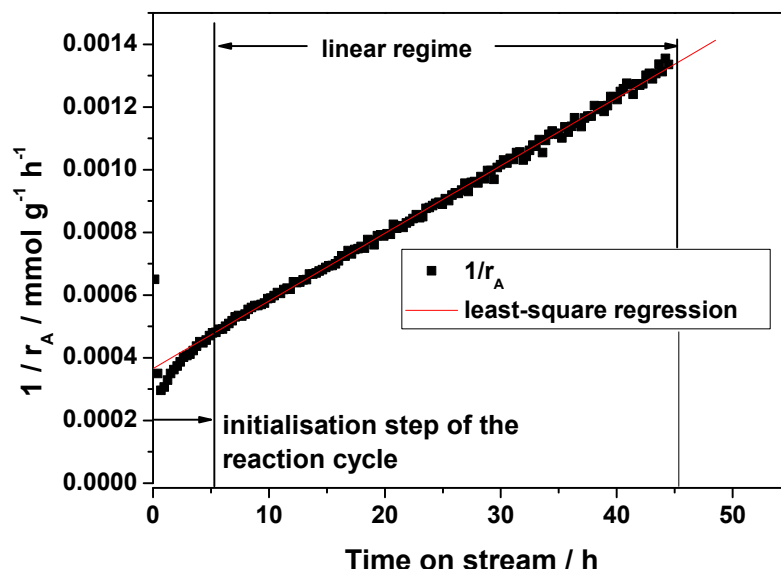


**Figure 2.8.:** Test for second-order deactivation kinetics. A long linear segment starts after ca. 5 h, the time which is attributed to the initiation of the reaction cycle. This confirms that the deactivation kinetics is of second-order, the deactivation rate constant ( $c_{deact}$ ) can be determined from the slope.

On that basis it is possible to calculate the reaction rates at any time. A slope of 1 in Figure 2.9 indicates that the calculated rate is in very good agreement with the measured rate. Moreover, with passing time the calculated and measured isobutane formation rates match better and better, which proves that a second-order kinetics is of . Extrapolating the calculated reaction rates (Fig. 2.10) demonstrates

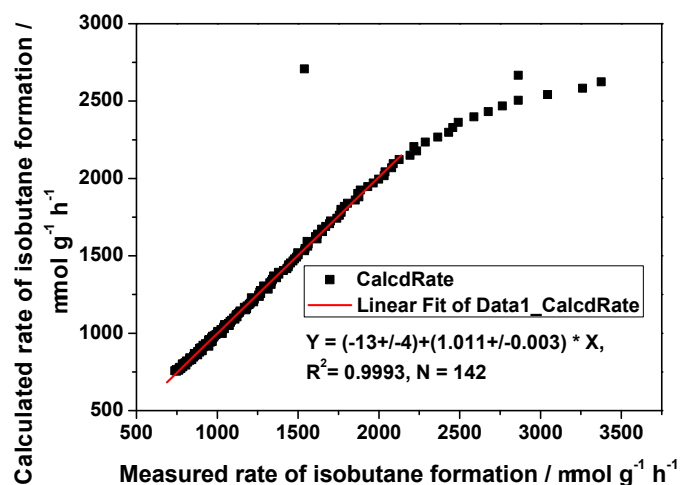


**Figure 2.9.:** Measured versus calculated rate of isobutane formation. A long linear regime, as well as a deviation from it in the first 5 h, which can be interpreted as the initiation step of the reaction, confirm second-order deactivation kinetic.

that there is a deactivation even after 250 h time on stream. Probably, without additional doping with platinum and the use of hydrogen gas feed stream during the isomerization, no steady state conditions can be reached with SZ catalysts (see Sec. 1.7).

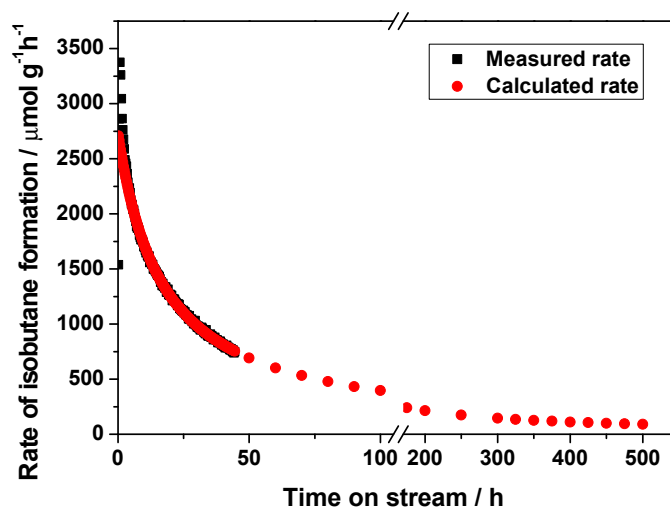


**Figure 2.10.:** Measured and calculated rate of isobutane formation versus time. Even after 250 h time on stream no steady state is reached. Most likely, without additional doping with platinum and the use of hydrogen gas feed stream during the isomerization, no steady state conditions can be reached with SZ catalysts.



## 3. Experimental

### 3.1. Catalyst preparation

#### 3.1.1. Unpromoted sulfated zirconia

In order to obtain an active sulfated zirconium catalyst, a commercially available precursor, namely sulfated hydrous zirconia, was used (*MEL Chemicals XZ0 1249*). This precursor had previously been identified as suitable [39]. Sulfate had already been introduced in the form of  $(\text{NH}_4)_2\text{SO}_4$  with a sulfate content corresponding to 6.5 wt% (measured by TG-MS). The BET-surface area of the material is  $425.69 \text{ m}^2/\text{g}$ . The industrial starting material lost in total 56 % weight during drying overnight at  $110^\circ\text{C}$  and the calcination process (1.5.1), 38 % during drying and 18 % during the calcination. Overnight drying was always carefully performed before weighing and calcination of the starting material, the general preparation steps for unpromoted SZ catalysts. The industrial precursor was used as a starting material for unpromoted SZ (Chap. 4, 5, 6 and 7).

Fig. 3.1a illustrates the steps of preparation of co-precipitated TmSZ (and precipitated SZ): Starting from a solution co-precipitation (precipitation) was followed by washing, filtering and drying. Subsequently the samples were sulfated, dried and calcined. Promoted zirconium hydroxide powders were prepared by co-precipitation of a solution of  $\text{ZrO}(\text{NO}_3)_2$  (*Fluka*,  $\geq 95\%$ ) and  $\text{Tm}(\text{NO}_3)_3 \cdot \text{H}_2\text{O}$  ( $x \approx 5$ ) (*Alfa Aesar*, 99.9% ) with  $\text{NH}_3$  solution. Since scalable and reproducible preparation under controlled conditions is a prerequisite for knowledge-based catalyst design, controlled co-precipitation was performed in an automated laboratory reactor system (*Mettler-Toledo Labmax*) (Fig. 3.1b) where the pH and the temperature were monitored by in situ probes.

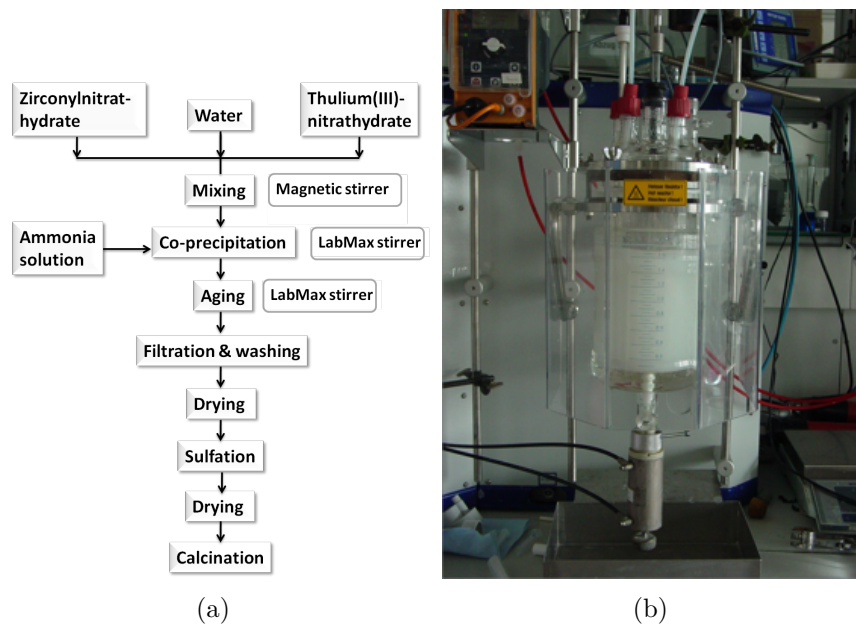


**Figure 3.1.:** (a) Preparation of SZ and TmSZ (b) Co-precipitation and aging in an automated laboratory reactor system (*Mettler-Toledo Labmax*)

#### 3.1.2. Promoted sulfated zirconia

$\text{ZrO}(\text{NO}_3)_2$  and  $\text{Tm}(\text{NO}_3)_3$  (approx. 67 g material in total) were dissolved in 750 mL deionized water and precipitated by adding an aqueous solution of  $\text{NH}_3$  at constant pH of 9 at  $45^\circ\text{C}$  under perpetual stirring with a rotation speed of 300 rpm (Fig. 3.2). Co-precipitation was carried out for 45 min, followed by an aging step at the same temperature for 1 h (stirrer rotation speed of 450 rpm). After aging the precipitate was filtered, washed, and dried. The precipitate was washed 3 times with deionized water (*Millipore-Q+*), once with alcohol, and finally with acetone (*technical grade*). The resulting wet cake was covered and dried for 3 days in air (for slow and homogeneous drying conditions, followed by drying overnight at  $110^\circ\text{C}$ ). Subsequently, the dry cake was pulverized and homogenized in an automatic mortar mill (*Retsch RM 200*) at the lowest pressure adjustment for 5 min.

The following sulfation was carried out by incipient wetness impregnation, using  $\text{NH}_4\text{SO}_4$  solutions yielding nominal sulfate loadings between 6 – 14 wt% in the amorphous catalyst precursor. Since the incipient wetness technique requires, that only the pores be filled with the solution, the amount of water in the solution was

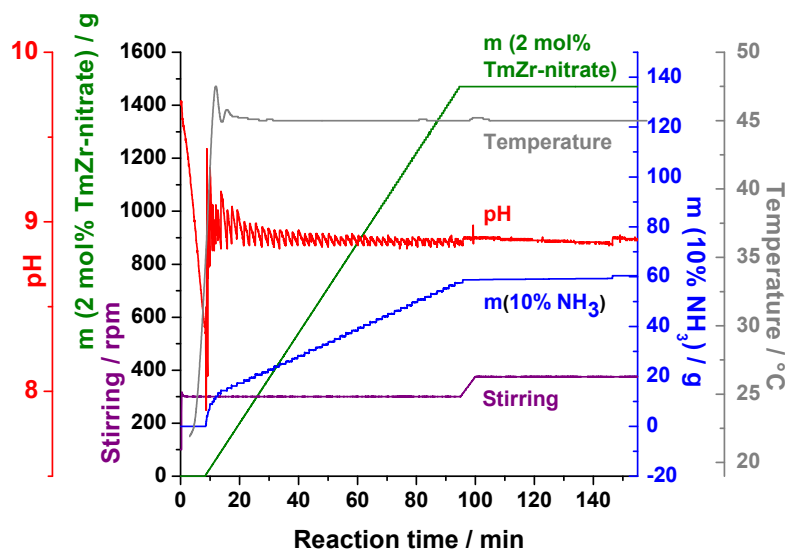


**Figure 3.2.:** Conditions of co-precipitation and aging in an automated laboratory reactor system (*Mettler-Toledo Labmax*)

varied. In order to do so the appropriate amount of solution was dropped into the dried promoted zirconium hydroxide powder in an automated mortar mill for 10 min under continuous homogenization. Throughout the whole procedure, the lowest possible pressure was used in order to avoid an agglomeration of the particles (seen by HRTEM) and to have a reproducible homogenization procedure. After 10 min, the resulting catalyst precursor was homogenized for another 5 min, followed by overnight drying at 110 °C, and re-homogenization for 5 min in its dry state.

## 3.2. Catalyst calcination

### 3.2.1. Calcination in a vertical tubular furnace

The catalyst precursors of the quenching series (Chap. 5) were calcined in a vertical tubular furnace. The sealings of the calcination setup were fixed with glass vacuum flanges without the use of grease. This is because in earlier experiments the use of grease led to leaks in the setup, which in turn resulted in different optimum calcination parameters.

Prior to calcination, the dried zirconium hydroxide powder was compressed, layer by layer, in a cylindrical sample holder (volume: 25 mL) with the help of a test

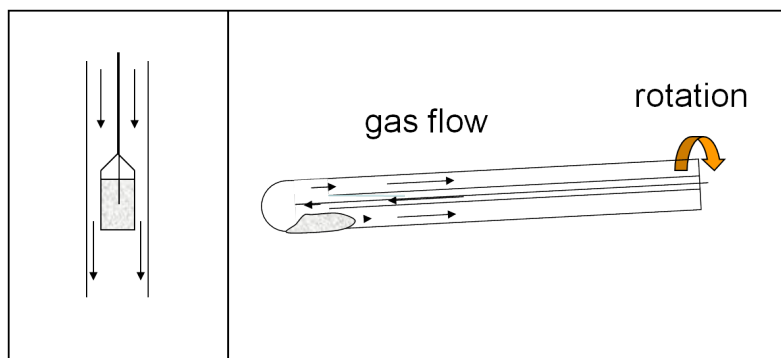


**Figure 3.3.:** Comparison of the two calcination set ups, (left) vertical tubular furnace, which was used for quenching experiments, (right) horizontal rocking furnace.

tube used as stamp. The sample holder, containing 20 g of catalyst precursor, was placed in a quartz glass tube with a volume of 2.5 L in the middle of the isotherm zone (length 10 cm) of a vertical tubular furnace (Fig. 3.3) with a platinum wire. The temperature of the furnace was controlled by a *Eurotherm 2604* temperature controller; the temperatures of the furnace and the middle of the sample bed were monitored with Ni-Cr-Ni thermocouples (*Thermocoaax*) and an *NI USB-9211* thermocouple input module connected with a computer. That way, it was possible to monitor the sudden temperature rise in the catalyst bed during the glow phenomena (Fig. 3.4). Calcination was performed in air flowing with a speed of 200 mL/min (adjusted by a rotameter) at 550 °C. The temperature was kept constant for 3 h, during which a temperature ramp for heating and cooling of 3 °C/min was applied. Deviations in the temperature during the ramps and the temperature plateau were  $\pm 1$  °C.

#### 3.2.2. Calcination in a horizontal rocking furnace

For calcination in a horizontal rocking furnace we used an oven (Fig. 3.3) with an agitated sample bed (Chap. 6, Chap. 7, Chap. 8). The agitated bed guaranteed for a homogeneous sample and suppressed the glow phenomenon completely. The calcination tube had a volume of 2 L. The gas flow was controlled for by a *Bronkhorst* mass flow controller; the temperature was controlled for by an *Eurotherm* temperature controller; and monitored with Ni-Cr-Ni thermocouples (*Thermocoaax*)

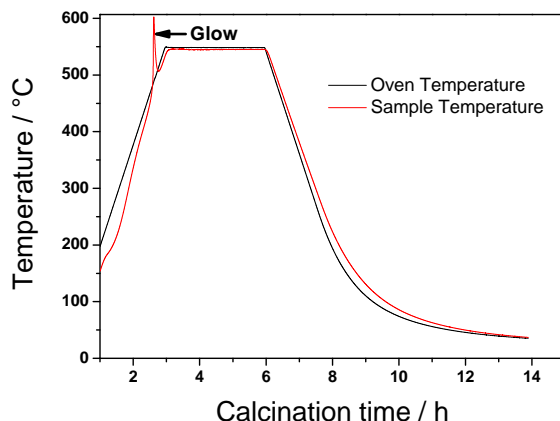


**Figure 3.4.:** Calcination program for quenching experiments in a vertical tubular furnace

and an *NI USB-9211* thermocouple input module connected with a computer. The thermocouple was fixed in position and sealed by Kleinflansch (KF) standard vacuum connection. Therefore a new quartz glass calcination tube equipped with KF standard vacuum connections was developed in order to guarantee air tightness of the calcination tube. In this way, the use of grease could be avoided. The catalyst powder was put into the end of a completely air tight tube. It was placed in the isotherm zone (length of 12 cm) of the furnace. Before starting a calcination, the setup was leak checked every time. A thermocouple connected with a computer monitored the temperature in the middle of the calcination tube at the position of the sample powder.

During the optimization procedure of the calcination (Chap. 6) calcination was performed between 550 and 650 °C in steps of 25 °C; the holding time varied between 1 – 21 h. The gas flow rate changed between 100 and 900 mL/min, and the oxygen partial pressure varied between 0 – 100 %. For the optimization only one parameter was changed at once, while the others were kept constant.

The following optimized calcination conditions were taken as starting conditions for the samples treated with different gas atmospheres during calcination (Chap. 7): 550 °C, 3 h, 500 mL/min 100 % Ar. During the whole time of the calcination procedure, the carrier gas was led through 50 mL of different liquids (water, sulfuric acid or oleum) at room temperature before it entered the quartz glass calcination tube, which in turn was filled with 17 g of amorphous precatalyst powder. One

part of the calcined optimized sample and the oleum sample underwent a post-treatment with gaseous  $\text{SO}_3$  at  $200^\circ\text{C}$  in a special apparatus for a few seconds (TU Munich) [101]. Before gaseous  $\text{SO}_3$  was added, SZ was preheated in a quartz tube under  $\text{N}_2$  with a flow rate of  $50\text{ mL/min}$  at  $400^\circ\text{C}$  for 2 h. In deviation from what has been described in the literature [101], the gas was led over a solid piece of  $\text{SO}_3$  in order to produce a gaseous  $\text{SO}_3$  atmosphere.

For the calcination of thulium promoted zirconium hydroxide (Chap. 8), 20 g of the material was used. The calcination was performed at  $625^\circ\text{C}$  in flowing  $500\text{ mL/min}$  100 % Ar, which was loaded with oleum. The temperature was held for 3 h, applying a temperature ramp for heating and cooling of  $3^\circ\text{C/min}$ .

### 3.3. Catalyst storage conditions

Each of the samples stored in laboratory cupboards suffered from aging. A double container technique (Fig. 3.5) was found to avoid air contact in an effective and long-lasting way. This technique has the advantage that the amount of air which gets into contact with the sample can be kept as small as possible after catalyst sampling. "Fresh" catalyst material was still available for analysis after several times of sampling. For this storage technique, the catalyst powder was filled in microfuge tubes, which were then stored in bigger catalyst containers. For small quantities of samples, storage in a vacuum desiccator gave the lowest aging effect. Larger quantities of samples were stored in a secador desiccator cabinet.

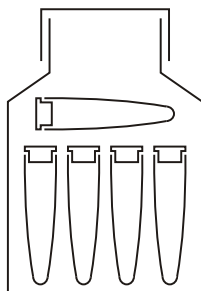


**Figure 3.5.:** The double container technique reduces the contact of the catalyst powder to air. With this technique catalyst aging can be reduced.

## 3.4. Catalyst characterization

### 3.4.1. Determination of sulfate content

#### Thermal analysis

Thermal analysis was carried out with a *Netzsch Jupiter Sta 449C* thermo balance under a controlled total flow of 100 mL/min (30 mL/min protective gas and 70 mL/min pure gas). Approximately 20 mg of sample were treated with 100 % Ar up to 1100 °C at a heating rate of 2 °C/min, maintained at this temperature for 30 min and ramped back to 200 °C at a cooling rate of 2 °C/min. The gases involved in the thermal analysis were monitored with a quadrupole mass spectrometer *QMS200 Omnistar*, *Balzers* coupled to the thermal balance via a quartz capillary.

#### Ion chromatography

Sulfate content was measured by a *Metrohm 690* ion chromatograph equipped with an Ion chromatography (IC) anion column (TU Munich) [102]. For this purpose, 0.02 g of SZ powder was suspended in 20 mL of 0.01 M NaOH for 20 min. The solution was filtered through a 0.45 µL filter, and the sulfur content in the liquid was determined by IC.

### 3.4.2. BET

The BET surface area of SZ was determined by measuring the nitrogen adsorption-desorption isotherms with a Quantachrome Autosorb automatic BET-sorptometer at −196 °C with nitrogen as the analysis gas. Prior to the analysis, the samples were outgased for 2 h at 200 °C.

### 3.4.3. XRD

X-ray diffraction (XRD) measurements were performed in Bragg-Brentano reflexion geometry with a Bruker AXS D8 Advance diffractometer equipped with a secondary graphite monochromator (Cu K 1+2 radiation) and a scintillation detector. The sample powder was filled into the recess of a sample cup, yielding a flat surface of

the sample bed. The angle range described was between  $10^\circ$  and  $100^\circ$  with a step size of  $0.04^\circ$ .

#### Pattern fitting

XRD data were fitted with the software package *Topas* version 3.0 (Bruker AXS) by using the Rietveld method. The calculations of the theoretical peak intensities for monoclinic and tetragonal zirconia were based on ICSD entries 89426 and 97004, respectively. The monoclinic/tetragonal ratio follows directly from the Rietveld fits, while the fraction of amorphous precursor phase (if present in larger quantities) was estimated from the area of a corresponding model pattern in comparison to the area of the crystalline fraction. The model pattern of “amorphous” SZ was derived from the XRD pattern of a dried SZ precursor. Very broad peaks of this pattern were fitted using seven Gaussian peaks. Subsequently, the resulting set of peaks was used as a model with fixed relative intensities and peak positions but variable peak widths and total intensity in the case of mixed precursor/crystalline samples.

#### 3.4.4. Transmission FTIR spectroscopy/CO adsorption

IR experiments were carried out on a *Perkin Elmer PE 100* equipped with a liquid nitrogen cooled DTGS (deuterated triglycine sulfate) detector at a spectral resolution of  $4\text{ cm}^{-1}$  and an accumulation of 32 scans. At first, the samples were pressed into infrared transparent self-supporting pellets (typically 20 to  $30\text{ mg/cm}^2$ ) at 123 MPa. Afterwards, they were placed in a homemade stainless steel low temperature infrared cell with  $\text{CaF}_2$  windows. The cell was connected to a vacuum system; details of the latter can be found elsewhere [103]. Catalyst activation was performed in situ in the heating zone of the IR cell under vacuum with a final pressure of  $10^{-6}\text{ mbar}$  at  $300^\circ\text{C}$  for 30 min (subsequent experiments with one sample). The spectra were recorded at  $-196^\circ\text{C}$  while CO pressure was increased iteratively in the range of  $0.001 - 6.0\text{ mbar}$  (complete coverage of the surface) in steps of  $0.005\text{ mbar}$ , followed by larger steps up to  $2\text{ mbar}$ . All spectra shown in the present work represent the difference between spectra of the sample recorded in presence and in absence of CO. Figure 3.6 shows a linear correlation between the intensity of the bands due to CO adsorption on Brønsted sites and the pellet density in agreement with the Lambert-Beer equation.



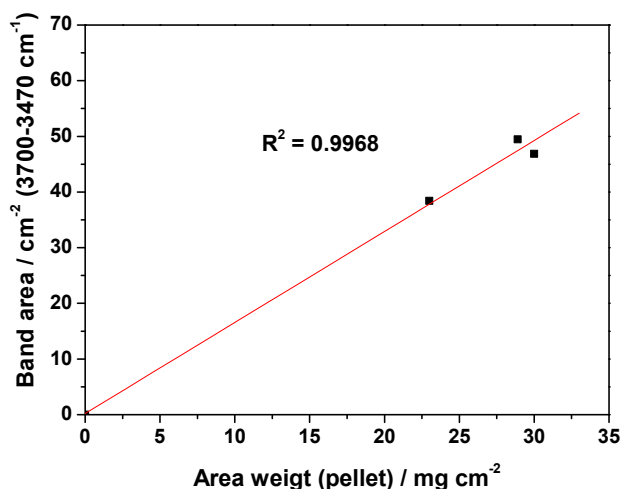


**Figure 3.6.:** Linear correlation between the intensity of the bands due to CO adsorption on Brønsted sites and the pellet density

### 3.4.5. Electron microscopy

In pre-experiments we found out that dispersion of the sample with liquids results in structural and morphological changes due to sulfur loss on the sample surface. Therefore, the sample grid was dipped into the sample and any surplus material was removed afterwards. For TEM particle investigations, the samples were dispersed by blowing the sample powder softly on a sample grid in order to obtain a well-dispersed powder without the use of liquids. Afterwards, the grid with the sample on top was fixed on a vacuum transfer sample holder.

#### SEM

A *Hitachi 4800* SEM was used to investigate the morphology and shape of the agglomerates of the SZ particles. The excitation voltage was 1.5 kV.

#### TEM

A TEM equipped with a LaB6 emitter (*Philips CM200*) operated at 200 kV was used to perform overview investigations of particle sizes. For that purpose more than 1000 particles were counted for the unpromoted samples and more than 2000 for the promoted samples.

High resolution transmission electron microscopy (HRTEM) investigation of the unpromoted SZ catalysts was performed on a *Philips CM 200 FEG* microscope equipped with a *Gatan* imaging filter operating at 200 kV ( $C_s = 1.35\text{mm}$ ). The information limit was better than 0.18 nm. The experimental micrographs were taken with a CCD camera.

Thulium-promoted samples were investigated for defect analysis with *FEI Titan 80-300* at 80 – 300 kV with a CS corrector for the correction of spherical aberrations. The spacial resolution was 0.08 nm.

## 3.5. Isomerization of *n*-butane

The catalytic properties of SZ as a powder were studied for the *n*-butane isomerization in a U-shaped fixed bed flow reactor. In the course of this study we constructed a three channel fluidized sand bed reactor system in order to be able to investigate high quantities of catalyst powders reproducibly within a relatively short time interval. That again helped us to compare catalyst samples of the same experimental series with each other. The set-up made it possible to investigate three catalysts at the same time, allowing a threefold enhancement of the catalytic test reaction. This helped enormously in speeding up the testing procedure, since a single catalyst run took 24 h for unpromoted catalysts and 36 h for thulium promoted catalysts.

### Reactors

Figure 3.7 shows a U-shaped tubular reactor tube. These reactors were made of quartz glass with an inner diameter of 4 mm with narrow tolerance of this value. They were fixed in holes of the lid of the sand bed with *Teflon* seals. The choice of quartz glass made it possible to carry out controlled catalyst loading and ensured temperature resistance of the reactor tubes during activation and reaction. The tubing was made of a single piece of quartz glass without cutting to improve the mechanical strength. The pure catalyst powder was put between glass wool plugs so as to create plug flow conditions. Small glass pinches at a position above the U-curvature in the reactor tubes fixed the catalyst bed position for all three reactors and ensured uniform gas flow conditions. The catalyst bed length-to-width ratio was 3/1 in order to avoid channeling problems in the catalyst bed. The aspect ratio

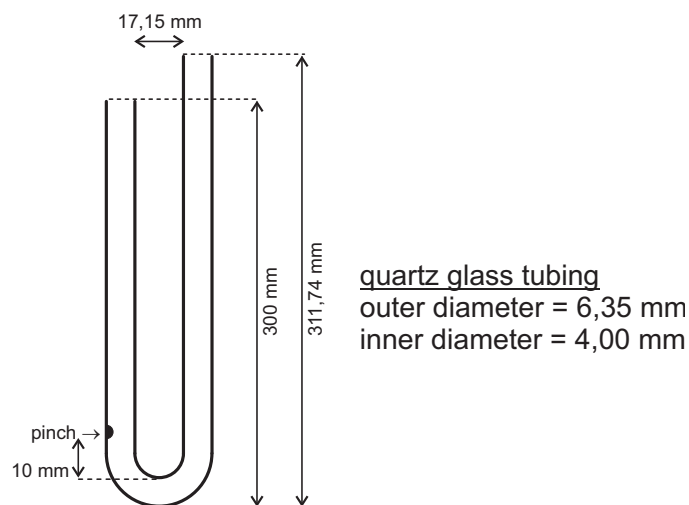


**Figure 3.7.:** Tubular reactor, which was used in the three channel fluidized sand bed reactor system.

corresponded to a catalyst loading of 250 mg for unpromoted SZ catalysts made of the industrial starting material, and 200 mg for co-precipitated promoted catalysts.

### Experimental set-up

The flow chart of the experimental set-up is shown in Figure 3.8, which consists of the main components: gas dosing system, three channel fixed bed reactor, and product gas analysis. All tubings were made of stainless steel. For activation, reaction or purging different gases could be used for the activation as well as for the reaction lines of the setup. The reactors were placed in a fluidized bed of sand which served as a source of heat in order to provide isothermal operating conditions. The sand bed vessel with the reactor heating was taken from an already existing set-up and has been described elsewhere [104]. The sand was fluidized by flowing air of 20 mL/min through a frit. At the air outlet position of the sand bed, a sieve (*Swagelok*) prevented the sand from escaping. In order to maintain the same pressure conditions in every reactor tube, resistors created a pressure drop of 3 bar in front of the point at which the gas entered the reactor tubes; the pressure drop over the catalyst bed was therefore negligibly small with only 0.05 bar. All three catalysts were held at the same temperature during their activation as well as during the catalytic reaction. The temperature on top of the catalyst bed

### 3. Experimental

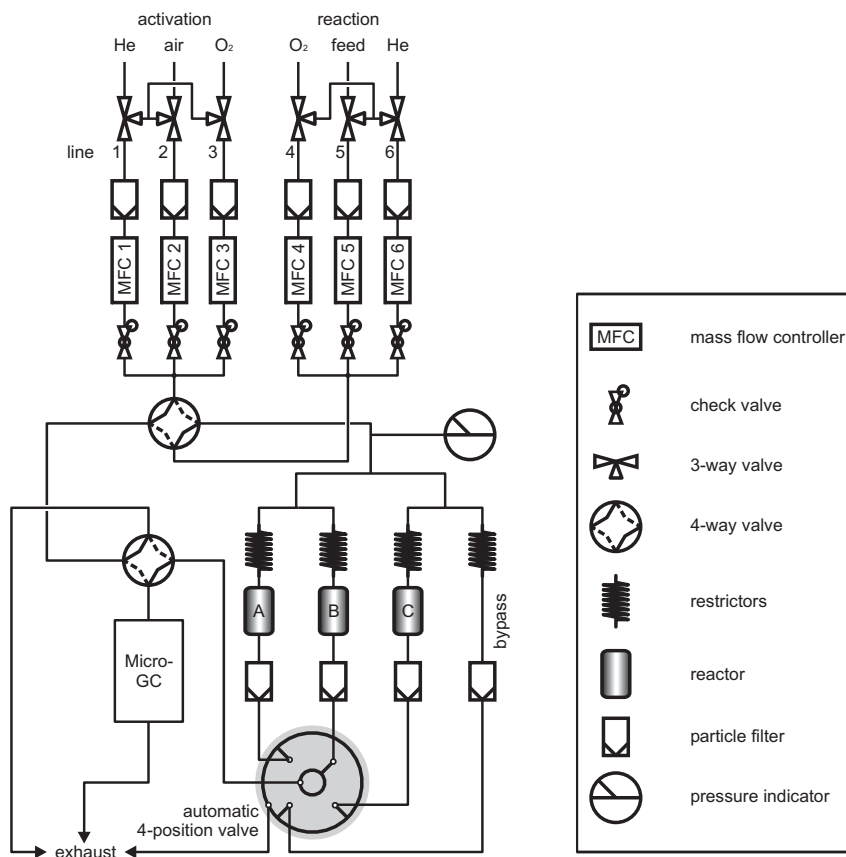


**Figure 3.8.:** Flow-chart of the experimental set-up, which was used for catalyst testing in *n*-butane isomerization.

was measured in each reactor tube and monitored on a computer (Fig. 3.9). One of the thermocouples (*Thermocoax*, K-type) in the reactor tubes controlled the reactor temperature via a linear temperature programmer (*Newtronic Micro 96*). An additional thermocouple monitored the temperature in the middle of the sand bed. Temperature deviations in the sand bed, and therefore, in the catalyst bed were  $\pm 1^\circ\text{C}$  within the studied temperature range.

#### Reaction conditions

In this study, it was found that an activation temperature of  $300^\circ\text{C}$  yielded optimum *n*-butane isomerization rates. For activation, the catalyst powder was heated in flowing He with  $15^\circ\text{C}/\text{min}$  to  $300^\circ\text{C}$ . The catalyst powder was activated for 30 min

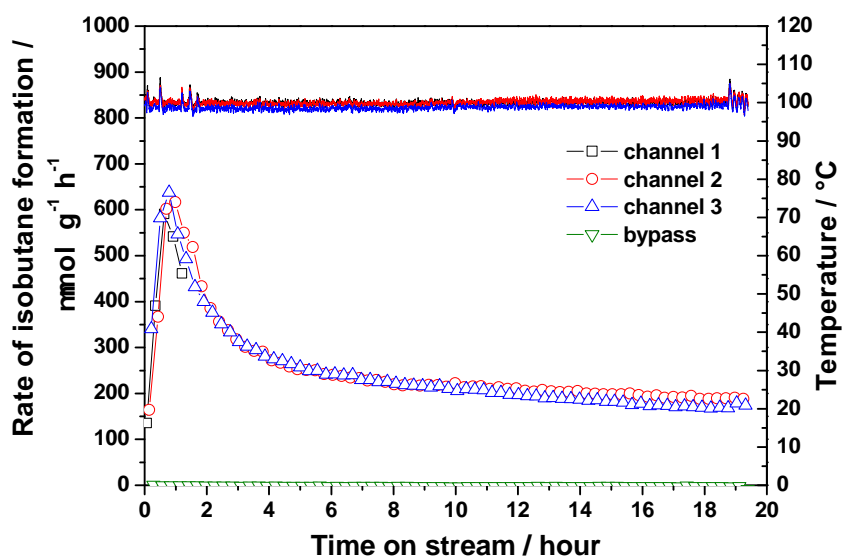


**Figure 3.9.:** Reproducibility test of the catalytic reaction and the corresponding temperatures of the catalyst beds. The test confirms that a given catalyst shows the same rate of isobutane formation in the individual reactor tubes and that all three catalysts were held at the same temperature during their activation, as well as during the catalytic reaction.

at this temperature in in helium flowing at 25 mL/min *Westfalen*. The gas was purified with *Oxysorb* and *Hydrosorb* cartridges (*Air Liquide*). The temperature was chosen as low as possible to avoid defect migration from the bulk to the catalyst surface. After activation, the catalyst was cooled down to the reaction temperature of 100°C in about 30 min. Cooling was also performed under He flow. The reaction feed of 5% *n*-butane in He mixture (*Westfalen*) was run with 25 mL/min at atmospheric pressure. The rate of isobutane formation at 100°C was taken as a measure of catalytic activity. Every channel (three with catalyst powder and one bypass) was measured every 20 min. Besides *n*-butane, pentane and propane were the detectable as minor phases. It was subtracted from the isobutane concentration in the effluent stream. Since oxygen strongly influences the reaction the O<sub>2</sub> content of the reactor system was carefully maintained below 50 ppm during both activation and reaction.

### Product analysis

A four-position valve (*VICI*, RS232 interface,  $\frac{1}{8}$ " fittings) rotatively sampled one of the three catalyst channels or the bypass, so that every channel was sampled every

### 3. Experimental

---

15 min. The gas of the lines which were not being sampled at the moment went into the exhaust. The feed and product components leaving the reactor were analyzed by an on-line micro gas chromatograph (*Varian CP 4900*) with a *CP-sil 5CB* (dimethylpolysiloxane) column. The hydrocarbon compounds were analyzed with a thermal conductivity detector. The gas phase was analyzed using the *Varian Star Chromatography Workstation* in combination with *Valve Control*. Figure 3.9 illustrates the reproducibility of one catalyst measured in the three channels at the same time and the corresponding temperature of the catalyst bed. Temperature, as well as catalytic performance, are reproducible for all three channels, whereas the bypass did not show catalytic activity as expected.

## 4. Catalyst aging

Aging is one of the most demanding challenges that one encounters when working with SZ catalysts, because SZ is an extremely sensitive material. Klose [104] optimized the storage conditions for unpromoted as well as for promoted SZ catalysts, by investigating different gas atmospheres and humidities. The catalysts were stored under different conditions for several months. The laboratory cupboard was found to be the best location to store the plastic containers in which the catalyst materials are typically kept. Even after this optimization procedure, however, it is striking that activity differences of two unpromoted samples prepared in the same manner amounts to 25 %, which is after one month reduced to 7 % due to the aging phenomenon. These differences are too large to allow for precise comparisons between two samples or a whole series of samples. By consequence, the preparation of the present study required the aging phenomenon to be investigated in detail first before calcining series of samples. Further optimization of the storage conditions appeared as the key to the aging phenomenon.

### 4.1. Results and Discussion

Since SZ is a sensitive hygroscopic material, considerable hydration occurs as a consequence of storage at ambient temperature [79]. During the activation phase prior to the actual reaction, only part of the water on the sample surface can be removed. This indicates that the storage conditions influence the performance of SZ catalysts drastically. Contrary descriptions in literature notwithstanding [104], samples stored in the laboratory cupboard suffer from aging (Fig. 4.1). The main cause of negative aging effect was the contact between the material powder and atmospheric humidity in the air.

Since the charging level of a given sample defines the volume of air left in a sample container, the charging level of the sample was found to be crucial. In frequently

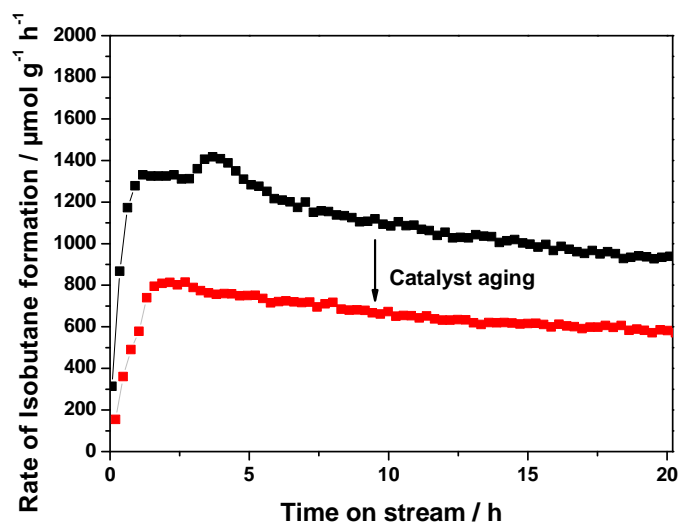


**Figure 4.1.:** Aging of an SZ sample stored on the laboratory cupboard for seven month. The catalytic activity of the sample is drastically decreased after seven month storage on the laboratory cupboard.

opened sample containers, where the sample surface was often exposed to air, the aging process accelerated. Furthermore, the sealing and the atmosphere in which the containers are stored are very important. A completely filled glass container was found to be a simple and feasible method. For frequently used samples or amounts of catalyst powder that were not immediately applied, the double container technique, as described in Chapter 3, was found to yield the best storage results. The containers were stored in a secador desiccator cabinet or an evacuated desiccator.

Aged samples can be identified by braying it by hand, which gives a soft and wet feeling, in contrast to the roughness and dryness of fresh catalysts. Catalyst aging starts at the moment of first exposure of the sample to air after opening a well stored sample. At optimum storage conditions, on the other hand, the influence of the time span between preparation and the first opening of the container is negligible. Despite optimum storage of the sample containers, catalyst aging can be detected with TG, if no double container technique is used. TG profiles of two samples of the gas flow series (Chap. 6) are presented in Figure 4.2. Both samples were measured after 3 and 12 months. The figure illustrates that the size of the effect is similar for samples prepared at the same time. The aged samples show a 0.9 % higher weight loss in the low temperature region (measured up to the point of inflection at 437 °C) and a 0.3 % lower weight loss at higher temperatures. Mass



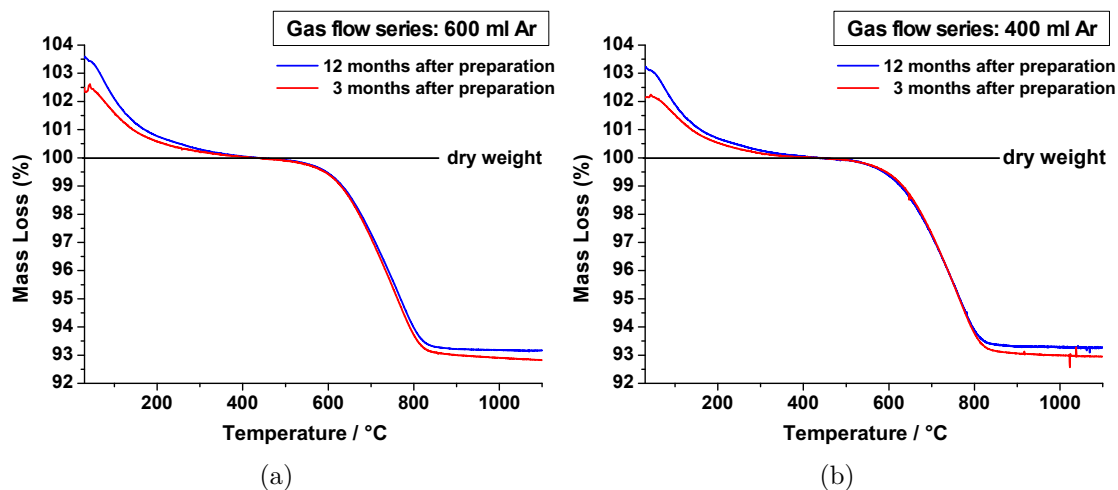


**Figure 4.2.:** TG curves of SZ of the gas flow series measured 3 and 12 months after preparation: (a) 600 ml/min Ar (b) 400 ml/min Ar. Both samples show aging characteristics – higher water (low temperature region) and lower sulfate contents (high temperature region) – due to several contacts to air.

spectrometry (MS) measurements proved the first weight loss to be associated with water evaporation and the second with loss of sulfate, which is in agreement with the literature [44, 74, 96]. When aging is inevitable, it leads to adsorption of water on the sample surface. Interestingly, when an aged sample is heated, the second weight loss above the point of inflection, which is associated with the decomposition of sulfate, is smaller for both investigated samples. The smaller weight loss in TG investigations in the region of sulfate decompositions leads to the assumption that small amounts of labile sulfate groups are adhere to the adsorbed water on the sample surface and, in the low temperature region, desorbed from the surface along with the water. This process could occur during catalyst activation prior to reaction and fits with the results of low temperature CO adsorption studies, discussed in Section 6.1.6. In this section, we will show that catalyst aging results in higher Lewis to Brønsted ratios on the catalyst surface.

As will be shown in Section 6.1.6 the correction of the aging effect with a computed value gives convincing results for probable initial relative L/B values of the fresh samples. Aging goes hand in hand with increasing humidity of the sample surface as could be shown with TG-MS measurements. Probably humidity is attracted by complexes of labile sulfate groups, associated with Brønsted acid sites. The labile

#### 4. Catalyst aging

sulfate groups are desorbed together with the adsorbed water from the surface in the low temperature region during the activation procedure at 300 °C in vacuum. This matches with the result of TG investigations (Fig. 4.2), that aged samples show lower weight loss in the high temperature region, associated with sulfate decomposition. Thereby the relative L/B ratio shifts for the benefit of Lewis acid sites. Already in 1998 Li and Gonzalez [79] investigated different catalyst regeneration conditions. Regeneration in N<sub>2</sub> led to a small loss in the sulfur content resulting in a complete loss of the catalytic activity combined with a very high L/B ratio.

Figure 4.3 illustrates a sample after the optimization of storage conditions as described above. The unpromoted SZ sample was found to be fresh directly after calcination and after 68 days, whereas the thulium promoted SZ sample was measured with a time difference of 39 days. Differences of the four catalytic measurements are in the error bar of the setup. Obviously, it was possible to reduce the effect of aging drastically, so that no differences in the catalytic performance of a SZ sample were visible after a storage time of 68 days. Aging can be avoided for promoted and unpromoted samples in the same way. The difference in height of the maximum activity is a common measurement inaccuracy for the maximum activity of SZ samples, due to a rapid increase of activity in a short time span.

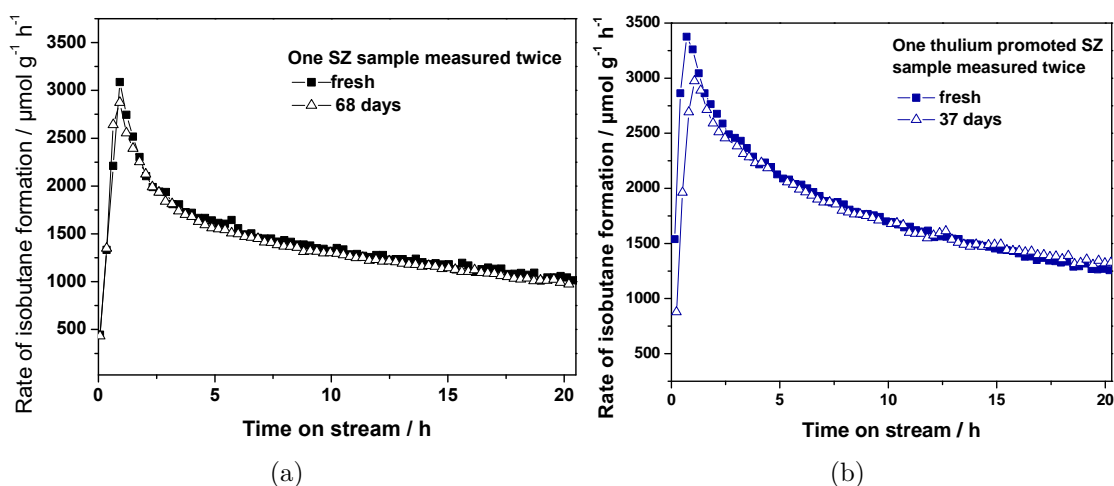


**Figure 4.3.:** Successful avoidance of catalyst aging. Rate of isobutane formation of a fresh SZ and after more than one month of storage, (a) unpromoted SZ catalyst (b) thulium promoted SZ catalyst after optimization of the storage conditions. The samples were stored in double containers, which were placed in a secador desiccator cabinet.

With further optimization of storage conditions, the effect of aging could be reduced so drastically that the catalytic performance of SZ samples remained unchanged after more than two months. This precondition makes it possible to compare the catalytic performances of large series of samples. It should be noted that the present work is the first to report about aging process being reduced to a negligible degree through elimination of air exposure, with the result that a comparison between fresh and samples kept under optimum conditions for month does not yield any significant differences. Even after optimization, Klose [104] still found a difference of 25 % in the rate of isobutane formation for two promoted samples with an age difference of only one week.

All investigated samples in this work, the promoted as well as the unpromoted ones, stayed in the tetragonal form. An increase of the monoclinic phase could not be detected in any of the samples. This shows that aging is predominantly a surface effect and demonstrates that well-prepared and stored catalysts can be kept in their metastable structural state that is responsible for high catalytic activity. Bolis et al. [105], with the help of IR investigation, observed that the first contact of water with the bare surface gave rise to a large amount of adsorbed species that were not removable by simply evacuating the sample at room temperature. This implies that the catalyst is easily modified by traces of water and is difficult to restore. Only when the storage conditions deteriorate, for example by storage in a humid or oxygen-depleted atmosphere in a glove box, as described by Klose [104] does the effect of aging result in structural changes of the bulk structure, resulting in monoclinization of the sample. Since the catalytic activity of a 6-month-old sample decreased disproportionately under tropical conditions, in comparison to the degree of transformation into the monoclinic phase, Klose [104] concluded that the fraction of tetragonal phase material which is most active is converted most easily. This conclusion could not be confirmed for moderate storage conditions because aging is mostly a effect of the catalyst surface reacting with the atmosphere.

## 4.2. Conclusion

Butane isomerization on sulfated zirconia requires careful handling and storage of the catalyst powder. Small differences between differently prepared or treated SZ

catalysts can only be studied, if the contact of the catalyst with air is limited as small and short as possible.

Catalyst aging starts at the moment of first exposure of the sample to air after opening a well-stored sample. Given optimum storage conditions, the influence of the time span between preparation and the first opening of the container is negligible. Water adsorption on the catalyst surface was found to be the main reason for catalyst aging. The present work assumes that when the catalyst is activated before its reaction, small amounts of labile sulfate groups, which are adhere to the adsorbed water on the sample surface, are desorbed from the surface along with the water. This results in higher L/B ratios for aged catalyst material (Fig. A.2). Catalyst aging in nearly 100 % phase-pure tetragonal samples, however, is a phenomenon of the catalyst surface and does not lead to the monoclinization of its structure.

The following points were found to reduce catalyst aging in laboratory practice to a minimum:

- The catalyst has to be put in a storage container while it is still warm, thus immediately after calcination.
- Reduction of the amount of humidity in the catalyst container is required.
- Storage with a double container technique as described above guarantees for the "freshness" of catalysts even after consumption of catalyst material from the same container.
- Storage of the containers in a vacuum desiccator or secador desiccator cabinet is essential.
- Exposure to air which is unavoidable for sampling has to be kept as short as possible.

## 5. The evolution of an active catalyst material in the course of thermal treatment

From what is being said in the literature, it remains unclear in which way active SZ catalysts develop. Calcination is critical in the preparation of these materials [28, 34]. Sulfated zirconia catalysts are typically obtained through the calcination of amorphous precursor material at 500-700°C. Many of the processes that are important for the properties of the final product already occur while the raw material is being heated up to the final calcination temperature (Sec. 1.5.1). These processes are: water loss, decomposition of precursor species (ammonium), crystallization and sintering (loss in surface area). The latter two reactions are strongly exothermic and frequently lead to an overheating of the sample known as the glow phenomenon. This exothermic glow can be observed for many catalytically relevant oxides, e.g. zirconia, titania and chromia. Hahn et al. [28] proposed that the active phase of sulfated zirconia is formed rapidly during the glow and that defects are quenched during this process. The examination of this relationship between the ongoing calcination process and the evolution of an active catalyst is presented in the paper on hand. We were trying to find out seeking to resolve whether the formation of the active metastable tetragonal catalyst does indeed take place in a short time interval of several minutes during the exothermic reaction, or whether this rather is a slower, gradual process. For that purpose, a variety of properties were investigated in detail, that is, in the form of quenching experiments, during calcination and, particularly, within the narrow time span of the glow phenomenon. A deeper understanding of the details of this transformation will allow for a knowledge-based optimization of the calcination procedure in order to produce an active defective catalyst material.

## 5.1. Results and discussion

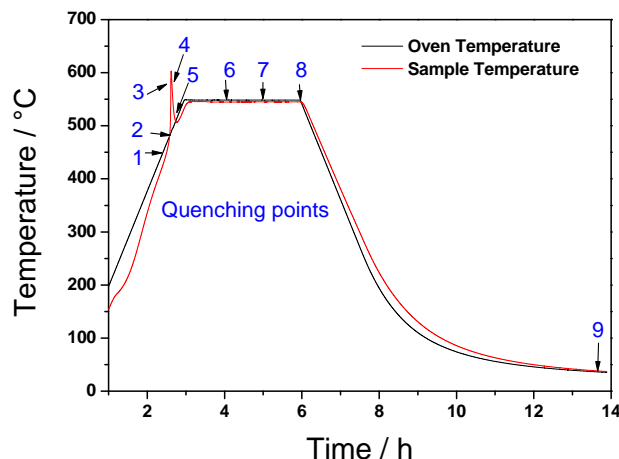
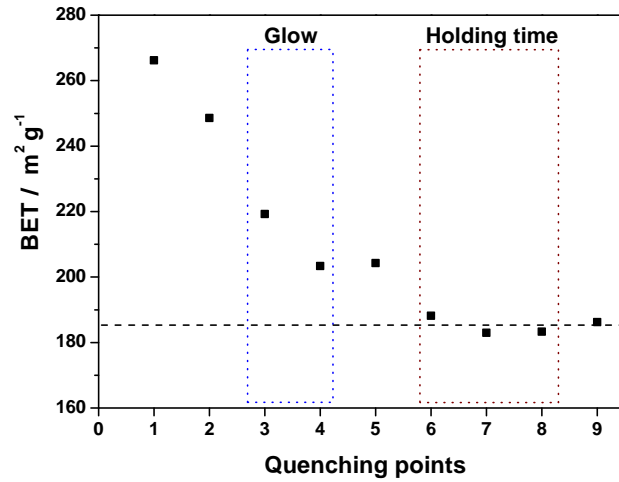


**Figure 5.1.:** Calcination program with indicated points of quenching experiments

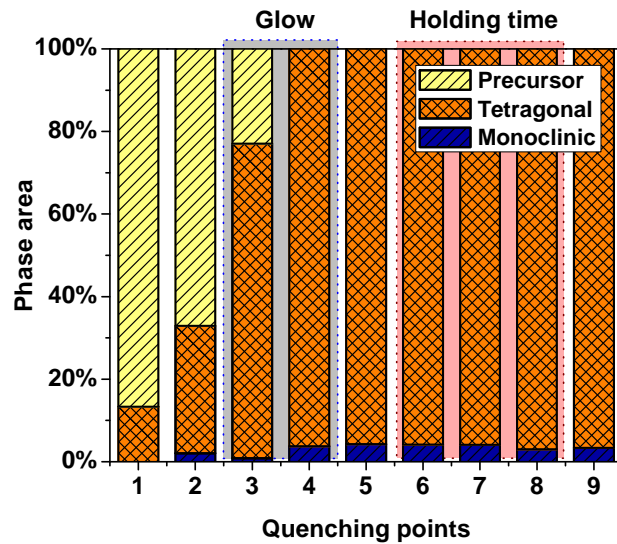
Figure 5.1 demonstrates the calcination program of unpromoted amorphous precursor material in a vertical tubular furnace. During the heating ramp, at oven temperatures of 480 °C to 510 °C, a rapid temperature rise from 465 °C to 603 °C was observed within 10 min inside the sample bed. This effect is known as glow phenomenon (sec. 1.5.1). The indicated numbers in the graph give the sampling points of the quenching experiments. These numbers are given in the images of this chapter. At these points, the experiment was interrupted and the sample was quenched in that the sample holder was dropped in a dewar vessel filled with liquid nitrogen.

Samples could be timetabled to a second during the exothermic reaction and differ in their characteristics. They follow a general trend: Surface area loss and crystallization are gradual processes. Figure 5.2 illustrates that the surface area decreases from 265 m<sup>2</sup>/g at 450 °C in the heating period to 185 m<sup>2</sup>/g after 1 h on the temperature plateau and remains stable at this value.

About 15 % of the material is crystalline in the heat up ramp at 450 °C (Fig. 5.3). In the following time span of the heat overshoot, crystallisation is very fast. At 480 °C, the temperature at which the glow phenomenon starts, 64 % of the material is still amorphous, the tetragonal phase amounts to 30 % and about 3 % are monoclinic. Some seconds later, at the second quenching point, which is to be located one second



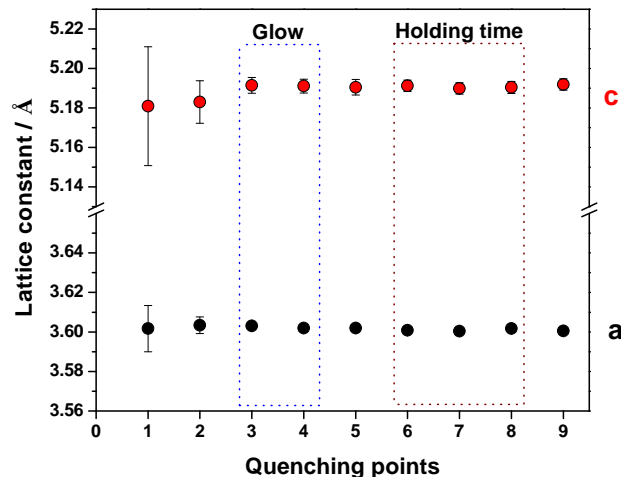
**Figure 5.2.:** Development of the BET surface area during calcination



**Figure 5.3.:** Development of the phase composition during calcination

before the glow maximum temperature, 74 % of the material already is tetragonal. Two seconds after the temperature maximum, the structure is completely crystalline according to XRD. The material is tetragonal with an amount of 3 % monoclinic phase and maintains in its composition. After occurring first at 480 °C, the amount of monoclinic phase material is constant throught the entire process of calcination. The monoclinic phase might already be present at 450 °C, but the high amount

of amorphous phase at this point made it impossible to detect a small amount of monoclinic phase.



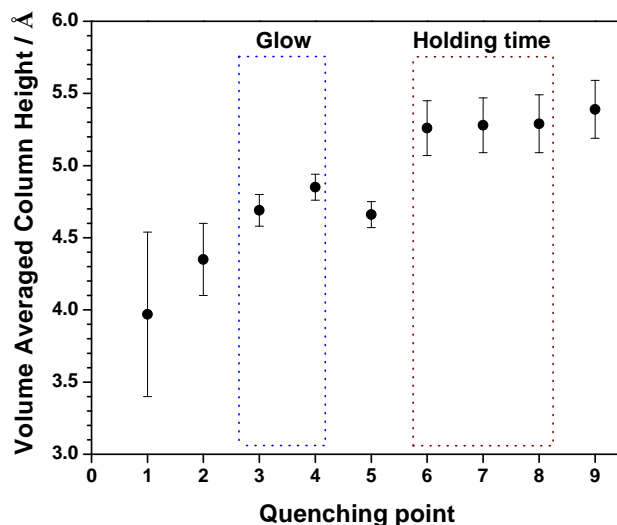
**Figure 5.4.:** Evolution of lattice parameters during the calcining program

Figure 5.4 illustrates the lattice constants  $a$  and  $c$  during calcination. The accuracy of the values for the lattice constants increases from the first quenching point to the third one, due to the decrease in the amount of amorphous phase material. Lattice parameters are fixed at the temperature maximum of the heat overshoot with averaged values  $a = 3.6011(4)$  and  $c = 5.191(10)$ . The crystalline size increases (Fig. 5.5) for rising temperatures from 4.0 nm at 480 °C to 5.3 nm at the temperature plateau of the calcination after 1 h. At this point, crystal growth is completed.

Figure 5.6 shows the evolution of the band gap energy for zirconia. The band gap energy at 450 °C is 4.5 eV, it increases up to a value of value of 5.1 eV, which is reached at the temperature maximum of the glow phenomena. Interestingly enough, the band gap energy increases within 2 s from 4.7 eV to 5.1 eV during the glow phenomenon between quenching point 3 and 4. This shows that the evolution of the electronic structure is related to the glow phenomenon. The direct band gap energy of tetragonal zirconia is typically given with 5 eV [106] in the literature which matches the values we obtained.

Activity in  $n$ -butane isomerization was first observed for that catalyst which was quenched one second before the temperature maximum of the glow phenomena with a value of  $52 \mu\text{mol g}^{-1}\text{h}^{-1}$  (value after 20 h reaction) (Fig. 5.7). It increases up to  $394 \mu\text{mol g}^{-1}$  at the maximum rate of isobutane formation for the catalyst which





**Figure 5.5.:** Development of the crystalline size during calcination

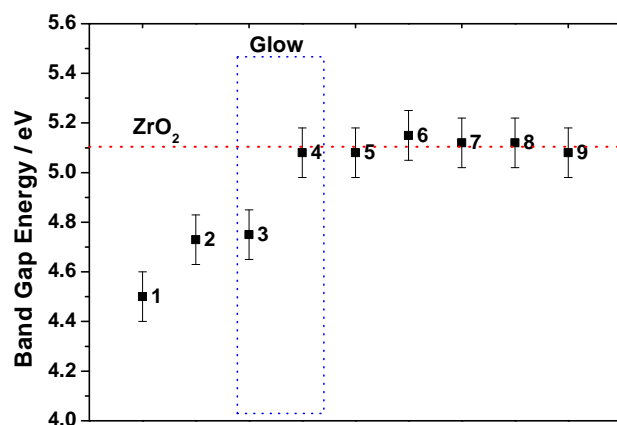


**Figure 5.6.:** Evolution of the band gap in SZ during calcination

was quenched after 2 h of holding time on the temperature plateau of calcination, after which the isomerization rate slightly decreased to  $314 \mu\text{mol g}^{-1}\text{h}^{-1}$  (after 3 h holding time). The development of catalytic activity of tetragonal SZ is a gradual process, in which the catalytic activity still changes after structural parameters and surface area have reached stable values. This fact suggests further structural and chemical modifications of the surface on the temperature plateau at  $550^\circ\text{C}$ .

All processes during the calcining program are gradual ones. The first processes, which are completed during the calcination procedure, or more precisely, in the course of the glow phenomenon, are the evolution of the tetragonal and of the

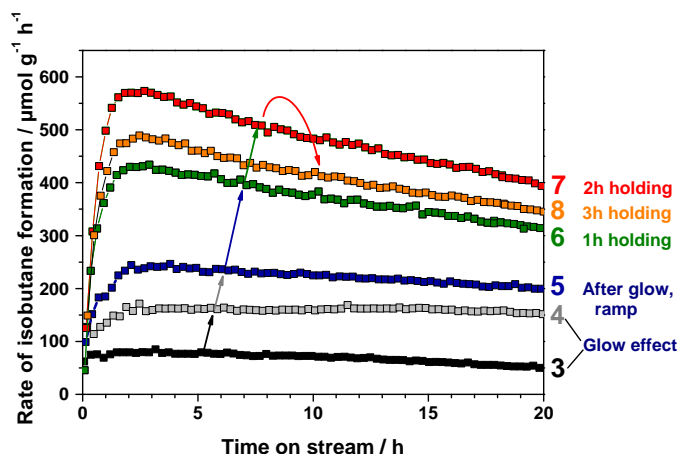


**Figure 5.7.:** Evolution of the catalytic performance during calcination

electronic structure. This shows the relevance of the glow phenomena for the structure of the investigated material. Nevertheless, the results demonstrate that in order to get an active catalyst, this is not sufficient. The surface area still decreases while the particle size still increases after the glow phenomenon, and as a result of these ongoing bulk and surface modifications, catalytic performance further increases. It is assumed that the defect structure is still modified after the glow phenomena due to the high temperatures. Defects are thought to migrate to the material's surface resulting in surface modification.

Earlier results given by Hahn et al. [34] were focused on the influence of the glow phenomena on differently prepared promoted and unpromoted samples. The authors correlated the temperature of the glow phenomena and the temperature of the oven at the time when the phenomenon takes place with parameters like the promoter content and the catalytic performance of the final product. In addition to that, the results of the present study show that the calcination conditions after the glow phenomena during the heat-up period of the calcination, are crucial for the definition of the catalyst's bulk and surface structure, and consequently, for the quality of the final product. Therefore, it can be assumed that the structural as well as the surface parameters change during calcination and both define an active SZ catalyst.

## 5.2. Conclusion

The series of quenching experiments show that the evolution of the electronic structure, surface area, crystalline structure/size and catalytic activity of SZ are closely linked. The glow phenomenon is an event within a gradual process of bulk phase evolution.

We were able to differentiate the characteristics of samples, taken at one second intervals during the exothermic reaction and establish that they follow a general trend. It could be shown that the samples were not damaged by nitrogen treatment. Surface area loss and crystallization are gradual processes completed at the maximum temperature of the heat overshoot. With the end of the glow phenomena phase composition, lattice parameters and the electronic structure are defined. The crystalline structure is established during the short time span of 20 min. Crystal growth is completed after 1 h on the temperature plateau of 550 °C. The development of catalytic activity of the metastable tetragonal phase is a gradual process, starting at the temperature overshoot, with a main increase in catalytic activity in the time window between the completed glow phenomena and the first hour on the temperature plateau. The final steps at this temperature are thought to be surface modification due to ongoing changes in the defect structure (migration to the surface) and modification of the surface sulfate groups due to interaction with the gas phase both influencing catalytic activity.

In order to obtain an active catalyst, a metastable tetragonal SZ needs to be formed, while extensive crystal growth and conversion into the thermodynamically stable but less active monoclinic modification through thermal activation are to be avoided. The conversion of a hydroxide into an oxide produces water, and sulfate is easily decomposed into volatile oxides. These reaction equilibria are governed by local partial pressures. The results show that the tetragonal phase itself is not sufficient for an active catalyst. In order to form an active defective material, further bulk and surface modification are necessary after the glow phenomena in the process of calcination.



## 6. Optimization of the calcination procedure

The aim of this chapter is to answer the question whether the systematically changed calcination parameters influence the bulk and / or the surface properties of SZ, and whether defects in the bulk structure of the material influence with these properties. In the literature only a few calcination parameters are investigated, while others are neglected (e.g. gas flow rate and defined oxygen partial pressure). For the parameters investigated most often the calcination temperature or time, contradictory results were found [30, 107]. In the present study, it is assumed that the different results could originate from different calcination geometries or setups, which are used by different working groups, since earlier studies showed that calcination boat geometry and size influence the resulting catalyst [28]. For this reason, upscaling the calcination procedure was not possible without losing control over the material properties. Furthermore, hot spots like the glow phenomenon (the origin of geometrical and size effects), have to be avoided in industrial production. Therefore, optimization was performed in an agitated sample bed in a horizontal rocking furnace instead of using a compact sample bed.

Our aim was to investigate a potential correlation between the different series of calcination parameters, material properties, like the particle size, the L/B ratio and the catalytic activity systematically. Nascimento et al. [22] proposed in 1993 a correlation between the L/B ratio of acid sites on the catalyst's surface and its catalytic activity. Morterra et al. [74] stated that the L/B ratio depends on the preparation procedure, the calcination temperature resulting in an amorphous, monoclinic or tetragonal structure, and the hydration/dehydration state (activation temperature). We expected these parameters to change the L/B ratio on the surface of tetragonal samples under varied calcination conditions as well.

## 6.1. Results and discussion

The following parameters were optimized for a given precursor material in a completely air-tight rocking furnace: plateau temperature during calcination, holding time, oxygen partial pressure of the gas flow, and the gas flow rate (Tab. 6.1). For the individual series the other parameters were kept constant at optimum conditions: 550 °C, 3 h holding time at the temperature plateau, 500 ml flowing 100 % Ar. Optimum conditions were defined as maximum rate of isobutane formation after 20 h. With the help of the rocking furnace, we succeeded in calcining our samples without any hot spots in the material, which means, in practical terms, in avoidance of inhomogeneous heat distribution (Sec. 1.5.1) during the heat-up ramp in the process of calcination. 20 g of starting material were used in each experiment. The catalysts were calcined in a calcination tube with a volume of 2 L.

**Table 6.1.:** Varied parameters

Parameter	Varied range
Holding temperature	525 -650 °C
Holding time	1 -21 hour
Oxygen partial pressure	0 -100 %
Gas flow rate	100 -900 mL

### 6.1.1. *n*-Butane isomerization

We managed to distinguish the catalysts according to their characteristics for all investigated parameters. The isobutane formation rate after 20 h on stream, as well as the long-term deactivation rate constants, are shown in Figure 6.1. The best results were obtained for a catalyst that had been calcined at 550 °C for 3 h at 500 mL/min flowing 100 % Ar. The rate of isobutane formation for this catalyst is  $981 \mu\text{mol g}^{-1}\text{h}^{-1}$  after 20 h on stream; its long-term deactivation rate constant is  $2.1 \cdot 10^{-5} \text{g } \mu\text{mol}^{-1}$ .

Deviating from this result, during optimization for the lowest long-term deactivation rate constant it turned out that the best catalyst is one which is calcined for only 1 h and yields a long-term deactivation rate constant of  $1.8 \cdot 10^{-5} \text{g } \mu\text{mol}^{-1}$ . The catalyst with the lowest isobutane formation rate and the highest long-term

deactivation rate constant is the one which was calcined at 650 °C. Time and, in particular, temperature have the strongest influence on the catalytic properties of the resulting catalyst. However, also the gas flow rate and the oxygen partial pressure lead to relative changes of up to 17 % for rate and 27 % for stability.

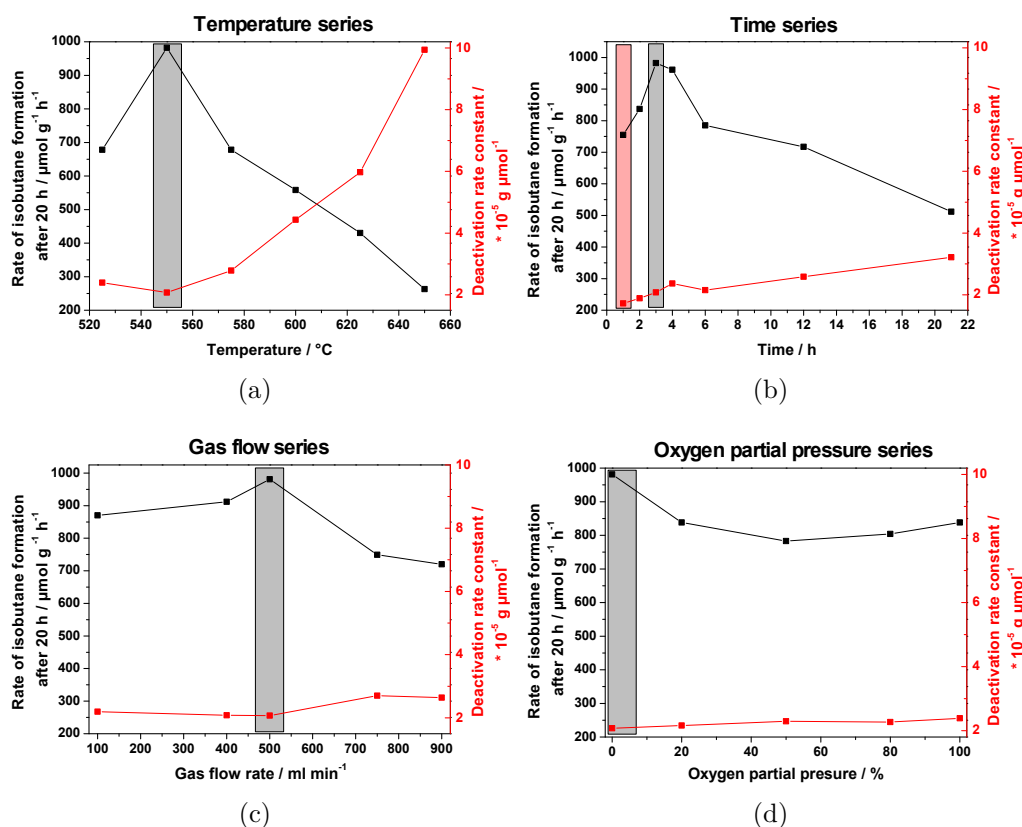


**Figure 6.1.:** Comparison of the rate of isobutane formation after 20 h on stream (black) with the deactivation rate constant (red) for different conditions during calcination (a) temperatures, (b) time, (c) argon gas flow, (d) oxygen partial pressure. For the individual series the other parameters were kept constant at optimum conditions: 550 °C, 3 h holding time at the temperature plateau, 500 ml flowing 100 % Ar. The optimum conditions after optimizing the rate of isobutane formation after 20 h are marked with a shaded box, deviating results for the time series after optimization of the deactivation rate constant are highlighted in a reddish box.

### 6.1.2. Determination of the BET surface area

Since all sulfate-containing samples are made of the same precursor, it can be assumed that they all have a BET surface areas nearing  $425 \text{ m}^2$  before calcination. The BET surface area changes if calcination conditions are changed. Figure 6.2 illustrates changes of temperature and time within the series, while it should be noticed that neither the oxygen partial pressure nor gas flow rate were varied. The greatest change in surface area was found for calcination at different temperatures.

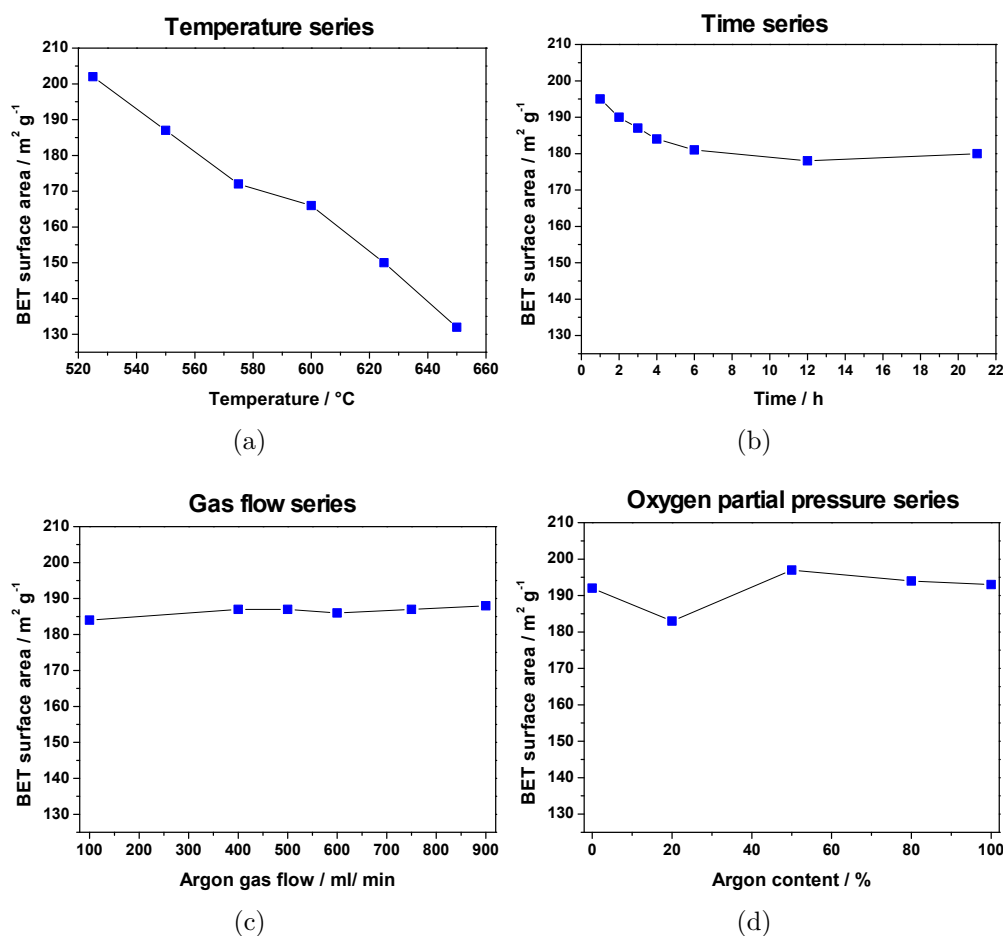


**Figure 6.2.:** Comparison of the BET surface area for different conditions during calcination (a) temperatures, (b) time, (c) argon gas flow, (d) oxygen partial pressure. For the individual series the other parameters were kept constant at optimum conditions:  $550^{\circ}\text{C}$ , 3 h holding time at the temperature plateau, 500 ml flowing 100 % Ar.

The surface area decreases from  $202 \text{ m}^2 \text{ g}^{-1}$  at  $525^{\circ}\text{C}$  to  $132 \text{ m}^2 \text{ g}^{-1}$  at  $650^{\circ}\text{C}$ . In



the time series, the surface area decreases from  $195 \text{ m}^2 \text{ g}^{-1}$  after 1 h to  $181 \text{ m}^2 \text{ g}^{-1}$  after 4 h on the temperature plateau at  $550^\circ\text{C}$  and remains stable at this value for 21 h (Fig. 6.2). It is interesting to note that the best catalytic properties do not correlate with the highest surface area neither in the temperature series nor in the time series.

### 6.1.3. Determination of the sulfate content

The sulfate content after calcination was determined by ion chromatography (Sect. 2.4). Figure 6.3 shows that the sulfate content decreases in an almost linear way for increasing calcination temperatures. Generally, the combination of calcination at high temperatures, low sulfate content, low catalytic performance, and low surface area can be found quite often in the literature. Furthermore, the decrease in sulfate content for increasing calcination time (Fig. 6.3) confirms results obtained by Li et al. [30] showing decreasing sulfate contents for prolonged calcination times.

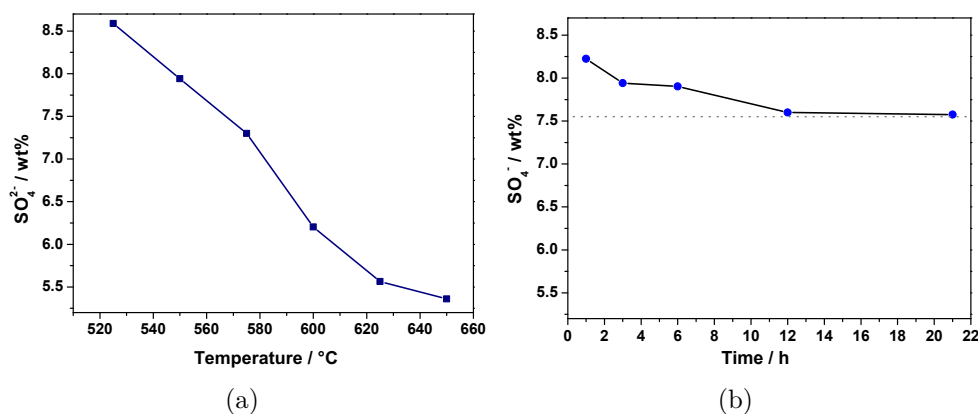


**Figure 6.3.:** Calcination (a) temperature and (b) time of unpromoted SZ catalysts versus its surface sulfate content after calcination. The sulfate content decreases for increasing temperature and time. The sulfate content was determined by ion chromatography.

### 6.1.4. SEM results

Figure 6.4 illustrates SEM images of SZ agglomerates at the endpoints of the respective series. No significant differences can be found between samples calcined at different temperatures, while oxygen partial pressure influences both size and

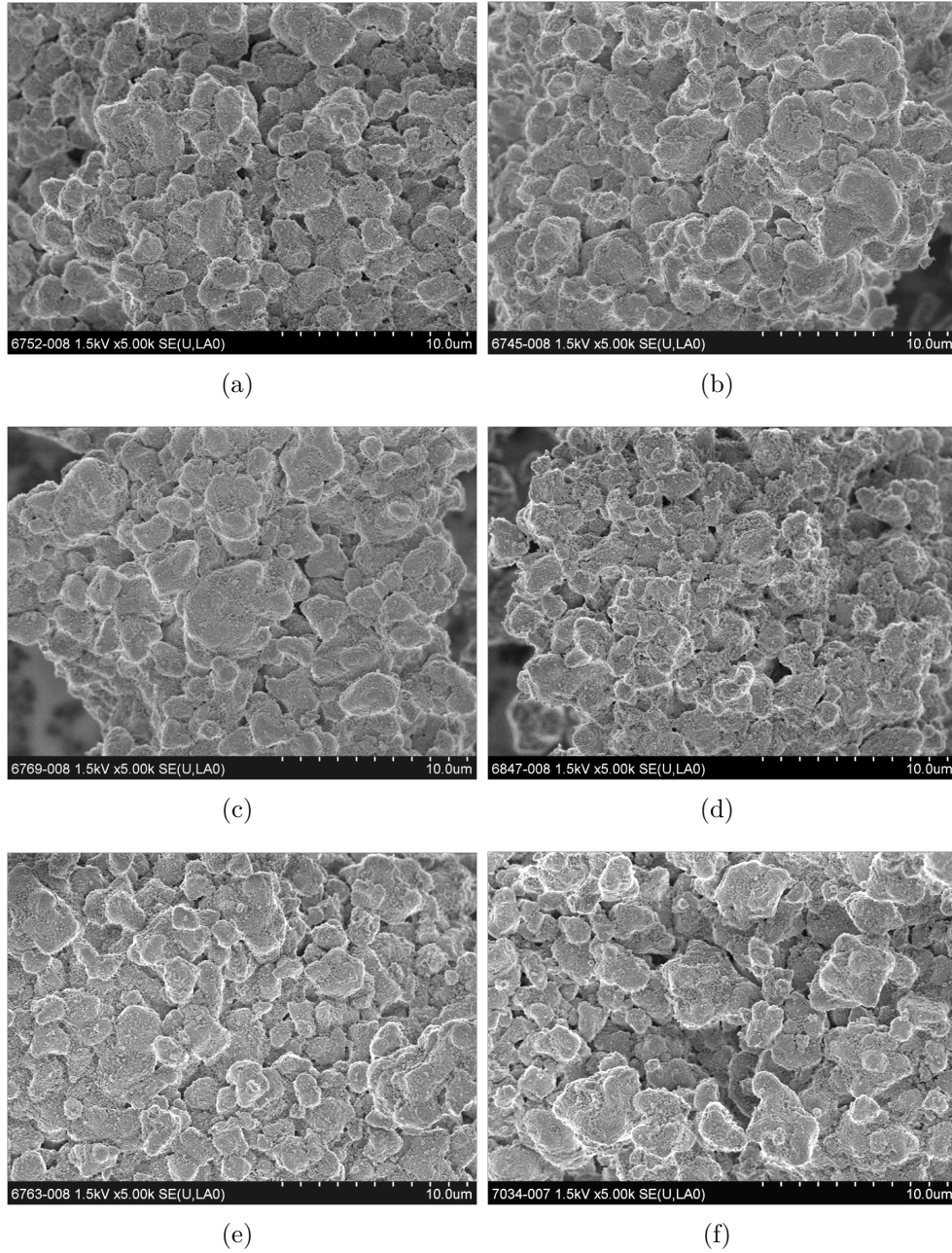


**Figure 6.4.:** SEM images of the endpoints of the different calcination series (a) temperature: 525 °C, (b) temperature: 650 °C, (c) oxygen partial pressure: 0 %, (d) oxygen partial pressure: 100 %, (e) time: 1 h, (f) time: 21 h. Differences are visible in the temperature series (sintering) and the oxygen partial pressure series (differences in particle roughness). These differences between the samples are only visible in low magnification images of the secondary particles.

morphology of the agglomerates. The sample calcined in 100 % argon is characterized by comparatively big and smooth agglomerates, whereas the sample calcined in 100 % oxygen displays a rough, irregular surface and smaller agglomerates. The images for the time series show a sintering of the agglomerated grains for longer calcination times.

### 6.1.5. XRD and TEM analysis

According to Rietveld refinement, all investigated samples described in this chapter are tetragonal with a marginal amount of maximum 3 % monoclinic phase. The determination of crystalline size was performed with a double Voigt approach and with the size and strain model, both of which are used by the program *Topas*. Figure 6.5 contains XRD peak profiles and TEM particle sizes for different calcination temperatures. Here, an increase in domain size as well as in grain size should be noted.

Since we did not find any changes in strain with the model used by the *Topas* program, a model combining XRD and TEM information, as described in Section 2.2, was used in order to search for changes of the apparent faulting probability in the tetragonal phase of the catalysts.

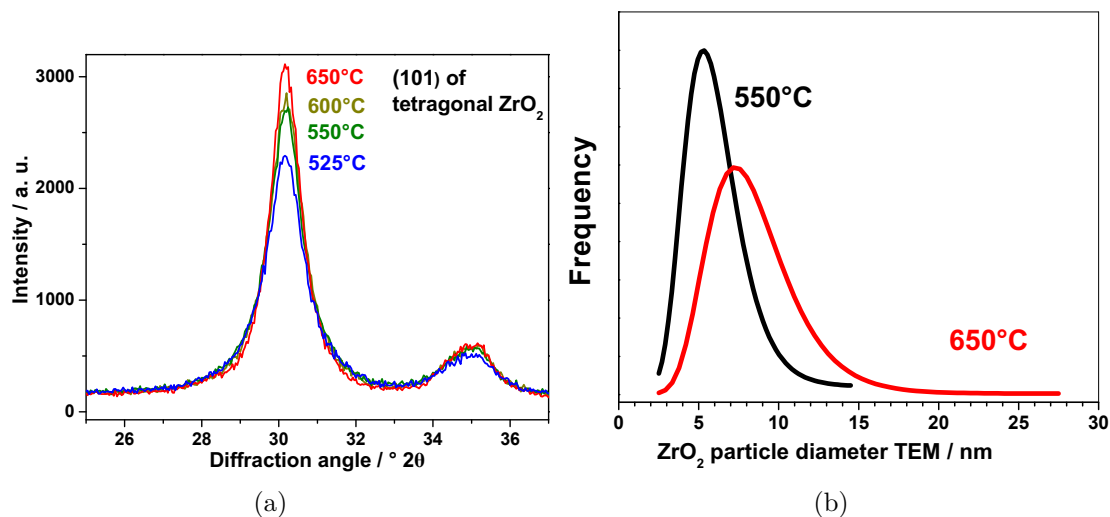


**Figure 6.5.:** (a) Shaping of XRD lines for increasing calcination temperatures, (b) increasing TEM grain sizes. The increase of particle size is caused by sintering.

### Defect analysis

Defect analysis was performed as described in Section 2.2.3 under the assumption of the Warren theory. In order to do so, pseudo Voigt fits of the XRD (101) peak were performed, and more than 1000 particles per sample were counted in TEM images. Figure 6.6 shows the particle size distribution derived from TEM images and XRD line profile analysis. Using this information and applying the Warren theory, the apparent faulting probability was determined for the temperature and time series, the series in which we had detected the most striking differences in catalytic performance (Fig. 6.1). Figure 6.7 illustrates an HRTEM image of the

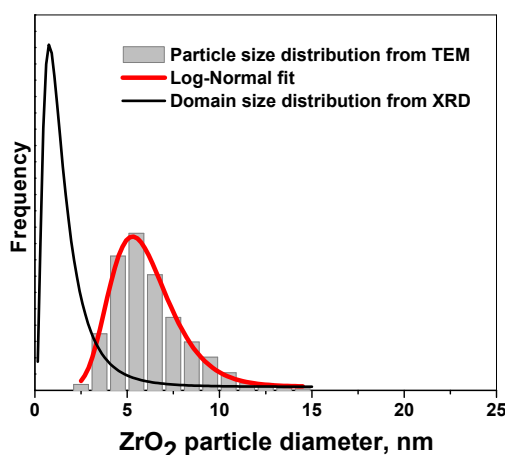


**Figure 6.6.:** Particle size distribution in TEM and XRD of the optimized catalyst. For the TEM particle size distribution more than 1000 particles diameters were measured.

optimized catalyst (550 °C, 3 h holding time at the temperature plateau, 500 ml flowing 100 % Ar). The most obvious defects to be seen under the microscope are the dislocation lines. In defect-rich particles, one can observe patch work-like structures of domains separated by dislocation lines.

Table 6.2 shows an increase in grain and domain size for rising calcination temperature while the relative apparent faulting probability and the sulfate content decrease. For increasing holding time during calcination, the development of the apparent faulting probability is more complex (Tab. 6.3). At first the relative faulting probability decreases between 1 h and 3 h, which is consistent with long-term deactivation rate constants increasing simultaneously. Between 3 h and 12 h,

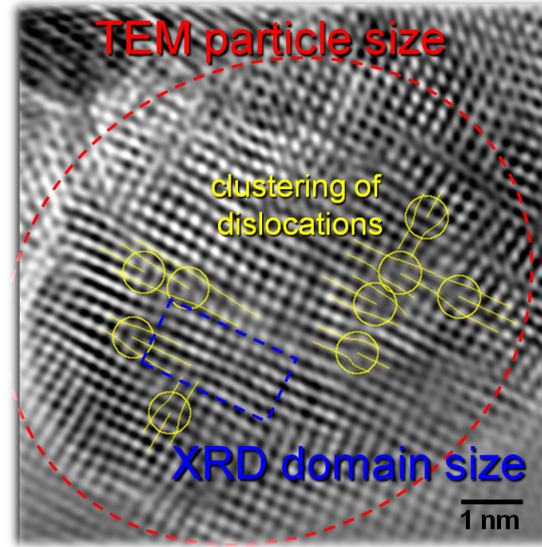


**Figure 6.7.:** TEM image of the optimized catalyst. TEM particle size and XRD domain size are visualized. Patch work-like structures of domains are separated by dislocation lines from each other.

**Table 6.2.:** Deactivation: temperature series

Sample	Domain size (XRD)/nm	Particle size (TEM)/nm	SO <sub>4</sub> <sup>2-</sup> /wt%	Faulting probability/rel. units	$c_{deact} / *10^{-5} \text{ g } \mu\text{mol}^{-1}$
550°C, 3h	1.70	6.02	7.94	1.00	2.1
650°C, 3h	2.57	8.45	5.36	0.64	9.8

**Table 6.3.:** Sample properties: time series

Sample	Domain size (XRD)/nm	Particle size (TEM)/nm	SO <sub>4</sub> <sup>2-</sup> /wt%	Faulting probability/rel. units	$c_{deact} / *10^{-5} \text{ g } \mu\text{mol}^{-1}$
1 h, 550°C	1.58	5.89	8.22	1.10	1.8
3 h, 550°C	1.70	6.02	7.94	1.00	2.1
12 h, 550°C	1.67	7.38	7.60	1.12	2.6
21 h, 550°C	1.80	7.40	7.58	1.01	3.2

however, the faulting probability seems to re-increases to its starting value while the deactivation rate constant further increases. This effect can be explained by sintering of the crystallites resulting in increasing particle sizes, which is not reflected in an

increase of the domain sizes. In the time span between 12 h and 21 h, the relative faulting probability shows the expected default behavior of decreasing faulting probability with time due to annealing at maximum particle size.

### 6.1.6. Determination of relative L/B-ratios

It was reported that catalytic activity does not depend on the total acidity of the catalyst surface [26, 79]. Furthermore, it was shown that only a small fraction of the sulfur located on the surface is responsible for the activity of a SZ catalyst [64]. Therefore, the relative L/B ratio is a valuable possibility to get relevant information concerning acid sites of the catalyst's surface. The L/B ratios were determined as described in Section 2.6.1. The acid sites were investigated with CO adsorption and IR measurements. Adsorption of CO was carried out at  $-196^{\circ}\text{C}$  with a CO pressure of 0.03 mbar. In comparison to the Brønsted sites, the bands of covered Lewis acid sites increase at an equilibrium pressure of  $p(\text{CO}) = 0.03$  mbar and with rising calcination temperature (Fig. 6.8), which meet our expectations.

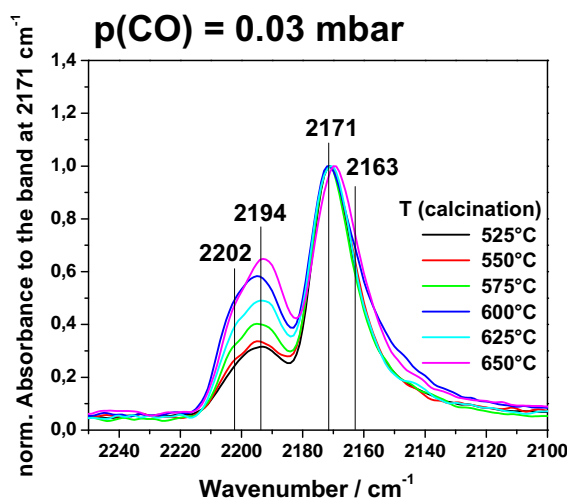


**Figure 6.8.:** Increasing relative amount Lewis acid sites for increasing calcination temperature (Brønsted sites are normalized to 1).

In the following, it is described why we believe special Brønsted acid sites to be relevant for the catalytic performance of SZ. Morterra et al. [108] showed that water deformation vibrations are connected to sulfate groups. Later on, Hofmann and Sauer [75] showed by theory that the sulfate groups on tetragonal SZ are disulfate

groups ( $\text{S}_2\text{O}_7^{2-}$  groups). Figure 6.9 illustrates that small quantities of  $\text{S}_2\text{O}_7^{2-} \cdot 2\text{H}_2\text{O}$  sites are present. A band assigned to  $\delta(\text{H}_2\text{O}_{\text{ads}})$  in  $\text{S}_2\text{O}_7^{2-} \cdot 2\text{H}_2\text{O}$  and detected at  $1598\text{ cm}^{-1}$  shifts to  $1598\text{ cm}^{-1}$ . This shift starts at a very low CO pressure and

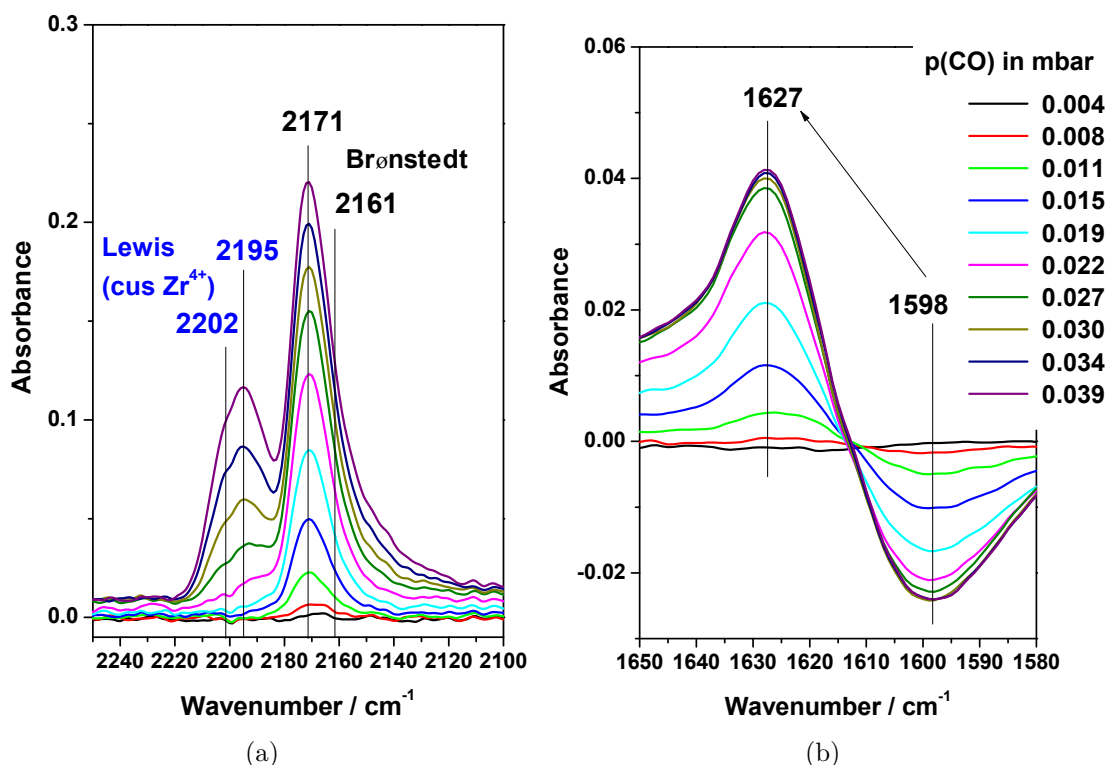


**Figure 6.9.:** IR difference spectra of CO adsorption on unpromoted SZ at  $-196\text{ }^{\circ}\text{C}$  illustrating the relevant spectra ranges for the determination of Lewis and Brønsted acid sites. (a) Carbonyl stretching vibrations, (b) shift of  $\delta(\text{H}_2\text{O}_{\text{ads}})$  in  $\text{S}_2\text{O}_7^{2-} \cdot 2\text{H}_2\text{O}$  correlates with the formation of the band at  $2171\text{ cm}^{-1}$  and  $2162\text{ cm}^{-1}$ , which are formed due to CO adsorbed on Brønsted sites.

ends at approximately 0.03 mbar (the investigated CO partial pressure). This shift can be attributed to the formation of the band at  $2172\text{ cm}^{-1}$  which appears due to CO being adsorbed on Brønsted sites (Fig. 2.6). This means that special Brønsted sites are influenced by  $\delta(\text{H}_2\text{O}_{\text{ads}})$  in  $\text{S}_2\text{O}_7^{2-} \cdot \text{H}_2\text{O}$ . These Brønsted sites have to be situated in the neighborhood of  $\text{H}_2\text{O}$  in the disulfate, and they seem to become more acidic than the other Brønsted sites, because the CO first adsorbs on these sites at a very low pressure, whereas normally the Lewis acid sites would be covered first (CO adsorbs first on Lewis acid sites at room temperature). Therefore, we assume that they are the key to the enhancement of the catalytic performance. This

finding goes in hand with investigations made by Breitung et al. [109]. They claim that only a small part of the total amount of Brønsted are catalytically relevant. By selective poisoning of the more acidic Brønsted sites close to sulfate groups, they found that catalytic activity dramatically dropped down. In their case, the poisoned centers made up only 3 % of Brønsted centers close to sulfate groups. As a result of the poisoning process, the absolute L/B ratio, determined by pyridine adsorption, increased due to a blockage of Brønsted centres.

Gradual changes in the relative L/B ratio could be visualized. Generally, low L/B ratios correlate with high catalytic performance (Appendix Fig. A.2 (b)) and vice versa. This is in agreement with the results obtained for surface modified unpromoted SZ catalysts as well as for thulium-promoted catalysts (Sects. 7.1.4 and 8.1.6). The optimized catalyst had a relative L/B ratio of about  $0.25 \pm 0.02$  units. A similar L/B ratio for an optimized catalyst was reported by Ward and Ko [25], who used diffuse reflectance infrared fourier transform (DRIFT) spectroscopy to examine the spectra of adsorbed pyridine.

In the temperature series, gradually decreasing calcination temperatures entailed a gradual decrease in the L/B ratio with a region of unchanged L/B ratios between 525 and 575 °C (Fig. 6.10 (a)). In contrast to the gradual changes in the relative L/B ratio presented here with an optimum at 550 °C, Ward and Ko [25] did not find any gradual changes and reported high L/B ratios of 0.8 and higher for temperatures lower and higher than their optimum temperature of 600 °C. Surprisingly, they found Lewis acidity for a sample calcined at 525 °C, which would correspond to an L/B ratio of 1. Figure 6.10 (b) illustrates a slight decrease in the relative L/B ratio for higher *n*-butane formation rates in the gas flow series. For the calcination parameters time and oxygen partial pressure, the deviations in the parameters are more subtle (Fig. 7.5) and the gradual change is more difficult to see. Nevertheless, we were able to demonstrate a general trend of gradually decreasing relative L/B ratios with increasing catalytic activity.

The error of the measurement could be defined with the help of the sample calcined at 575 °C, which was measured twice in a short time interval, and is determined to  $\pm 0.02$  units, whereas the error of the preparation conditions on the relative L/B ratio for a sample prepared twice is  $\pm 0.01$  units.

Since it was not possible to investigate all samples within a small time interval and owing to multiple sampling for the different analytical methods – several samples



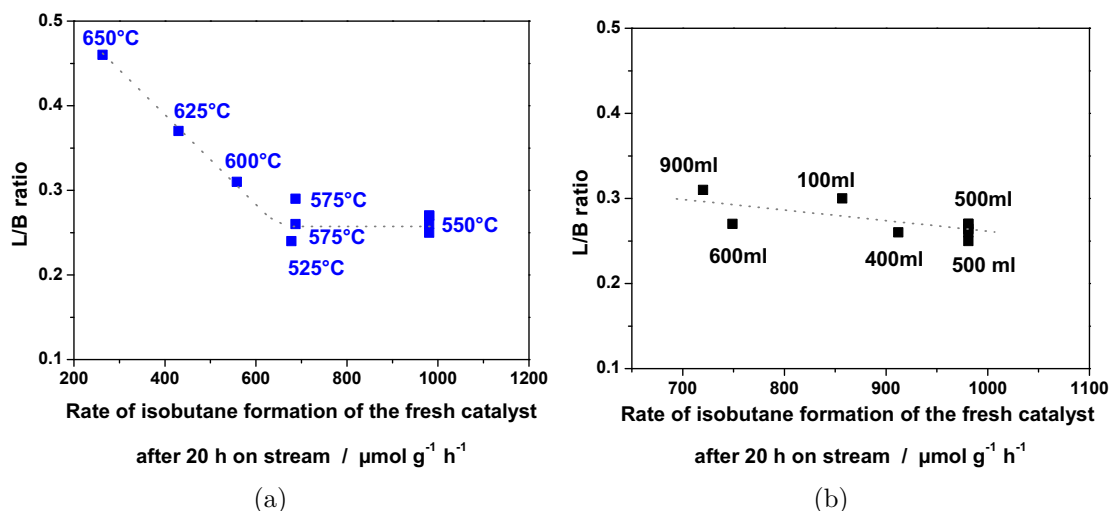


**Figure 6.10.:** Comparison of the relative L/B ratio after aging correction (Appendix Fig. A.1) for different (a) calcination temperatures (b) argon gas flow rates during the calcination procedure versus the rate of isobutane formation of the fresh SZ sample after 20 h.

show higher L/B ratios as expected more than 5 month after the first investigation with IR spectroscopy. This is a result of catalyst aging, which could not be completely avoided despite optimized storage conditions (Chap. 4) after sampling the same sample more than 15 time. In Figure 4.2 it was shown that the aged samples show a aging behavior in the course of time. As we were able to calculate the aging effect from samples which where measured twice (with a time difference of up to 7 month) the described effect could be corrected for aged samples (Appendix Fig. A.1). After correction, all highly active catalysts show low relative L/B values between 0.2 and 0.35 units (Appendix Fig. A.2).

## 6.2. Conclusion

We succeeded in calcining SZ under controlled conditions by minimizing the effect of bed and geometry. The end products were (highly) active in *n*-butane isomerization and, as a result, the gradually changing calcination parameters are reflected in different catalytic performances. With the help of systematic variation of the individual parameters during calcination (temperature, time, oxygen partial pressure, and gas flow rate), we were able to show that all parameters individually change the

quality of the final product. In all characterization techniques the largest differences were found for the factors temperature and time.

After optimization of the isobutane formation rate after 20 h, the optimum parameters for calcination (of 17 g in a calcination tube with a volume of 2 L) are: 500 mL/min flowing 100 % Ar at 550 °C for 3 h. The optimum catalyst is characterized by a high relative apparent faulting probability in its tetragonal structure, a low L/B ratio of acid surface centers, a high BET surface area, and a high sulfate content on its surface.

Two Lewis and two Brønsted acid sites were found at a CO partial pressure of 0.03 mbar, which correlate with the catalytic performance of SZ. At this pressure a small number of special Brønsted sites, which are influenced by  $\delta(\text{H}_2\text{O}_{\text{ads}})$  in  $\text{S}_2\text{O}_7^{2-} \cdot \text{H}_2\text{O}$ , are covered. Since they are very acidic, at low temperature they are covered first. These special Brønsted sites are the key to the enhancement of the catalytic performance. It could be shown that the calcination parameters temperature and gas flow directly influence the surface properties and, subsequently, the catalytic performance. For the parameters oxygen partial pressure and calcination time, the catalytic performance cannot simply be explained with the relative L/B ratio. In this case, other sample properties seem to be more relevant. The change in the rate of *n*-butane formation after 20 h with increasing calcination temperature can be attributed to gradual changes in the relative L/B ratio. Interestingly enough, this effect cannot be seen in the L/B ratio with time passing on the temperature plateau during calcination. For the calcination parameter time it can be concluded that bulk effects dominate surface effects.

In TEM investigations, it could be demonstrated that the most important manifestation of structural changes in apparent faulting probability can be seen in the temperature series. This series also shows the best correlations of the relative L/B ratio with catalytic performance. In the other series, the structural changes resulting from variation in the calcining parameters are smaller, which leads to changes that are much less easy to resolve in CO adsorption at low temperatures. As stated by Klose et al. [45], it is impossible to predict catalytic activity solely from the state of the functional groups of the catalyst's surface.

The sensitivity of the product properties to heat transfer and gas exchange conditions during calcination is striking. Most of the changed parameters have an influence on bulk structure as well as on the surface. Neither the bulk structure nor the

surface alone can account for the catalytic performance of the investigated material, because the apparent faulting probability within the bulk structure automatically influences the catalyst's surface properties.



## 7. Influence of gas phase loading during thermal treatment of unpromoted SZ

In Chapter 6 and 8 it is shown that defects in the bulk structure of SZ (dislocations) influence the sulfate groups on the catalyst surface and therefore the catalytic performance. This chapter deals with our investigation of the influence of gas phase loading with sulfate, sulfuric acid and water during calcination, and ex-situ post-treatment with sulfur trioxide after calcination respectively. Our hope was to obtain information about the magnitude of the effect of surface modification on catalytic activity, without having influences of the bulk structure. The starting point for this was the optimized unpromoted SZ catalyst (Chap. 6). The literature gives clear evidence that there exists such a relationship. Li et al. [101] found that SZ that had been prepared with the help of gas phase  $\text{SO}_3$  as a sulfating agent was highly active in *n*-butane isomerization. They were able to prove the influence of the presence of labile sulfate species on catalytic activity.

### 7.1. Results and discussion

#### 7.1.1. Catalytic results

Figure 7.1 shows the rate of isobutane formation versus time on stream for *n*-butane skeletal isomerization of the parent sample (optimized unpromoted SZ) at 100 °C, the water-treated sample (during calcination), the oleum treated sample (during calcination), the  $\text{SO}_3$  post-treated sample (after calcination) and the oleum-treated sample with additional  $\text{SO}_3$  treatment after calcination. Starting from the optimized unpromoted SZ catalyst, the rate of isobutane formation could be increased by the

## 7. Influence of gas phase loading during thermal treatment of unpromoted SZ

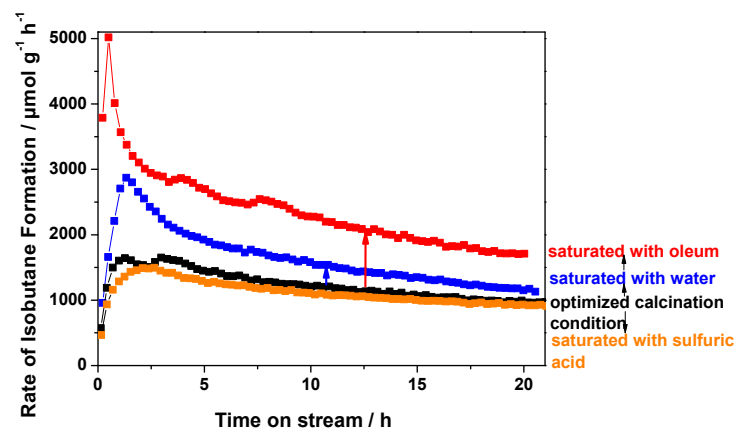


**Figure 7.1.:** Influence of different gas phase treatment during and after the thermal treatment on the *n*-butane isomerization of unpromoted SZ samples. Extra gas phase SO<sub>3</sub> (in a certain range) and water result in increased isobutane isomerization rates, while sulfuric acid has no positive effect.

use of oleum and water during the calcination process, or by a gas phase SO<sub>3</sub> post-treatment of the calcined optimized catalyst. Water-treatment during calcination is less effective than the addition of extra surface sulfate if one aims at increasing the rate of isobutane formation; even more water has a negative effect on the long-term deactivation rate constant (Fig. 7.2).

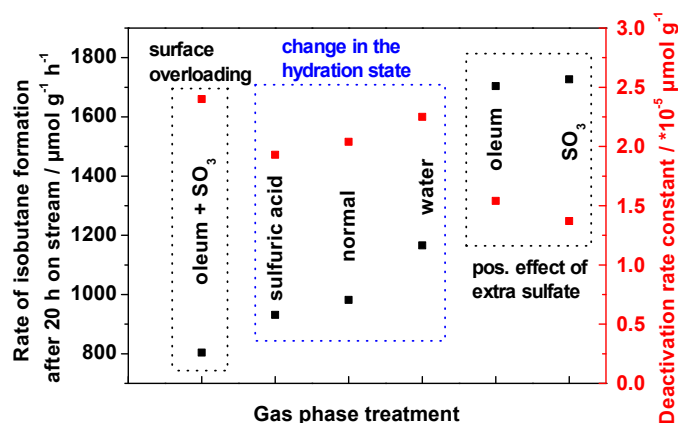


**Figure 7.2.:** Influence of different gas phase treatment during and after the thermal treatment on the rate of isobutane formation after 20 h on stream and on the deactivation rate constant of unpromoted SZ samples. Extra SO<sub>3</sub> has a positive effect on both parameters, whereas for a change in the hydration state, if one of the parameters has a positive influence the other one is changed at the same time in a negative direction.

On the other hand, oleum and  $\text{SO}_3$  post-treatment both increase the catalytic performance and, at the same time, lower the long-term deactivation rate constants drastically at constant values of the apparent faulting probability in the bulk structure as an indicator for a constant defect density. Although the oleum sample and the  $\text{SO}_3$  post-treated sample have different total sulfate loadings (Fig. 7.3), they yield similar results: isobutane formation rates nearly twice as high and a long-term deactivation rate constants nearly half of what it was before. Interestingly, the combination of both extra sulfate loading methods (oleum during calcination plus  $\text{SO}_3$  post-treatment), which yields a catalyst with the highest surface sulfate loading, has a negative effect on both parameters. The catalyst displays the lowest rate of isomerization and the highest deactivation rate constant. Changing the hydration state by using water or sulfuric acid has no remarkable positive effect, as both parameters increase or decrease at the same time: sulfuric acid, known as a drying agent, decreases the deactivation rate constant and simultaneously lowers the rate of isobutane formation (Fig. 7.2).

### 7.1.2. Sulfate loading and BET surface area

The results of Figures 7.1 and 7.2 demonstrate that the catalytic performance of an optimized catalyst can be further increased by gas phase loadings during or after the calcination process. Extra surface sulfate has a positive effect on the catalytic performance up to a total surface sulfate loading of 10.8 wt% after calcination for a surface of  $189 \text{ m}^2/\text{g}$  for the untreated SZ surface, while the surface decreases of about  $20 \text{ m}^2/\text{g}$  to  $173 \text{ m}^2/\text{g}$  (Fig. 7.3). Between sulfate contents of 8.4 and 10.8 wt% of the oleum and the  $\text{SO}_3$  post-treated sample, the catalytic performance and the BET surface area remain almost constant. Extra sulfate loading above 10.8 wt% after calcination result in an overloading of the surface. Probably, the monolayer sulfate is exceeded. This results in a steep decrease in BET surface area (Fig. 7.3) and catalytic performance (Figs. 7.1 and 7.2).

Our positive results between 0.5 and 4 wt% extra sulfate confirm the results of Breitung et al. [100], who stated that extra gas phase  $\text{SO}_3$  treatment could drastically enhance the catalytic activity up to one order of magnitude for a material that had been already sulfated before calcination. At the same time, the presented results also show the limits of this procedure. The fact that gas phase loading by

## 7. Influence of gas phase loading during thermal treatment of unpromoted SZ

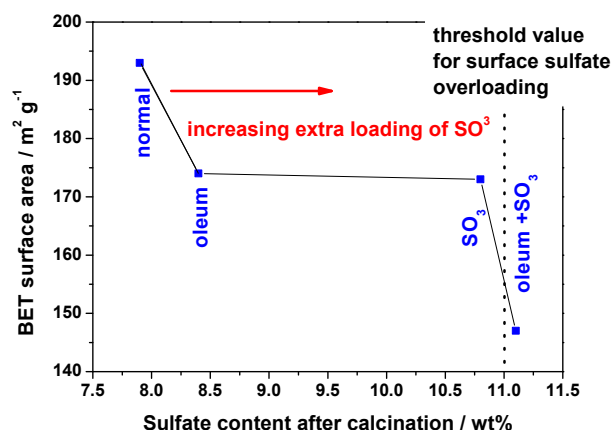


**Figure 7.3.:** Influence of increasing surface sulfate content on the BET surface area. The BET surface area is lowered by increasing sulfate content. Surface sulfate overloading, which is defined by more than 11 wt% sulfate, results in a further decrease of the BET surface area in comparison to the moderate sulfate contents with concentrations between 8.4 and 10.8 wt%.

oleum during calcination, which only has a small effect on the total sulfate loading, shows the same effect as gas phase  $\text{SO}_3$  post-treatment for the catalytic performance suggests that the addition of extra labile sulfate species on the catalyst surface already has a positive effect in a small concentration that cannot be improved by adding higher quantities. Furthermore, there is a limit of positive effect of surface sulfate concentration.

**Table 7.1.:** Influence of the hydration state on BET surface area and sulfate content

Treatment	Sulfate content / wt%	BET surface area / m <sup>2</sup> g <sup>-1</sup>
optimized	7.9	189
+ sulfuric acid	7.7	184
+ water	6.9	144

Table 7.1 shows that a change in the hydration state results in a decrease in BET surface area. While sulfuric acid does not significantly influence the surface sulfate content nor the surface area, water treatment during calcination leads to a lowering of both parameters: the surface area decreases of 45 m<sup>2</sup>/g and the sulfate content of – 1 wt% compared to the optimized catalyst without extra gas phase treatment.



### 7.1.3. SEM results

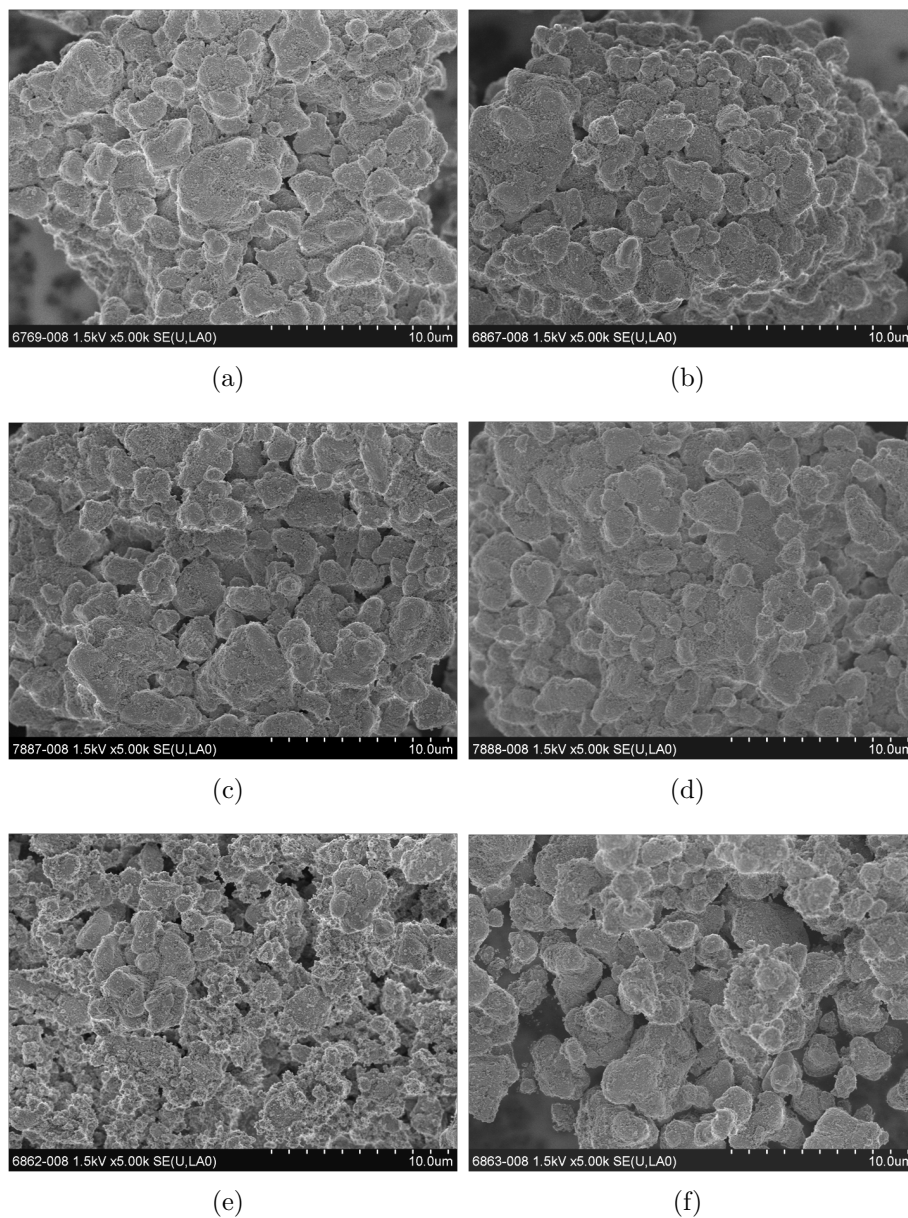


**Figure 7.4.:** SEM images for different gas phase treatments during or / and after calcination. (a) Optimum of the calcination optimization, (b) oleum during calcination, (c)  $\text{SO}_3$  post-treatment, (d) oleum during calcination +  $\text{SO}_3$  post-treatment, (e) water during calcination, (f) sulfuric acid during calcination. Extra sulfate on the catalyst surface has no effect on the morphology if the surface is not overloaded with sulfate, whereas a change in the hydration state has a influence on the roughness of the agglomerates.

Figure 7.4 illustrates the effect of gas phase treatment on the morphology of the agglomerates. Extra sulfate on the catalyst surface has no effect on the morphology if the surface is not overloaded with sulfate. Overloading of the surface results in a slightly smoothing effect on the morphology. A change in the hydration state has a big influence on the roughness of the agglomerates (Fig. 7.4 (e) + (f)). Both samples show more irregular agglomerates. This effect is also reflected in a decreasing BET surface area.

#### 7.1.4. CO adsorption on post-treatment SZ samples at -196°C

The relative L/B ratio was determined as described in Section 2.6.1. In contrast to the optimization series with their gradual changes in calcination parameters, the gas series is characterized by completely different gas phase treatments (water, sulfuric acid, oleum, SO<sub>3</sub> post treatment after calcination, and a combined treatment with oleum during and SO<sub>3</sub> after calcination). Nevertheless, we were able to confirm the general trend found in Subsection 6.1.6 could be confirmed: High relative L/B ratios correlate with low catalytic performance (Figure 7.5) and vice versa. The differences in the relative L/B ratios for different gas phase loadings are larger than within the former described calcination series.

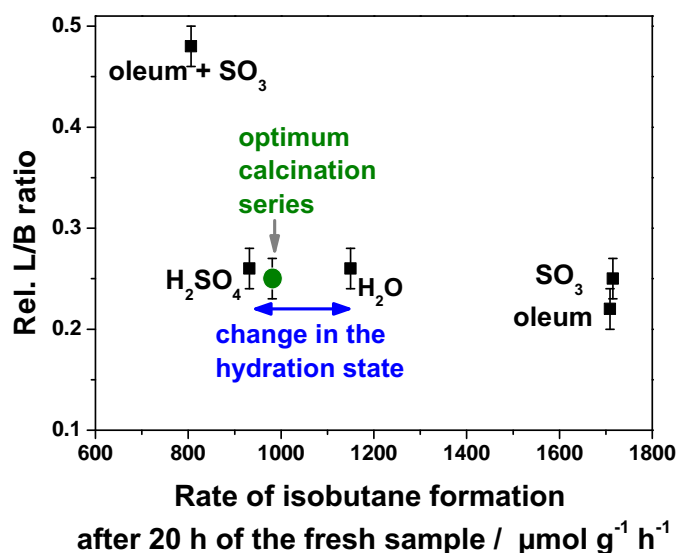


**Figure 7.5.:** L/B ratios for unpromoted SZ samples of the gas saturation series versus their rate of isobutane formation after 20 h. Low L/B ratios correlate with high catalytic performance and vice versa.

As described by Manoilova et al. [110], the labile sulfate groups, which are responsible for alkane activation, are removed by water washing and their amount is increased by  $\text{SO}_3$  sulfation after calcination. Water washing strongly weakened Brønsted acidity but only slightly weakened Lewis acidity. Morterra et al. [74] stated that Lewis acid sites are partially transformed into Brønsted sites if water is present. As described by Li et al. [101] the labile sulfate groups induce Brønsted acidity on the zirconia surface. A decrease in Lewis acidity after  $\text{SO}_3$  sulfation indicated that at least some of the labile sulfates were coordinately bound to the Lewis acid sites. Li et al. found that the increase in Brønsted acid sites went hand in hand with a significant decrease in zirconia surface OH groups, and they concluded that the Brønsted acid sites are affiliated with disulfate species. The statement that labile sulfate groups induce Brønsted acidity on the zirconia surface fit well together with the oleum treated sample shown in Figure 7.5, which shows the lowest L/B ratio and the highest catalytic performance. Unfortunately, the decrease in the L/B ratio, which should be present, is so small that it is not visible for our investigated  $\text{SO}_3$  treated sample. This shows that additional sulfate on the surface, which we measured with IC and which resulted in an almost doubled catalytic performance, only slightly influences the L/B ratio if the surface is not overloaded. Surface overloading by additional  $\text{SO}_3$  post-treatment of the oleum sample exhibits a very high relative L/B ratio of 0.8 units in combination with a very low catalytic performance. This again proves what has already been shown by the other characterization methods, namely that the  $\text{SO}_3$  extra treatment has a positive effect in a limited interval. An oversupply of sulfate seems to destroy Brønsted acidity for the benefit of Lewis acid sites, which are correlated with a low catalytic performance.

Interestingly, the L/B ratio of those samples saturated with  $\text{H}_2\text{SO}_4$  or  $\text{H}_2\text{O}$  did not change significantly, whereas the catalytic performance did in fact change. Since  $\text{H}_2\text{SO}_4$  is a well known drying material, both sulfuric acid and water should influence the degree of hydration of the zirconia and, as a consequence, change the L/B ratio. Cerrato et al. [23] found a dependency between couples of Lewis and Brønsted acid sites, which are necessary for catalytic activity, and the dehydration rate during calcination. They found an optimum ratio at a medium high degree of dehydration of the catalyst. This fits with our catalytic results but is not reflected in the L/B ratios. Li et al. [30] found water steam during the calcination procedure to have a

negative impact on the catalytic activity. They believed that synthetic air saturated with water would be negative for the formation of active sites. Moisture and  $\text{SO}_3$  were thought to compete for adsorption on SZ [30]. These results, however, could not be confirmed by our investigations.

## 7.2. Conclusion

It is possible to almost double the catalytic performance of an optimized, defect rich catalyst by the use of gas phase treatment with  $\text{SO}_3$  in a distinct interval. That means that for a defect rich bulk structure of SZ, the catalytic performance can be further increased by tuning the catalyst's surface properties. This fact further verify that both, bulk and surface properties, control the catalytic performance of SZ (see also Section 6.2). Small amounts of additional sulfate on the catalyst's surface between 0.5 and 3 wt% (values after calcination) increase the catalytic activity. The surface area shrinks when the surface is loaded with sulfate. Interestingly, oleum treatment during calcination and the gas phase  $\text{SO}_3$  loading ex situ after calcination, with different sulfate loadings resulting from each respective treatment, result in the same increase in catalytic performance and the same decrease in BET surface area at constant apparent faulting probability in contrast to the sample calcined normally. This proves that an increase in catalytic performance can be exclusively attributed to a change of the surface properties by gas phase treatment for a given defect-rich starting sample. Additional sulfate on the catalyst's surface below 3 wt% did not significantly change the L/B ratio of surface acid sites. In contrast to that, 3 wt% additional sulfate, with a total sulfate value of 11.1 wt%, was found to be a threshold value for an overloading of the surface with sulfate: starting from a surface area of  $193 \text{ m}^2/\text{g}$ , the result of overloading is a drop of  $47 \text{ m}^2/\text{g}$  in the surface area, a drastic increase in the L/B ratio of the surface acid sites, and a decrease in catalytic performance.

## 8. Effect of promoters and sulfate content on catalytic performance

Promoters as well as sulfate alter the properties of a given catalyst. This chapter presents a systematic evaluation as to which of the two parameters outweighs the other in its impact on the final product. This should answer the general question whether it is the bulk or the surface effects that are dominant and, consequently, which factor is most important during the catalyst preparation to improve the alkane isomerization on SZ.

For that purpose, we needed a promoter which (i) was incorporated into the tetragonal lattice of SZ, (ii) did not change the white color of SZ (in order to be able to perform UV-vis experiments) and (iii) did not distort the results of EPR investigations on SZ. Gillespie and Cohn [54] conducted industrial investigations on SZ catalysts and found that SZ material promoted with rare earth elements (REE) was very active in the conversion of light alkanes. Their hypotheses about REE being introduced into the tetragonal lattice of SZ are justified by well-known physical laws (Sect. 1.5.2). Investigations on ceramics made by Yashima et al. [111] have shown that REE dopants are incorporated into the cubic lattice of zirconia with a completely solid solution range and that Vegard's law can be applied. These facts lead to the conclusion that REE can be introduced into the lattice of SZ. For the present work we chose thulium as a heavy REE with a ionic radius of 113.4 pm in eightfold coordination [112].

Marcus et al. [64] reported that the amount of sulfate loaded onto the catalyst strongly determines its reactivity. Their results demonstrated that the number of active sites is generally very small. In order to increase the number of active sites it is necessary to prepare a pre-catalyst with most possible available sites on the catalyst surface through systematic variation of the bulk and surface properties. In this chapter, in a 'Tm series' the Tm content was varied between 0 – 5 mol%,

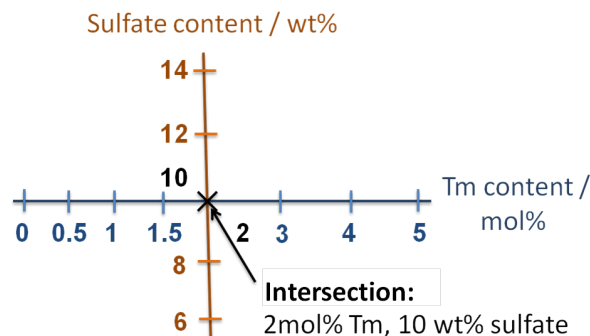


**Figure 8.1.:** Co-precipitated samples: thulium and sulfate series with their intersection at 2 mol% Tm and 10 wt% sulfate

as well as the sulfate content was varied independently between 6 – 14 wt% in the amorphous precursor material in a ‘sulfate series’. Both series display an intersection at the point where the isobutane formation rate reaches its maximum (Fig. 8.1).

## 8.1. Results and discussion

Thulium-promoted samples of thulium contents between 0 – 5 mol%, as well as samples with a constant Tm content of 2 mol% and various sulfate contents (6 – 14 wt%) (Fig. 8.1), were successfully co-precipitated in an automated laboratory reactor system (*Mettler-Toledo Labmax*) at constant pH 9, sulfated through incipient wetness impregnation and calcined at 625 °C (Sect. 3.1). For the sake of comparability, all samples, promoted and unpromoted, were calcined at the same temperature. The samples in this chapter are indexed as follows: a sample with 2 mol% thulium and 10 wt% sulfate is indicated as 2TmSZ in the case of the variation of the Tm content or in the case of the variation of the sulfate content at a constant Tm content of 2 mol% the same sample is indexed more precisely as 2Tm10SZ, a sample containing 2 mol% thulium and 14 wt% sulfate is indicated as 2Tm14SZ.

Preliminary TEM investigations suggested that different parameters were crucial during the preparation of the catalyst. In order to avoid particles from connecting with each other and thereby creating structures of undefined size – which would make the material useless for defect analysis – the following parameters had to be optimized: the temperature during co-precipitation, the number of washing procedures as well as the solvents applied during this procedure, the time to homogenize the

amorphous precursor before, during and after incipient wetness sulfation, as well as the calcination temperature. Details of the optimized parameters can be found in Section 3.1. Tm-promoted SZ (TmSZ) samples calcined at 600 °C showed a significant amount of amorphous phase, whereas TmSZ samples calcined at 650 °C showed a clearly visible amount of monoclinic phase under the HRTEM. Therefore, 625 °C was chosen as calcination temperature where SZ was 100% tetragonal. Since oleum improves the catalytic performance of *n*-butane isomerization (Chap. 7), all samples were treated with SO<sub>3</sub> from the beginning of calcination until the end of the process. This oleum treatment reduced the effect of SO<sub>3</sub> release on the catalyst surface during calcination and made it possible to calcine unpromoted tetragonal SZ at 625 °C.

In the following, it will be shown that the bulk properties modifies the catalyst surface and therewith the catalytic performance in *n*-butane isomerization of the investigated thulium promoted SZ catalysts.

### 8.1.1. *n*-Butane isomerization

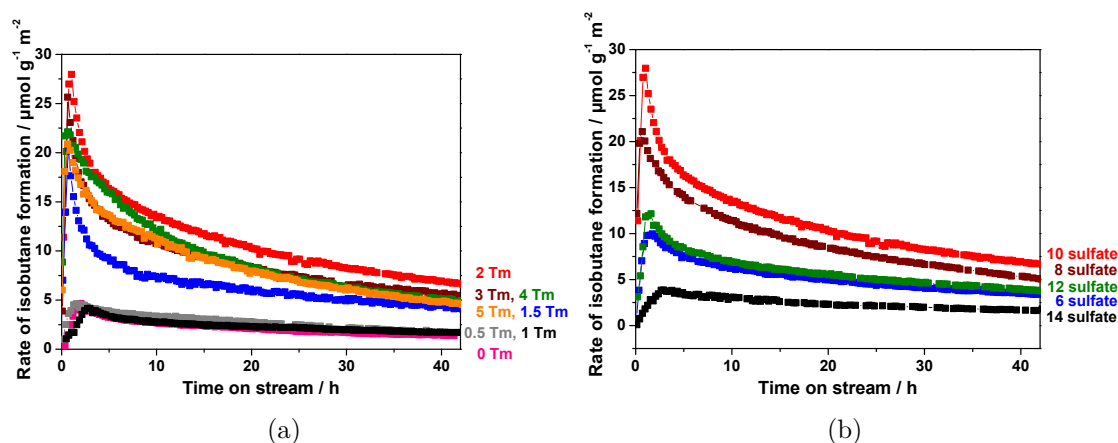


**Figure 8.2.:** *n*-butane isomerization for (a) the Tm series (varying thulium contents at 10 wt% sulfate) and (b) the sulfate series (varying sulfate loadings at 2 mol% TmSZ)

Fig. 8.2 demonstrates *n*-butane isomerization versus the Tm-content at a constant sulfate loading of 10 wt% (a) and versus the sulfate content at a constant Tm loading of 2 mol% (b). When the rate of isobutane formation after 40 hour on stream was

## 8. Effect of promoters and sulfate content on catalytic performance

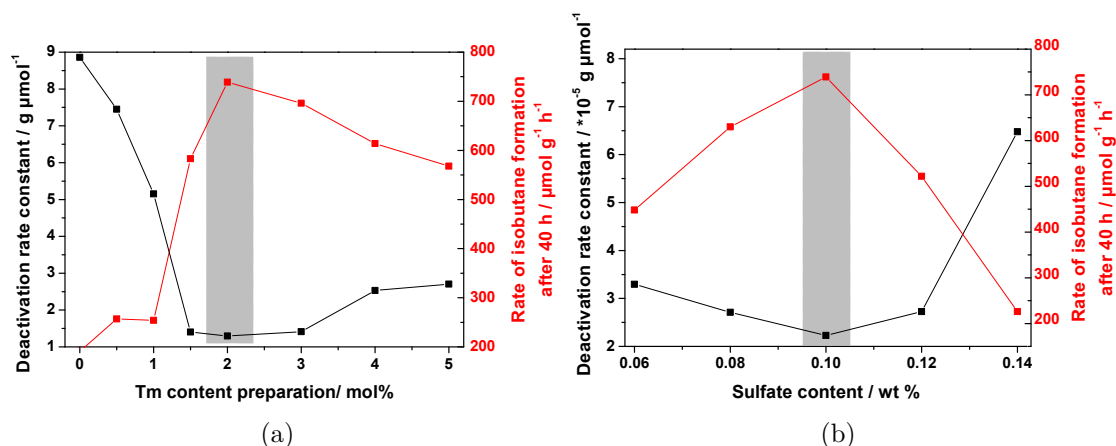


**Figure 8.3.:** Deactivation rate constants and rates of isobutane formation after 40 h on stream for samples with (a) varied thulium contents (mol%) at 10 wt% sulfate (Tm series), (b) varied sulfate loadings (wt%) at 2 mol% TmSZ (sulfate series), the best catalyst is highlighted with a grey background.

plotted as a function of sulfate or thulium content (Fig. 8.3), volcano-type curves were obtained, with an intersection for the sample containing 2 mol% Tm and 10 wt% sulfate. This sample is characterized by the highest *n*-butane isomerization rate after 40 h on stream ( $739 \mu\text{mol g}^{-1} \text{h}^{-1}$ ) and the lowest deactivation rate constant ( $2.2 \mu\text{mol g}$ ).

Generally, the trends of the Tm series (Fig. 8.3) given by the long term deactivation rate constant and the rate of isobutane formation pointing in opposite directions differ in their trends for samples with Tm contents between 1 and 3 mol%, of which the samples with Tm contents between 1.5 and 3 mol% show the lowest long term deactivation rate constants. An abrupt rise of the rate of isobutane formation is visible between 1 and 1.5 mol% Tm with a jump from  $254$  to  $583 \mu\text{mol g}^{-1} \text{h}^{-1}$  after 40 h on stream, which is also displayed in the decrease of the deactivation rate constant from  $5.2$  to  $2.3 \mu\text{mol}^{-1}$ . The 1.5TmSZ sample differs from the 2TmSZ sample – the latter having the highest catalytic performance and lowest deactivation rate constant – insofar the rate of isobutane formation further increases, while the value for the deactivation rate constant remains at its old level. The samples promoted with 3, 4 and 5 mol% thulium show only slight decreases in long-term activity, while the deactivation rate constants slightly increase for the 4TmSZ and 5TmSZ samples.



A different picture, however, evolves from catalytic tests with varied sulfate contents at a constant, optimized Tm content of 2 mol%, as shown in Figure 8.3b. For an increasing sulfate content from 6 to 10 wt% – optimum and intersection of the two series– the long term isomerization rate increases (from 448 to 739  $\mu\text{mol g}^{-1}\text{h}^{-1}$ ), while the deactivation rate constant decreases (from 3.3 to 2.2  $\text{g } \mu\text{mol}^{-1}$ ). After the point of optimum sulfate content has been reached, the rate is severely reduced to only 226  $\mu\text{mol g}^{-1}\text{h}^{-1}$  after 40 hour for the sample impregnated with 14 % sulfate (2Tm14SZ). This reduction is accompanied by a high deactivation rate constant of 6.5  $\text{g } \mu\text{mol}^{-1}$ . Later in the IR section it will be explained that this reduction of catalytic performance for the 2Tm12SZ and 2Tm14SZ samples cannot be easily explained by surface overloading. This would imply that the 2Tm10SZ sample represents a monolayer of sulfate on the surface, which is not the case. It is more likely that the surface sulfate structures are changes into less favourable configurations.

### 8.1.2. Nitrogen adsorption isotherm

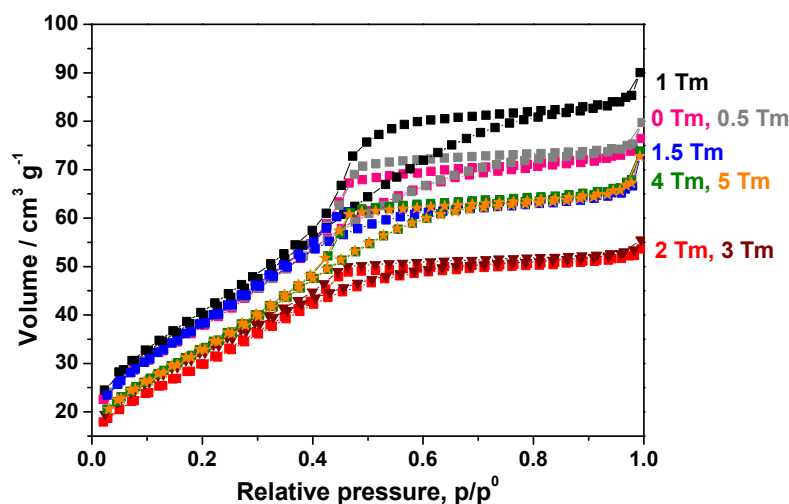


**Figure 8.4.:** Nitrogen adsorption isotherms of the Tm series (10 wt% sulfate samples with different thulium contents) indicating mesoporous materials.

According to IUPAC (Sect. 2.1), the isotherms of all investigated samples are type IV isotherms (Figs. 8.4 and 8.5). This type is characteristic for mesoporous solids consisting of particles crossed by nearly cylindrical channels or being formed

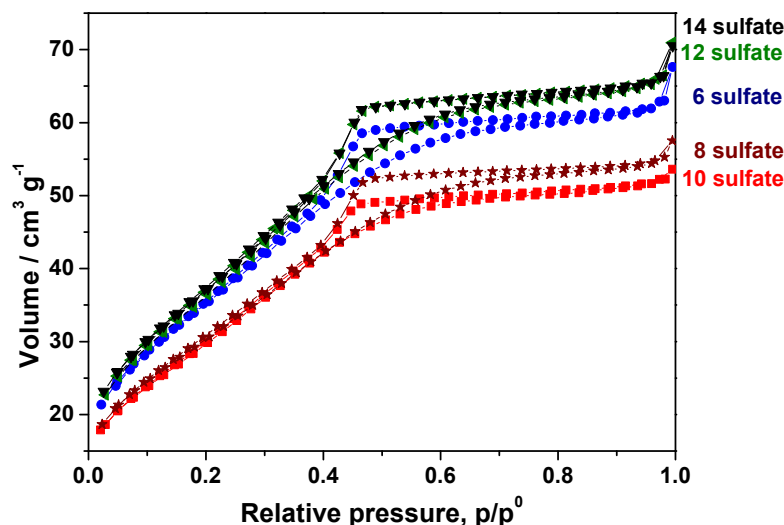


**Figure 8.5.:** Nitrogen adsorption isotherms of the sulfate series (2 mol% TmSZ samples with different sulfate loadings indicating mesoporous materials)

by aggregates (consolidated) or agglomerates (unconsolidated) of spherical particles. In the present case, the pores have heterogeneous sizes hysteresis (type H2) (see also Fig. 8.8). In the very low pressure region, the curves of the 0, 0.5, 1, and 1.5 mol% thulium overlap just as the 2, 3, 4, and 5 mol% samples do. This behavior fit together with an abrupt rise of the catalytic activity between the 1TmSZ and 2TmSZ sample (Fig. 8.2). Interestingly, the catalysts differ more in the high pressure region (total pore volume), than in the low pressure region, which displays the BET surface area (discussed later together with the lattice constants). Changes in both regions are coupled with changes in catalytic performance. The hysteresis loops of the 1.5, 2, and 3 mol% samples, the sample with lowest deactivation rate constant, are more narrow, and the 2TmSZ and 3TmSZ samples overlap. For further increase of thulium the hysteresis are reopened being positioned at higher volumes. The changes of the hysteresis loop are reflected in changes of the total pore volume (Fig. 8.6(a)) and changes of the pore size distribution (Fig. 8.8 (a)).

The sulfate series shows the same trends for the low pressure region, the hysteresis loops, and the high pressure region as the Tm series for changing *n*-butane isomerization rates. Between 6 and 10 wt% sulfate, the opening of the hysteresis loops decreases and yields lower volumes of adsorbed N<sub>2</sub> on the high pressure plateau. For the 12 and 14 wt% sulfate samples a higher volume of N<sub>2</sub> is adsorbed and has

more narrow hysteresis loops. Furthermore, there seems to be a trend for catalytic highly active materials (8, 10 wt%) to obtain lower values of adsorbed  $N_2$  to obtain lower values in the low pressure region, while catalysts with a low performance yield higher values. Similarly to the Tm series, changes in the high pressure region of the isotherms and of the hysteresis loops, are reflected in changes of the total pore volume, which are visualized in Figure 8.6(b) as well as changes of the pore size distribution in Figure 8.8(b).

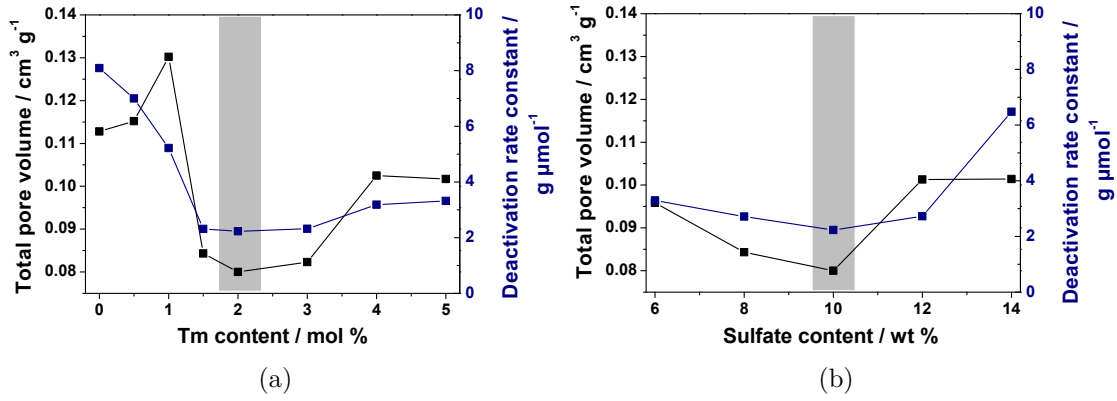


**Figure 8.6.:** Total pore volumes and deactivation rate constants for (a) the Tm series (10 wt% sulfate and varying thulium contents), (b) the sulfate series (2 mol% TmSZ samples with varying sulfate loadings)

Total pore volume and long term deactivation rate constant, shown in Figure 8.6, have a similar progression for increasing thulium and sulfate contents. In Figure 8.7(a) the total pore volume is plotted versus the long term deactivation rate constant for the individual thulium contents. A linear correlation with a  $R^2 = 0.979$  is shown in Figure 8.7(b) for thulium contents  $\geq 1$  mol%.

Figure 8.8 shows a bimodal distribution of pore volumes for all thulium containing samples with a first maximum around 25 Å and a second around 35 Å. The smaller pores are characterized by a broad pore size distribution between 10 and 40 Å on which a narrower one is superimposed between 30 and 40 Å. For 0TmSZ the smaller pore size range is subdivided into several local maxima. Obviously, the investigated samples of the thulium and sulfate series differ in the heights of the second maximum between 30 and 40 Å. Differences in the total pore volume of the individual samples, as well as its correlation with the long term deactivation rate constant, derive from varying abundance of large pores with a diameter between

## 8. Effect of promoters and sulfate content on catalytic performance

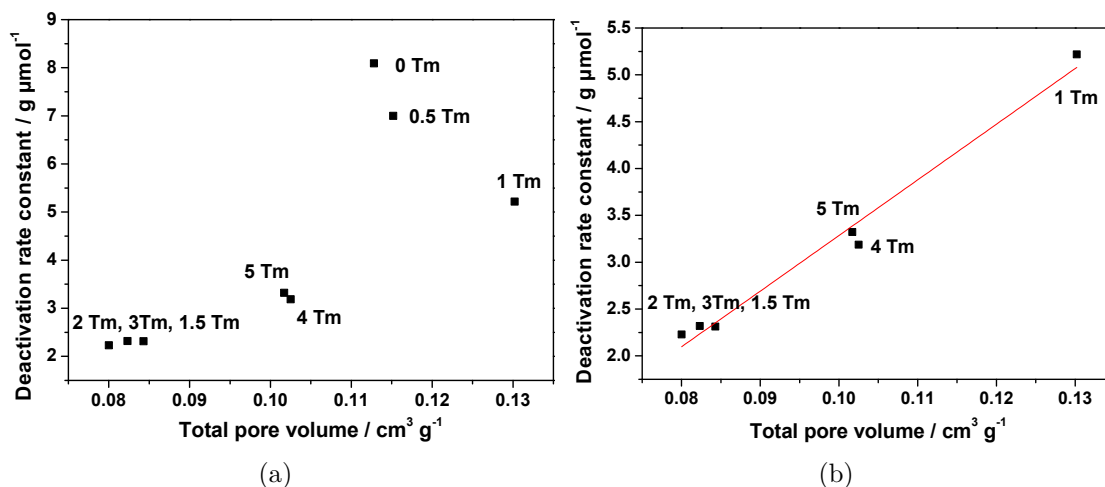


**Figure 8.7.:** Deactivation rate constant versus total pore volume for (a) for the complete Tm series, (b) for Tm contents between 1-5 mol%

30 and 40 Å. A possible explanation for this phenomenon could be polymerization inside the big pores leading to coke formation. This hypothesis is supported by the observation that the most stable catalysts (2Tm10SZ, 3Tm10SZ, 2Tm8SZ) show the lowest degree of blackening after 45 h *n*-butane isomerization and, in comparison, only relatively small quantities of these pores.

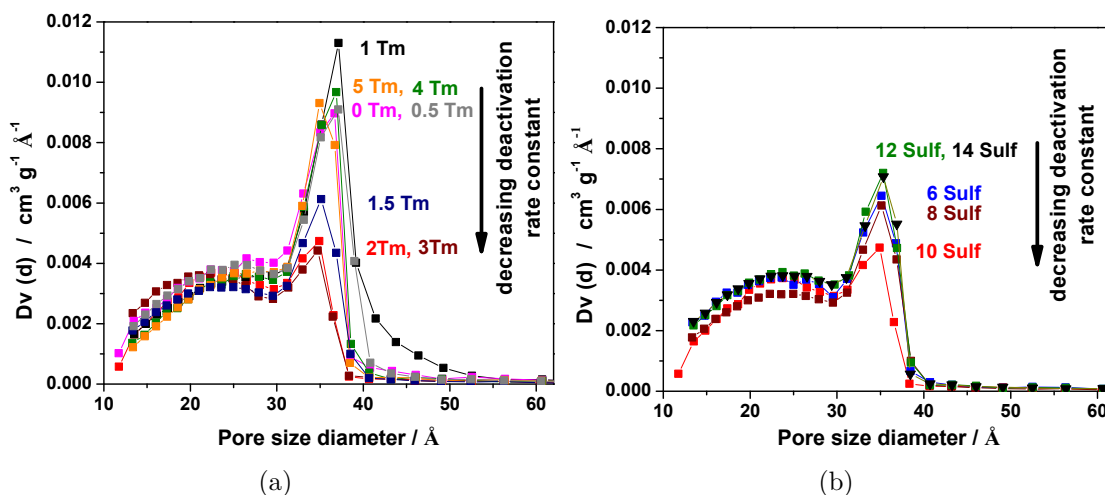


**Figure 8.8.:** Bimodal pore size distribution for (a) the Tm series (varying thulium contents at 10 wt% sulfate) and (b) the sulfate series (varying sulfate loadings at 2 mol% Tm)

## 8.1.3. SEM

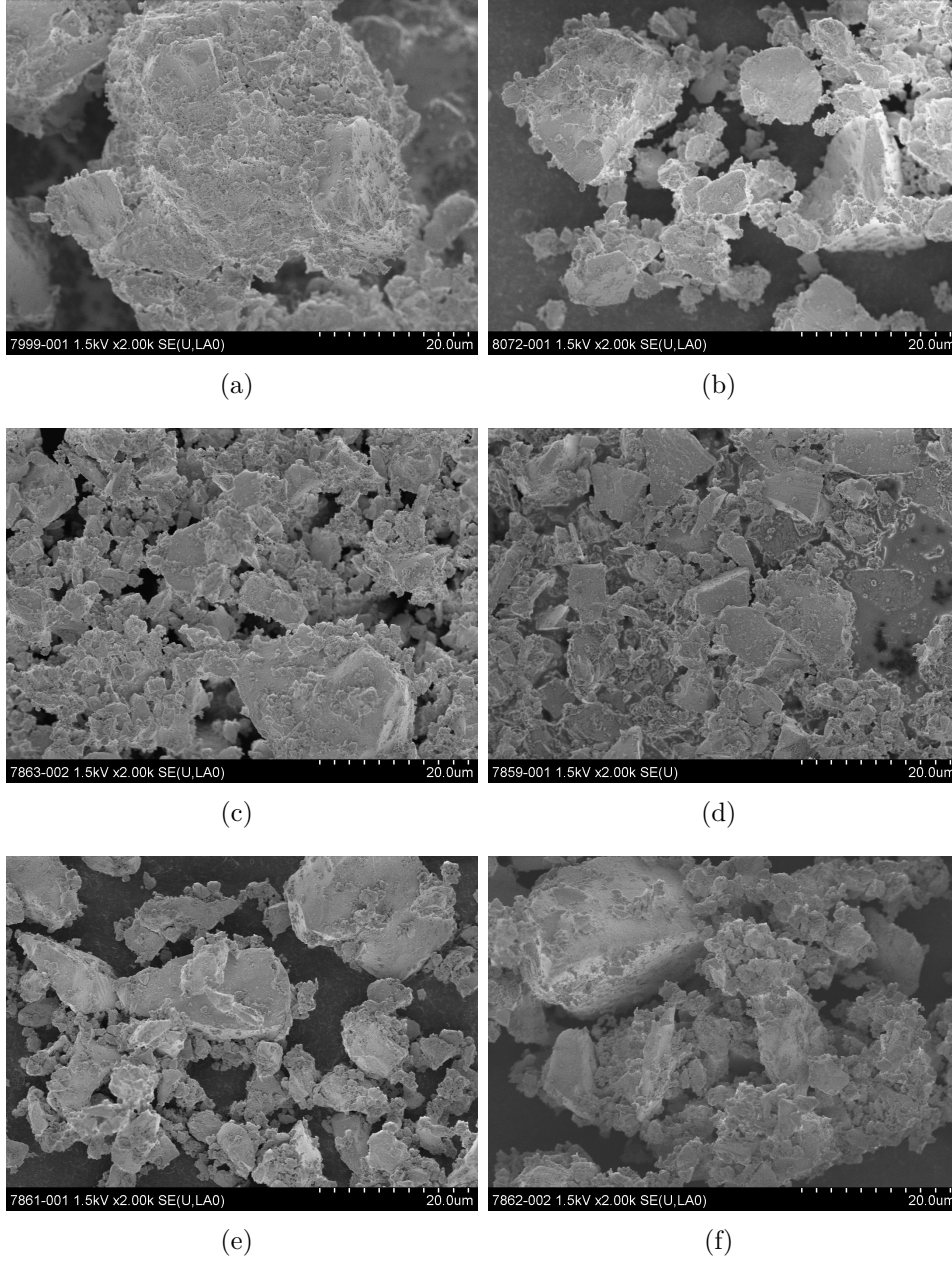


**Figure 8.9.:** SEM images of the Tm series (10wt% sulfate) (a) 0TmSZ, (b) 1TmSZ, (c) 1.5TmSZ, (d) 2TmSZ, (e) 4TmSZ, (f) 5TmSZ

The SEM images in Figures 8.9 and 8.10 demonstrate that the distribution of particle agglomerates (secondary particles) is most homogeneous for the sample

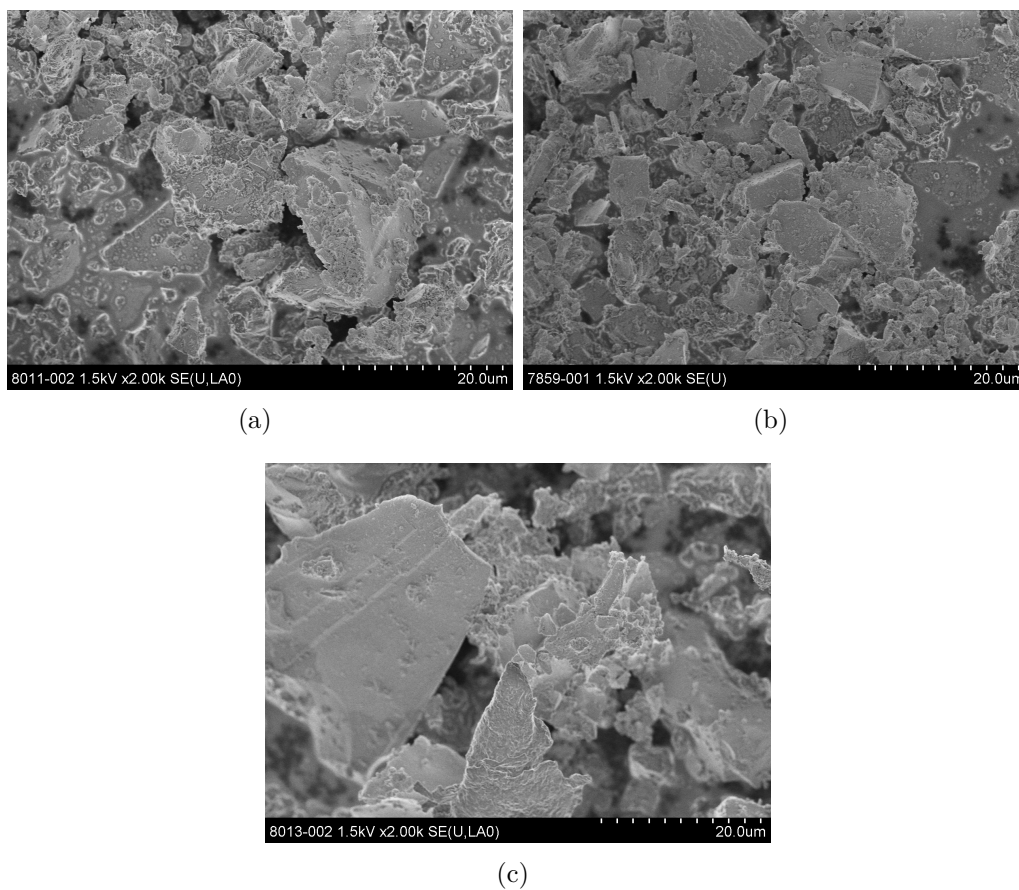


**Figure 8.10.:** SEM image of the sulfate series (all samples contain 2 mol%Tm)  
(a) 6wt% sulfate, (b) 10wt% sulfate, (c) 14wt% sulfate

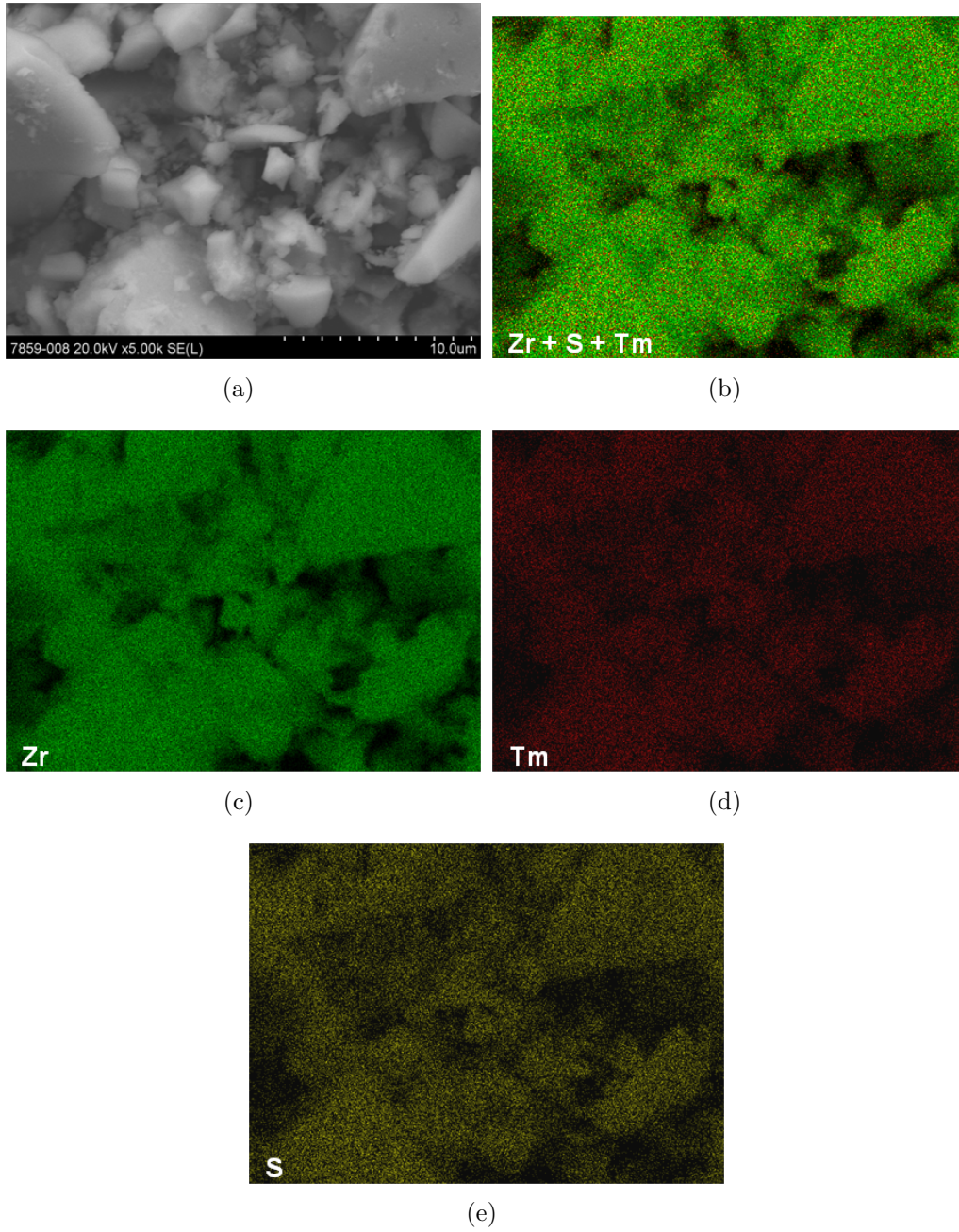


**Figure 8.11.:** Element mapping of 2TmSZ (a) overview, (b) Zr, Tm and S, (c) Zr, (d) Tm, (e) S shows a homogeneous distribution of the displayed elements.



with the highest catalytic performance. Furthermore, the secondary particles of this sample are most well-separated from each other. The more the thulium and sulfate values deviate from the optimum values (2Tm10SZ) the less separated are the individual particles. The energy dispersive X-ray spectroscopy (EDX) element mapping (Fig. 8.11) shows that zirconium, thulium and sulfur are well distributed over the secondary particles. This is valid for all samples and means that, besides (thulium promoted) sulfated zirconia, no other phase can be detected by this method.

### 8.1.4. XRD analysis

Lattice constants and unit cell volume were determined by Rietveld refinement with the program *TOPAS*. The peak shape analysis of a single peak was performed by a pseudo Voigt fit of the (101) XRD peak to apply Warren's theory (see Sect. 2.2).

#### BET-surface area and unit cell volume

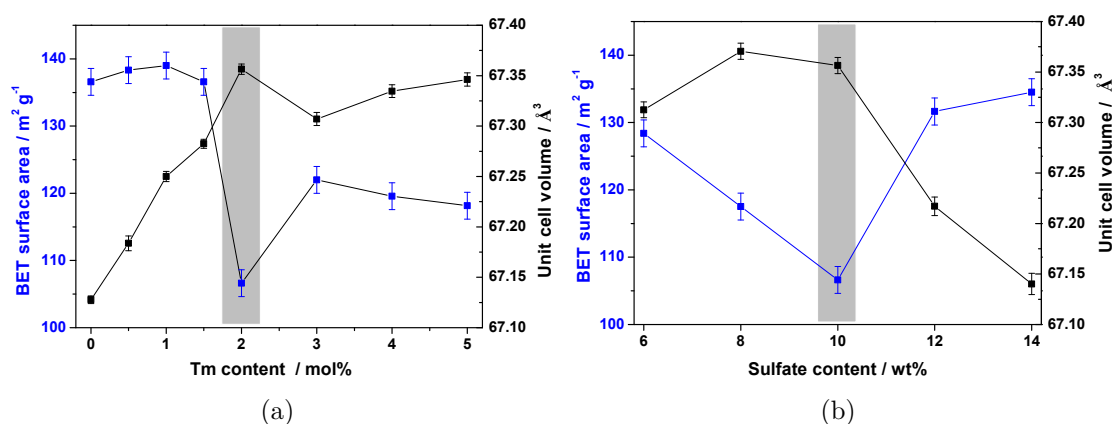


**Figure 8.12.:** BET surface area and unit cell volume for (a) the Tm series, (b) the sulfate series, the best catalyst is highlighted with a grey background.

Generally, the BET surface area decreases for increasing Tm contents from 137 to 118 m<sup>2</sup>/g, with a minimum (Fig. 8.12 (a)) for the 2 mol% Tm sample (the one with the best catalytic performance) of 107 m<sup>2</sup>/g. At the same time, the unit cell volume increases from 67.128 Å to 67.346 Å, with a maximum of 67.356 Å for the 2 mol% Tm sample. The same goes for the lattice parameter *a* (not shown here). The decrease



in the surface area is first visible for the sample promoted with 1.5 mol% thulium, for smaller Tm contents the surface area remains almost constant.

Figure 8.12 (a) shows that the trendlines of the BET surface area and of the lattice volume overlap in the 2Tm10SZ sample, which is far from both trendlines in its characteristics. For 0 – 2 mol% thulium the unit cell volume increases from 67.13 – 67.36 Å. Beyond 2 mol% Tm the values scatter around a possible plateau on the level of the 2 mol% Tm.

In the sulfate series, the BET surface area decreases for the 6 to 10 wt% sulfate samples from 128 to 107 m<sup>2</sup>/g and re-increases for higher sulfate values up to 134 m<sup>2</sup>/g for 14 wt% sulfate, as demonstrated in Figure 8.12 (b). The unit cell volumes show a mirrored trend compared to the surface area (Fig. 8.12(b)), starting with a unit cell volume of 67.313 Å increasing a maximum for the 8 and 10 wt% samples (67.371 and 67.356 Å) that are followed by decreasing values (67.140 Å for 14 wt% sulfate).

It is interesting to note that the catalyst with the highest catalytic performance (2Tm10SZ) has the lowest BET surface area. This means that the catalytic performance of the catalyst is a result of its intrinsic properties and not of its surface area. Furthermore, it is surprising that the lattice parameter  $a$  and the unit cell volume systematically change for increasing sulfate contents. The literature generally suggests that the sulfate is located on the surface and not in the bulk and that, therefore, it should not affect structural parameters like the lattice constant  $a$  and the unit cell volume. The present results suggest that sulfate is incorporated into the zirconia bulk structure in some way or affects the incorporation of thulium. The maximum in the unit cell volume for the 8 and 10 wt% samples in the sulfate series, as well as the changes in the unit cell volumes above 2 mol% Tm cannot be easily explained. It is possible that thulium interacts with sulfate in the crystalline lattice. Since sulfate is relatively large, it could only be accumulated in linear defects like dislocation lines or three-dimensional defects.

For the catalysts of both series, the surface area shows a connection to the lattice constant  $a$  and the unit cell volume, indicating that the surface area depends on structural properties. The general trendline of increasing lattice constants for increasing Tm content can be explained with the bigger ionic radius of thulium compared to zirconium, with 0.994 nm for Tm<sup>3+</sup> compared to 0.84 nm for Zr<sup>4+</sup>, both compared in eightfold coordination [113].

It is noteworthy that SZ and TmSZ nanoparticles synthesized by precipitation/co-precipitation are not single isolated particles. HRTEM images illustrate the existence of cohesion between the nanocrystallites within the agglomerates. Similar behavior was found by Rezaei et al. [114] for pure unsulfated tetragonal zirconia. The authors calculated the change of the monoclinic-to-tetragonal phase transformation at room temperature as a result of the modified surface free energy values when single, isolated zirconia nanocrystallites become elements of an aggregated particle. It appeared that the critical crystalline size for phase transformation increased from 9.6 to 33.2 nm. These findings could explain why the co-precipitated TmSZ and precipitated SZ samples are 100 % tetragonal in contrast to the samples drawn from consisting of industrial starting material (*MelChem*), which contain about 3 % monoclinic phase.

### XRD peak shape

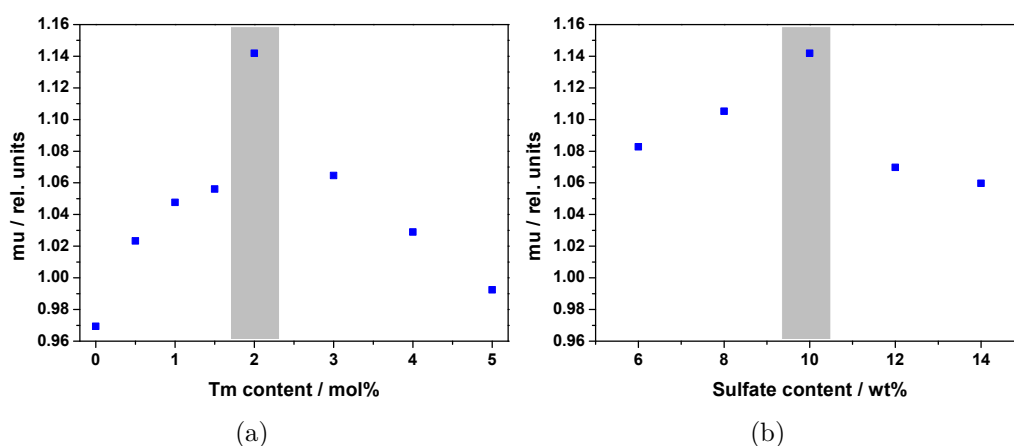


**Figure 8.13.:** The mixing parameter  $\mu$  of (a) Tm series, (b) sulfate series reflects the trend of the catalytic performance for increasing thulium and sulfate contents. Values above unity indicate superlorenzian peak shapes.

As explained in section 2.2.3, the XRD peak shape of the (101) peak of tetragonal zirconia is used to determine a mean XRD domain size in order to be able to compare this size with a mean value of the real particle size derived from TEM investigations. Both values are used to calculate the relative apparent defect density.

The mixing parameter ( $\mu$ ) of the pseudo Voigt fit of the (101) XRD peak reflects the peak shape. Furthermore, Figure 8.13 shows that it reflects the trend of the

catalytic performance for increasing thulium and sulfate contents with a maximum value for the 2 mol% catalyst impregnated with 10 wt% sulfate. In Figure 8.13, values above unity indicate super-Lorentzian peak shape for Tm contents between 0.5 and 4 mol% Tm as well as for all varied sulfate contents. Super-Lorentzian peak shape indicates a broad range of particle sizes with a high proportion of small particles. Unfortunately, the values above unity have no physical meaning for the model used to determine the particle size. For the calculation of the apparent defect density the mixing parameter ( $\mu$ ) of the (101) XRD peak and the full width at half maximum (Fig. 8.14) were used to determine the XRD domain size. In general, for this peak analysis peaks with a mixing parameter  $\mu$  between 0 and 1 are needed, in other words, a peak shape between Gaussian and Lorentzian. As the observed values for  $\mu$  differ just slightly from unity, the trend can be used for a calculation. The most active catalyst has a maximum in  $\mu$  of 1.14 (relative units), indicating a maximum of small particles (tails of the peak) and a large mean size (peak maximum).

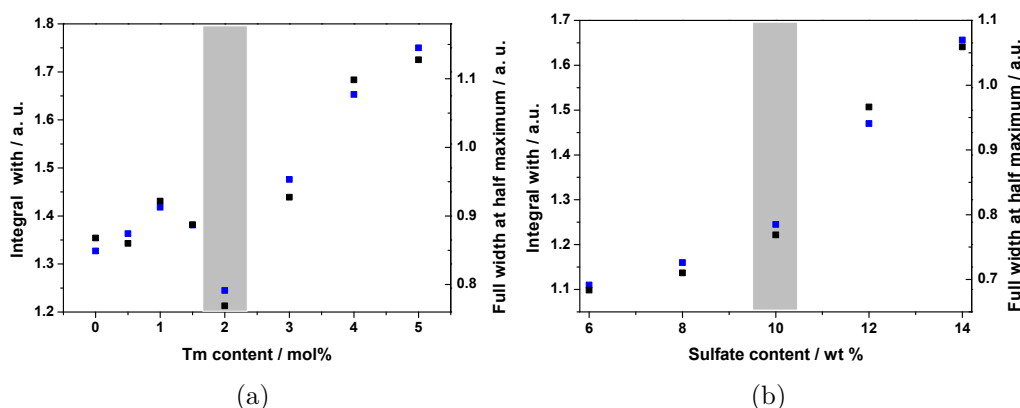


**Figure 8.14.:** Full width at half maximum and integral width show similar results for the individual catalysts. Both peak shape parameters are displayed for the (a) Tm series, (b) sulfate series.

The full width at half maximum and the integral width (Fig. 8.14 (a)) for increasing Tm contents show an increasing tendency with obvious deviations to lower values for the 2TmSZ catalyst and slighter ones for samples with a Tm content close to that one of the best catalyst (1.5TmSZ and 3TmSZ). Figure 8.14 (b) shows that both the full width at half maximum and the integral width (Fig. 8.14 (b)) increase for sulfate contents between 6 and 14 wt%.

### 8.1.5. TEM particle size determination

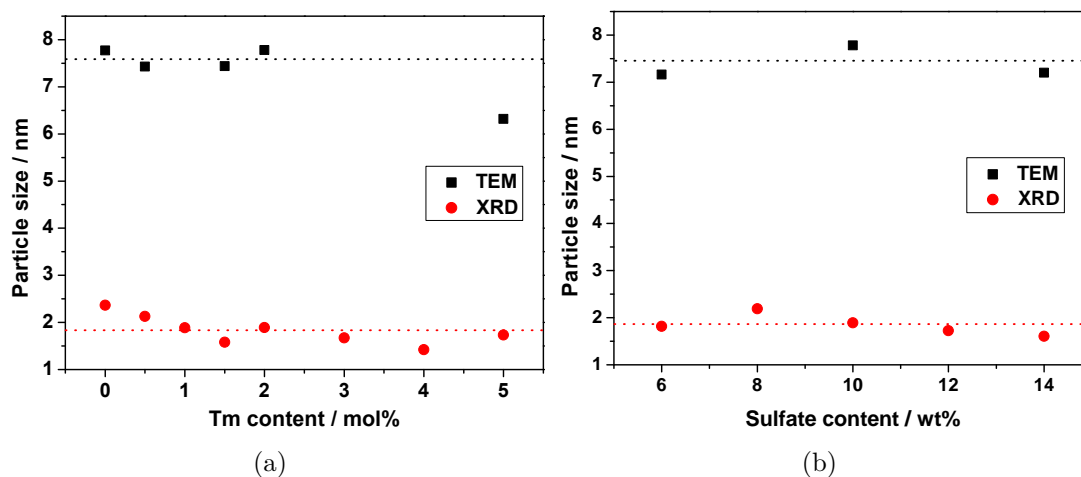
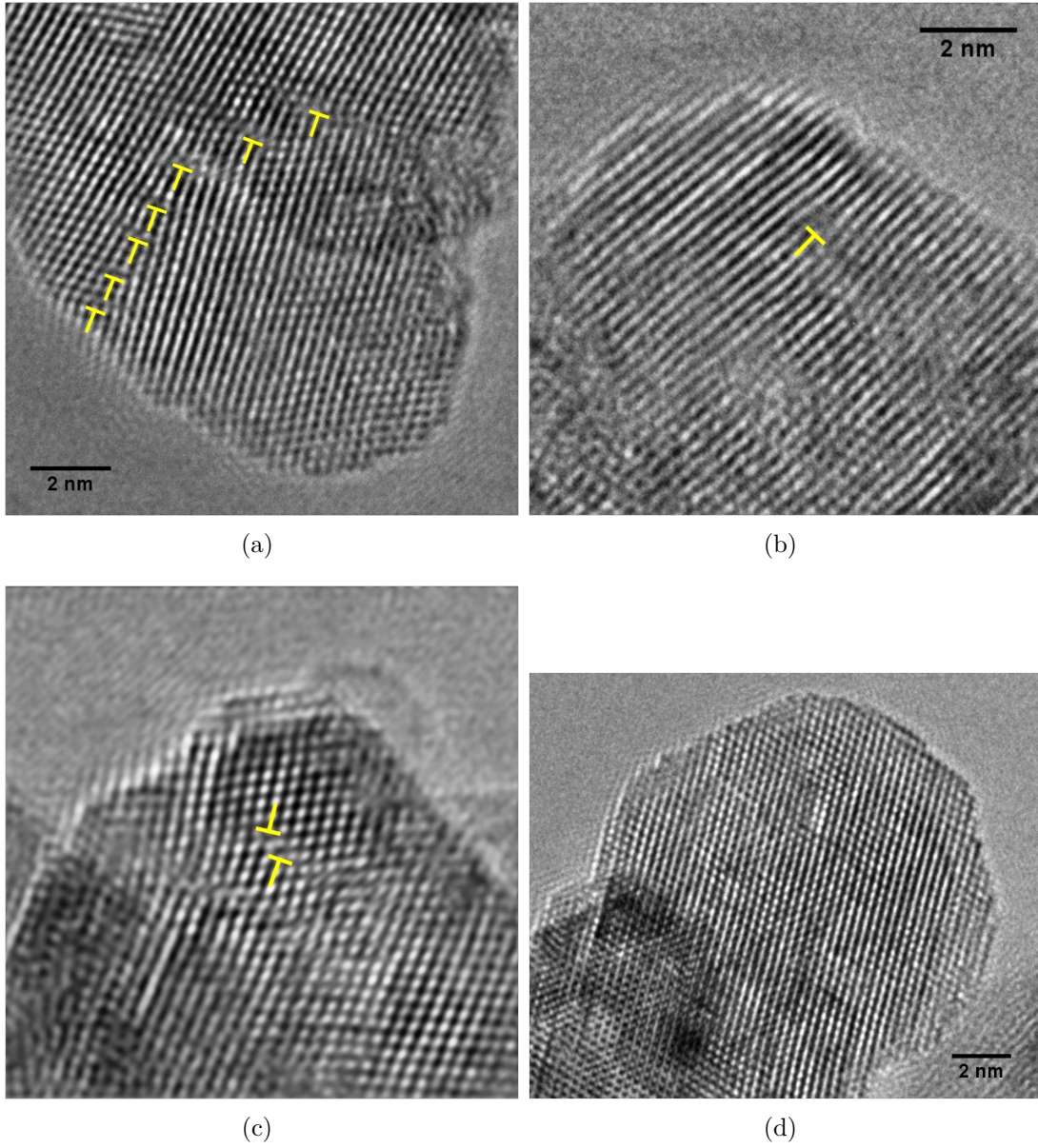


**Figure 8.15.:** Comparison of particle sizes derived from TEM and XRD for the (a) Tm series, (b) sulfate series. Particle sizes are constant in both series.

The real particle size given by TEM images, is determined by measuring the diameter of more than 2000 particles. The results of determination are shown in Figure 8.15 for both series. Particle sizes obviously did not change significantly. The maximum particle size of 7.78 nm was found for the 2 mol% catalyst impregnated with 10 wt% sulfate. A similar value was found for the unpromoted catalyst. With a value of 6.32 nm, the 5 mol% thulium sample was found to have the smallest averaged particle size. XRD domain size, determined by pseudo voigt fitting, lies between 1.42 nm for the unpromoted catalyst and 2.37 nm for the 4 mol% catalyst. The variation in the particle size obtained by TEM and XRD are smaller for the sulfate series (Fig. 8.15(b)) than for the Tm series (Fig. 8.15 (a)).

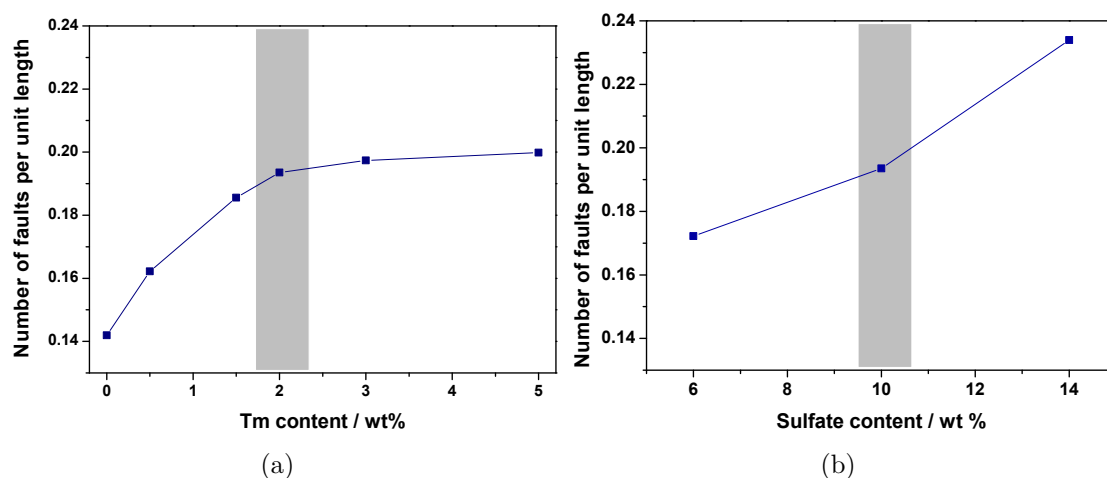
#### Apparent faulting probability

Figure 8.16 shows HRTEM images of the 2Tm10SZ sample. Different kind of crystal imperfections are displayed. Beside point defects – visible as spotty contrasts – dislocations are imaged. They induce small angle boundaries and local strain fields around their core. These dislocations, which produce a mosaic-like structure of separated domains, are the visible basis for determination of apparent faulting probabilities – a measure for the defect density.



**Figure 8.16.:** HRTEM images of the 2Tm10SZ sample displaying different types of crystal lattice imperfections (a) dislocation array (small angle boundary;  $\alpha = 14^\circ$ ) separating two crystallites. (b) A single edge dislocation produces visible lattice distortions (strain field) around its core. (c) Unidentified defect (possibly, two edge dislocations of opposite sign close together). Note the lattice rotation by about  $10^\circ$ . (d) Spotty contrast indicates presence of lattice distortions.

These are determined by using the values of the XRD peak shape analysis (Sect. 8.1.4) and the values for the real particle sizes derived from TEM investigations

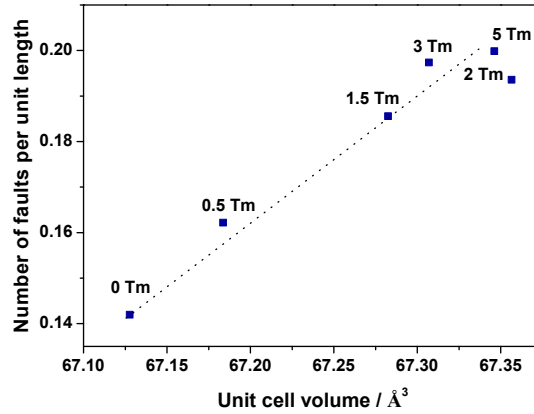


**Figure 8.17.:** The apparent faulting probability for the (a) Tm series, (b) sulfate series was calculated by combining XRD and TEM data and applying the Warren theory. The best catalyst is highlighted with a grey background.

(Sect. 8.1.5) and applying them to the Warren theory (Sect. 2.2.3). Figure 8.17 (a) shows an increase of the apparent faulting probability for Tm contents under 2 mol%; for higher thulium contents a plateau is reached. Consequently, the value for the 2 mol% sample marks the threshold beyond which the catalytic performance cannot be improved by a further increase of Tm. The catalyst marking this threshold, can be said to display the best catalytic performance and long term stability. This fact leads to the idea that 2 mol% Tm is the maximum concentration of Tm that can be incorporated into the lattice. For increasing contents of  $\text{Tm}^{3+}$  substituting  $\text{Zr}^{4+}$ , this trend can be explained by an increasing amount of oxygen defects, maintaining lattice neutrality in the zirconia lattice. Above 2 mol% Tm, Tm possibly forms  $\text{Tm}_x\text{S}_y\text{O}_z$  phases. These phases are known for different stoichiometries ( $\text{Tm}_2\text{O}_3$  ICSD-400048 [115],  $\text{Tm}_2\text{S}_2\text{O}$  ICSD-67380 [116]) but their small amounts are undetectable for XRD and EDX. Energetically the formation of  $\text{Tm}_x\text{S}_y\text{O}_z$  phases seems to be more favorable than the formation of solid solutions above 2 mol% Tm in this system. Whereas for cubic zirconia complete solid solution between zirconia and thulium as well as for all other investigated rare earth elements (Th, Nd, Sm, Eu, Gd, Tb, Dy, Y, Ho, Er, Yb, Lu, and Sc) is reported by Yashima et al. [111].

Figure 8.17 (b) demonstrates an almost linear increase in apparent faulting probability for increasing sulfate concentration during preparation, reflecting an

influence of sulfur in the catalyst bulk as has already been suggested for the relation between BET surface area and unit cell volume shown in Figure 8.12.



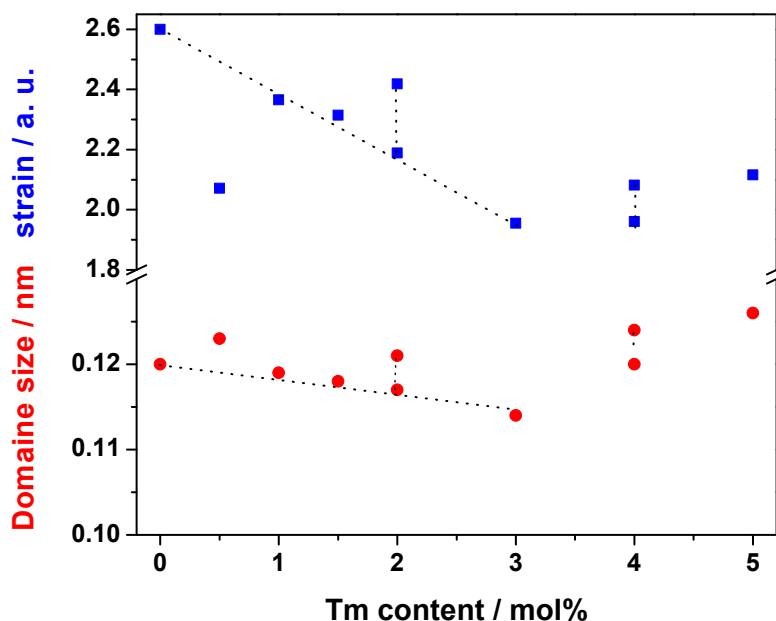
**Figure 8.18.:** Correlation between apparent faulting probability and unit cell volume

Figure 8.18 shows a linear correlation between the apparent faulting probability and the unit cell volume within the Tm series. This proves that the increase of the unit cell volume for increasing thulium contents arises from the increasing faulting probability caused by thulium incorporated into the zirconia lattice. Furthermore, it shows the applicability of the Warren's theory for tetragonal sulfated zirconia and of the XRD single peak fitting. While the unit cell volume was determined by a Rietveld full pattern refinement the XRD domain size was determined by a single peak fitting of the (101) peak, which was used to be able to use the Warren theory for planar defects.

### Variance method

There is no theoretical model which directly uses the super-Lorentzian peak shape in order to calculate defect densities. We could have made use of a number of methods that work with raw data without fitting, but the data quality of the present study is insufficient because of a high noise level due to small crystallite sizes. Therefore, the shape of the most intense peak, the (101) peak, had to be smoothed, and we needed a model for a single peak fit for the super-Lorentzian peak shape. First of all, the peak was fitted with a model based on calculations from first principles which





**Figure 8.19.:** Size and strain for increasing Tm content, calculated with the variance method by Igor Kasatkin. (Two points for the same Tm content mark different results of the first principles calculations, with equally good results for the fitted XRD diffractogram.)

was described elsewhere [6]. However, none of the functions that are typically used worked to describe this fitted peak shape, because the crystalline size distribution was not a log normal type as it is usually. The only reliable method that was able to derive a function adequately describing the presented peak shape is the variance (or dispersion) method. This method is reliable because it uses the whole peak profile. It was published for zirconia by Sánchez et al. in 2009 [95]. They suggested a new, generalized model to derive size and strain from peak broadening. Using this method, we calculated the dispersion from the center of the peak with increasing ranges to both sides. The peak shape was precisely fitted by using a polynomial. The residual between raw data and simulated peak shape was nearly zero, which proves that the fitted profile was smoothed without any noise. The smoothed function describing particle size distribution is at least bimodal for TmSZ catalysts. The challenge in the calculations was to find the correct background level, because even small changes in the level yielded different results. Therefore, the function was calculated for different background levels. Figure 8.19 shows size and (micro-)strain plotted versus Tm content. First principle calculations using



the variance method calculated by Igor Kasatkin. Strain decreases with increasing dopant between 0 and 3 mol% Tm. A minimum is visible for thulium contents between 2 and 3 mol% (both catalysts showing the best long term stability). For the 4 and 5 mol% Tm samples the strain remains constant or slightly increases. The only strain value which cannot be explained is the, in comparison, low strain value of the 0.5 mol% TmSZ sample. The domain size curve shows a similar less visible trend for increasing Tm content. Up to 3 mol% Tm the domain size remains almost constant and increases for the 4 and 5 mol% Tm samples. The fact that unpromoted SZ does contain visible strain – which is possibly induced by dislocations (which are visible under the TEM) – explains why the differences in strain can be calculated but are not visible when comparing a TEM images of the OTmSZ sample with one of the 2TmSZ sample. According to the model we used, the resulting polynomial suggests an inhomogeneous distribution of Tm as the main reason for strain. This inhomogeneous distribution of Tm is invisible in the EDX images (Fig. 8.11) because of the limited resolution of this method and because quantities are too low and the particle sizes are too small for this method. In promoted SZ, the larger Tm substitute Zr, thereby creating a local strain field and dislocations, which can be partially relaxed by forming dislocations. The influence of Tm on SZ is suggested to be due to Tm ions which diffuse to the dislocation lines and adhere to them (Fig. 8.20), resulting in Tm-decorated dislocation lines (Cottrell atmosphere) and a decrease in total non-uniform strain. Furthermore the dislocation lines are fixed by the phenomenon and the defect structure remains.

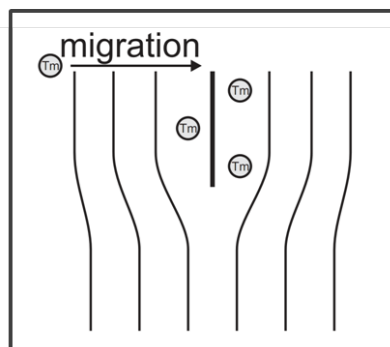


**Figure 8.20.:** Cottrell atmosphere model applied for Tm in tetragonal sulfated zirconia with Tm migrating to a dislocation line

## 8.1.6. Determination of the Lewis and Brønsted acid sites

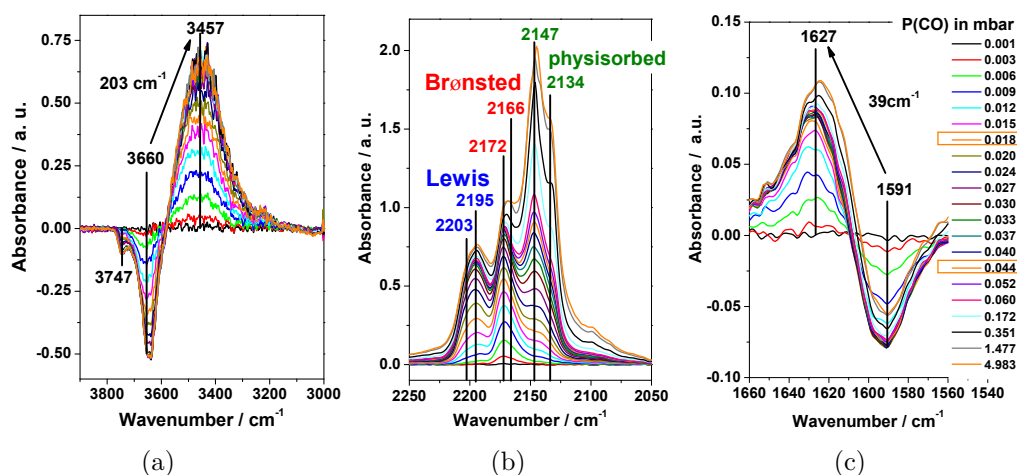


**Figure 8.21.:** IR difference spectra of CO adsorption on SZ at  $-196\text{ }^{\circ}\text{C}$  illustrating the relevant spectra ranges for the determination of Lewis and Brønsted acid sites (a) OH vibration region, full coverage of Brønsted sites at a CO partial pressure of 0.044 mbar, (b) carbonyl stretching vibrations, (c) coverage of  $\text{H}_2\text{O}$  influenced Brønsted sites,  $\delta_{(\text{H}_2\text{O}_{\text{ads}})}$  in  $\text{S}_2\text{O}_7^{2-} \cdot 2\text{H}_2\text{O}$  at a CO partial pressure of 0.018 mbar.

Lewis and Brønsted acid sites were determined for the Tm and sulfate series by CO adsorption and IR spectroscopy, as described in Section 2.6.1. Figure 8.21 shows three spectral ranges for the determination of Lewis and Brønsted acid sites of the 2TmSZ sample (comparably to Fig. 6.9). In contrast to Chapter 6, where only the relative L/B ratio was investigated in the pressure region of the  $\text{H}_2\text{O}$  influenced Brønsted sites, here the Lewis and Brønsted sites are analyzed in more detail in two relevant pressure regimes of CO partial pressure in order to obtain a deeper understanding and to calculate site concentrations for the Tm and sulfate series.

A shift in the OH-vibration region of  $203\text{ cm}^{-1}$  to smaller wavenumber position is attributed to acidic Brønsted sites (Fig. 8.21 (a)). Full coverage of Brønsted sites is reached at a CO partial pressure of 0.044 mbar. This is one of the two investigated pressure regions in this chapter. The other interesting pressure region can be determined by Figure 8.21 (c): A band shift of  $39\text{ cm}^{-1}$  to higher wavenumbers is attributed to  $\delta_{(\text{H}_2\text{O}_{\text{ads}})}$  in  $\text{S}_2\text{O}_7^{2-} \cdot 2\text{H}_2\text{O}$  [75], i.e.  $\text{H}_2\text{O}$  influenced Brønsted sites. For the 2TmSZ sample, this band is completely shifted at a CO partial pressure of 0.018 mbar. Figure 8.21 (b) shows the region of the carbonyl stretching vibrations,

in this range Lewis ( $2203\text{ cm}^{-1}$ ,  $2195\text{ cm}^{-1}$ ), Brønsted ( $2172\text{ cm}^{-1}$ ,  $2166\text{ cm}^{-1}$ ) as well as physisorbed CO bands ( $2147\text{ cm}^{-1}$ ,  $2134\text{ cm}^{-1}$ ) can be observed.

For the determination of the L/B ratio and site concentrations the peak areas of CO adsorbed on both Lewis and Brønsted acid sites were investigated in the carbonyl stretching vibrations region, as explained in Section 2.6.1, with CO pressures region of 0.015 mbar ( $\text{H}_2\text{O}$  influenced Brønsted sites) and 0.040 mbar (full coverage of Brønsted sites). Since the samples were investigated at the same coverage in these pressure regions – instead of measuring at the same CO partial pressures – the individual CO partial pressures deviated (Fig. 8.22 for the Tm series and Fig. A.5 for the sulfate series). For this purpose the shift positions of the individual samples were determined in the OH vibration region and the  $\text{H}_2\text{O}$  vibration region.

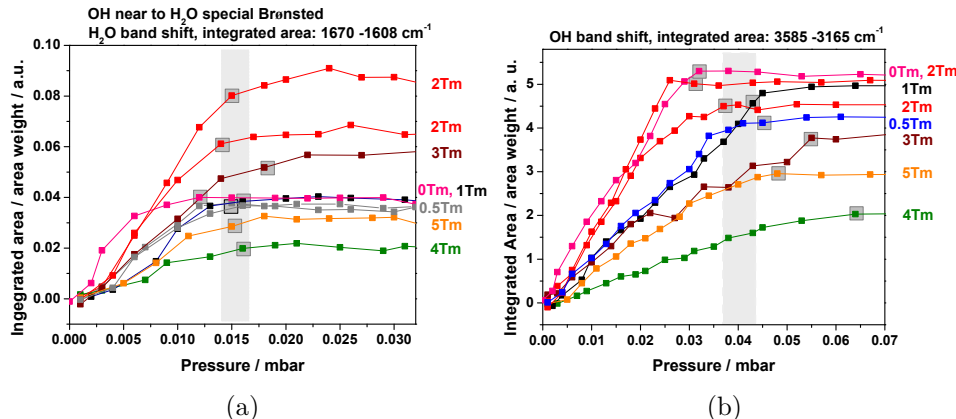


**Figure 8.22.:** Integrated peak areas for increasing pressure of CO adsorption on samples with varied Tm contents. Saturation of (a)  $\text{H}_2\text{O}$  influenced Brønsted sites at  $\approx 0.015$  mbar, (b) full coverage of Brønsted sites at  $\approx 0.04$  mbar illustrating the individual investigated pressures for the Tm series.

In order to be able to calculate concentrations of Lewis and Brønsted acid sites, an extinction coefficient ( $\epsilon_\nu$ ) was selected from literature. Morterra et al. [117] investigated CO adsorption on Lewis sites of  $\text{TiO}_2$  by IR spectroscopy with the help of a volumetric gas dosing system and microcalorimetry. They found that the extinction coefficient of adsorbed CO is almost constant for complexes whose frequency is in the range of  $2150 - 2190\text{ cm}^{-1}$  with an  $\epsilon_{2187} = 2.6 \pm 0.3\text{ cm}/\mu\text{mol}$ . Marchese et al. [118] quantified Brønsted sites in microporous catalysts by combined FTIR (CO and  $\text{NH}_3$  adsorption) and  $\text{NH}_3$ -TPD. They used an extinction coefficient

of  $\epsilon_{2187} = 2.5 \text{ cm}/\mu\text{mol}$  based on the findings of Morterra et al. and came to the conclusion that the overall concentration of Brønsted acid sites determined by the three different approaches were in good agreement. Therefore, this extinction coefficient of adsorbed CO was used in the present study for calculating the amount of Lewis and Brønsted sites.

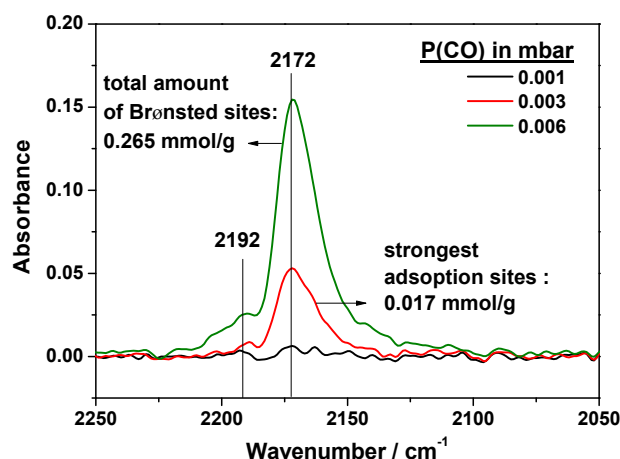


**Figure 8.23.:** CO adsorption on 2TmSZ. The ratio of 6.4 % between the strongest, firstly adsorbed Brønsted sites, and the total amount of these sites is in agreement with literature data and confirms the validity of the CO extinction coefficient.

With a rough calculation the validity of the used extinction coefficient was confirmed: For this purpose the ratios of the first adsorption sites, which are assumed to be the most acidic, and the total amount of Brønsted acid sites were taken for 0TmSZ and 2TmSZ (see Fig. 8.23 as example for 2TmSZ) and compared to literature data. The ratios for 0TmSZ and 2TmSZ are 4.4 and 6.4. This means that approximately 5 % of the Brønsted sites were covered before co coverage of Lewis sites is initiated for increasing CO partial pressure at  $-196^\circ\text{C}$ . This estimation is in good agreement with literature data: Breitung et al. [100] selectively poisoned 3 % of Brønsted centers close to sulfate groups which resulted in a significant decrease of isomerization activity. In the present study, the initial quantity of CO adsorbed on Brønsted acid sites is 0.013 mmol/g for 0TmSZ and 0.017 mmol/g for 2TmSZ, respectively. This fits well with the results presented by Wrabetz et al. [119] who identified a small group of sites (0.02 mmol/g) to be very acidic, yielding heats of 50-60 kJ/mol. Small deviations from the reported literature values can be explained

by the fact that the accuracy of the IR measurements was limited by the stepwidth of the CO dosing during its adsorption on the surface of SZ.

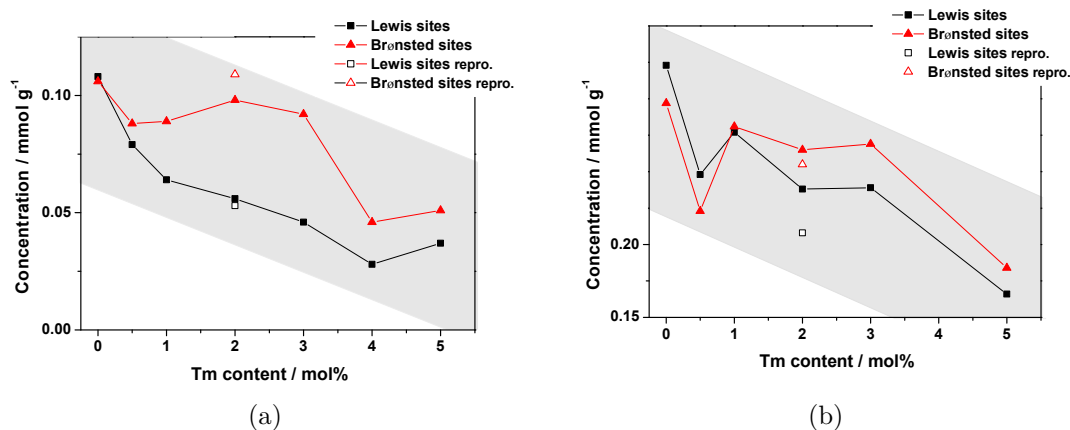


**Figure 8.24.:** Concentration of Lewis and Brønsted acids sites versus Tm content (a) for H<sub>2</sub>O influenced Brønsted sites, (b) full coverage of Brønsted sites illustrating a decreasing trend of both sites for increasing Tm contents. The peak areas of Lewis and Brønsted sites were fitted and the side concentrations were calculated by using an extinction coefficient of  $\epsilon_{2187} = 2.5 \text{ cm}/\mu\text{mol}$  selected from the literature

Figure 8.24 illustrates that the concentration of Lewis and Brønsted acids sites decreases for increasing Tm contents. The difference in the amount of Lewis and Brønsted acid sites is the greatest for the catalyst with the highest performance (2TmSZ), resulting in the lowest L/B ratio. The amount of water influenced Brønsted sites is roughly half of the total amount of Brønsted acid sites of, approximately 0.1 mmol/g. Furthermore, the trend is less resolved at full coverage of Brønsted sites. This demonstrates that water is part of the active site. When comparing the amount of surface acid sites of 0TmSZ with that of 2TmSZ in Fig. 8.24 (a) it is interesting to notice that the amount of water influenced Brønsted acid sites remains constant, whereas the concentration of Lewis acid sites is halved. Our results confirm findings reported elsewhere that catalytic activity does not depend on total acidity [26, 79] but are in disagreement with the proposal that catalytic activity solely depends on the absolute amount of Brønsted acid sites [100]. The catalytic performance of SZ depends on the relative L/B ratio of surface acid centers combined with a high absolute value of H<sub>2</sub>O influenced Brønsted sites. Deviating from the findings of Breitskopf et al. who consider 3 % of the Brønsted centers to be

relevant for the catalytic performance, we suggest that all water influenced Brønsted centers, namely half of all Brønsted centers, contribute to catalytic activity.

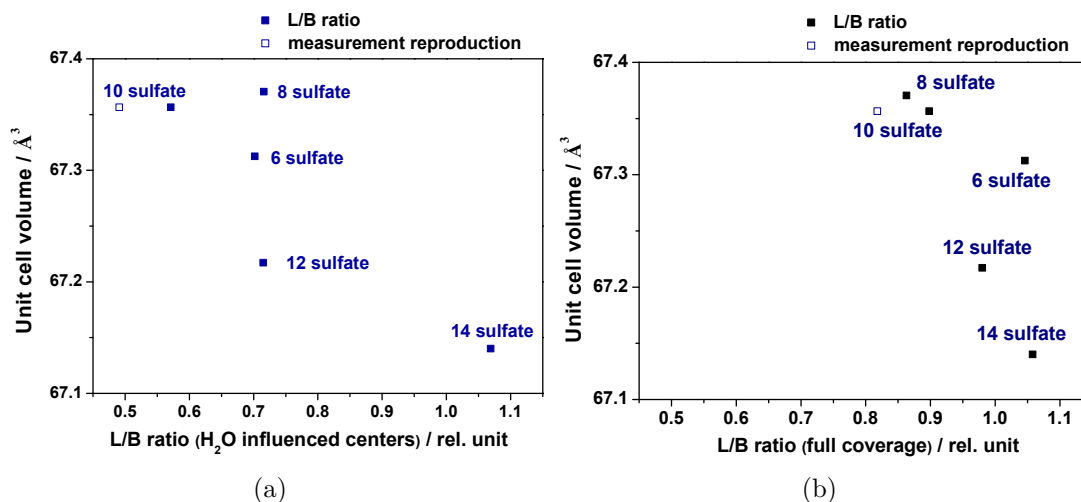


**Figure 8.25.:** Correlation between bulk and surface properties. L/B ratio versus unit cell volume for (a) the H<sub>2</sub>O influenced Brønsted sites, (b) full coverage of Brønsted sites. The best catalysts (2Tm) display the lowest L/B ratios. The values were determined using the peak areas of Lewis and Brønsted bands, which appear in the carbonyl stretching vibration region of IR difference spectra after CO adsorption on promoted SZ at  $-196^{\circ}\text{C}$ . Unit cell volumes were determined by Rietveld refinement.

Figure 8.25 displays a correlation of the unit cell volume with the L/B ratio for the Tm series, which is an obvious correlation between surface and bulk properties for increasing Tm contents. The L/B ratio decreases for increasing unit cell volume with the lowest L/B ratio and the highest unit cell volume for 2Tm10SZ, the catalyst with the highest *n*-butane isomerization rate and the lowest deactivation rate constant. The results for the sulfate series can be found in the Appendix (Fig. A.7), which show the same relationship but less resolved.

Figure 8.26 (a) demonstrates a correlation between L/B ratio with the long term deactivation rate constant. This confirms that the water influenced Brønsted acid sites belong to the active site and influence the catalytic performance. Therefore this correlation is less resolved in Figure 8.26 (b), where all Brønsted sites are plotted versus the long term deactivation rate constant. Figure A.8 (Appendix) show the same correlation for the sulfate series.

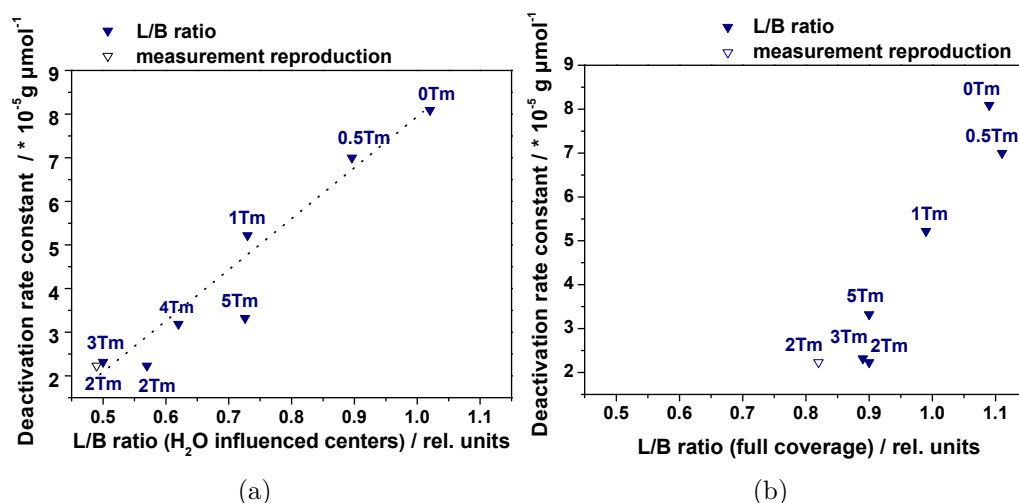


**Figure 8.26.:** Correlation between surface properties and deactivation rate constants. L/B ratio versus deactivation rate constant for samples of the Tm series (a) for H<sub>2</sub>O influenced Brønsted sites, (b) full coverage of Brønsted sites. L/B ratios were determined as described in Figure 8.25. Deactivation rate constants were calculated applying a linearized form of a second order deactivation kinetics for the long term deactivation of SZ in the *n*-butane isomerization.

## 8.2. Conclusion

With an optimized calcination temperature of 625 °C and continuous saturation of the argon gas flow with oleum during the calcination process all co-precipitated samples, including the unpromoted sample, were 100 % tetragonal. For the first time it was possible to assign unambiguously the tetragonal phase of the unpromoted SZ catalyst to its properties. It could be proven that the defects in the bulk structure correlate with the lattice volume for constant particle sizes (TEM/XRD). Relationships exist between the lattice volume and the L/B ratio on the catalyst surface as well as between L/B ratio and long term deactivation rate constant. The total pore volume correlates with the deactivation rate constant for Tm loading  $\geq 1$  mol%. This correlation is caused by a relationship between the abundance of big pores with a diameter between 30 and 40 Å and the long term deactivation rate constant, which might be explained by polymerization in these pores.

The catalyst with the highest rate of isobutane formation and the lowest deactivation rate constant is the catalyst promoted with 2 mol% thulium and 10 wt% sulfate, representing the intersection point of the two catalyst series. This catalyst is

characterized by the lowest BET surface area, the lowest total pore volume resulting from the lowest abundance of large diameter pores, the highest lattice volume caused by the largest lattice constant  $a$ , a superlorentzian peak form (highest mixing parameter ( $\mu$ )) and the biggest particle size (analyzed by TEM) as well as a low strain. Furthermore, it is characterized by the smallest value for the relative Lewis to Brønsted ratio and the highest absolute value for H<sub>2</sub>O influenced Brønsted acid sites on the catalyst's surface.

The obviously diverging bulk- and surface characteristics of the less active 4 and 5 mol% Tm catalysts suggest that, under the chosen conditions, a limit has been exceeded, at which thulium and sulfate from the surface starts to build up Tm<sub>x</sub>S<sub>y</sub>O<sub>z</sub> phases whose small amounts are neither detectable with XRD nor with EDX. The stable unit cell volumes for Tm contents > 3 mol% give an indication on this relationship. The apparent faulting probability, a measure for the defect density, further increases for higher thulium and sulfate loadings than 2 mol% thulium and 10 wt% sulfate, what suggests that the optimized catalysts need a stabilized defect structure, as found by low strain values with constant particle sizes for the optimum catalyst.

The fact that the BET surface area is the lowest for the catalysts with the highest performance, provides conclusive evidence that the intrinsic defect structure and not the tetragonal structure itself influences the surface of the material and therewith is responsible for an optimum catalytic activity. In the present study, Tm creates defects, most likely oxygen vacancies, that compensate for the lower valence of Tm<sup>3+</sup> ions relative to Zr<sup>4+</sup>. This leads to the formation of different defect structures in the zirconia lattice. For all investigated active catalysts of this study these structures are the same but differ in their quantities. These changes could only be unveiled by statistical counting of particles diameters from TEM images in combination with XRD peak profile analysis. The intrinsic defect structure is visible under the TEM as spotty contrasts due to point defects and dislocation lines. These dislocations were very frequently observed in the bulk structure of tetragonal SZ (Fig. 8.16). They cause numerous small angle grain boundaries, by which patchwork-like domains are formed (Fig. 6.7). It is assumed that the stabilized defect structure is formed by thulium migrating into the dislocation lines, by decorating those and being fixed there (Cottrell atmosphere model). As a result the defect structure remains stable under reaction conditions at 100 °C.



Therefore, defects in the bulk structure influence indirectly the catalytic performance of SZ in the isomerization. This effect outweighs the effect of variation of sulfate content on the surface. Since the variation of sulfate content systematically changes the unit cell volume, it can be concluded that it is partly incorporated into the bulk structure or affects the incorporation of the promoter. The effect of varied  $T_m$  versus varied sulfate concentration seems to be identical for most of the investigated properties but differ in their impact on the final product. For all investigated properties, the effect of bulk changes prevails the direct variation of surface sulfate concentration. These results contradict findings of Marcus et al. [64], who claimed the surface concentration of sulfate to be the most important factor for catalytic activity of the final product.

By the separated variation of bulk versus surface properties we could verify our basic hypothesis that defects, as high energy sites on the catalyst surface, are necessary for the formation of active centers. These centers are compromised of surface defects and closely spaced disulfate groups and water. The concentration of Lewis and Brønsted acids sites decreases for increasing  $T_m$  contents. The difference in amount of Lewis and Brønsted acid sites is the greatest for the best performing catalyst, resulting in the lowest L/B ratio (Fig. 8.26). The amount of water influenced Brønsted sites is, for all investigated samples, approximately half of the total amount of Brønsted acid sites. We could demonstrate that only these water influenced Brønsted acid site are relevant for catalytic activity. This seems to be in conflict with findings of Breitung et al. [100] who assumed that only the most acidic Brønsted sites – 3 % of all Brønsted sites – would be relevant for the catalytic reaction. We conclude that the catalytic performance of SZ depends on the relative L/B ratio of surface acid centers combined with a high absolute value of  $H_2O$  influenced Brønsted sites, which can be tailored by variation of the defect density in the tetragonal structure of SZ.



## 9. Final conclusion

The objective of this thesis was to elucidate the influence of defects in the tetragonal structure of sulfated zirconia catalysts on their physical properties and catalytic activity in *n*-butane isomerization. The basic assumption is that defects – which function as high energy sites on the catalyst surface – are required for the formation of active centers. These active centers are thought to be composed of surface defects and closely spaced disulfate groups.

Since it is known that the storage conditions influence the performance of SZ catalysts drastically [79, 104], catalyst aging was initially investigated. As water adsorption on the catalyst surface is the main cause of catalyst aging, the contact time with air plays the most important role in the aging process. Extending the findings of Klose [104], who claimed the laboratory cupboard to be the best place for SZ catalyst storage, aging could be further diminished by storage in air tight containers or by storage in a double walled container inside a secador desiccator cabinet (Chapter 4).

Characterization methods, specifically devised for this system were applied. These methods included the determination of the ratio of Lewis to Brønsted acid sites (L/B) with CO adsorption in combination with IR spectroscopy and the combination of TEM and XRD to find a measure for the defect density and structure in the bulk. Besides point defects, which were identified under the TEM as spotty contrast features, further dislocation lines were very frequently visible in the bulk structure of tetragonal SZ (Fig. 8.16). Arrays of these lines separate individual domains by small angle boundaries (Fig. 6.7) in the structure.

The evolution of the active phase of SZ during calcination was studied in detail (Chap. 5). Hahn et al. [28] assumed that the active phase is formed in kinetically controlled reactions during rapid overheating (glow phenomenon – an exothermic reaction during calcination) and proposed that defects in the bulk would be quenched through a fairly rapid cool-down after the glow. The results within this thesis

however, disagree with the above hypothesis, since the evolution of the active phase during calcination was found to be a gradual process. Moreover, it can be concluded that further bulk (defect migration) and surface modifications (of the surface sulfate groups) are necessary to form an active, defective material after the glow phenomenon. Additionally, it was observed that the simultaneous complete crystallization takes place during the heat-up ramp of the calcination program; before isothermal conditions are reached. Nevertheless, the dramatic influence of the calcination step on the final product remains unquestioned. The defect arrangement inside the structure is kinetically controlled at elevated temperatures (mainly the holding temperature) during calcination.

Based on the aforementioned results, the influence of individual calcination parameters on the final product was investigated (Chapter 6). For this purpose, parameters including temperature, time, oxygen partial pressure and gas flow rate were varied individually for unpromoted SZ. A completely air tight rocking furnace was used in order to avoid the influences of the glow phenomenon and geometric effects as well as allowing for the possibility for upscaling. With these precautions, a calcinations procedure without a measurable glow phenomena was achieved. For the effects of the most frequently investigated, such as calcination temperature or time, contradictory results were often found in the literature (e.g. [30, 107]). We have confirmed that these two parameters have the biggest impact on catalyst performance during *n*-butane isomerization, and additionally found that the gas flow rate and oxygen partial pressure also influence catalyst performance. The best calcination conditions for unpromoted SZ were determined to be: 550 °C, 3 h, 500 mL/min 100 % Ar. This sample is characterized by high values of defect density in the bulk structure, surface sulfate content, BET surface area, and rate of isobutane formation, as well as by the lowest L/B ratio of surface acid centers. Most varied calcination parameters influenced bulk and surface properties at the same time.

Li et al. [30] found that the catalytic activity of a given catalyst was increased after a post calcination treatment with gaseous SO<sub>3</sub>. In order to investigate the additional influence of surface treatments, the gas phase was saturated (Chapter 7): with sulfuric acid and water during calcination, and an ex-situ post calcination treatment with sulfur trioxide was performed respectively. It was possible to almost double the catalytic performance of an optimized, defect rich catalyst by the use of gas phase

---

treatment with  $\text{SO}_3$  without inducing changes in the bulk structure. That means that for a defect rich bulk structure of SZ, the catalytic performance can be further increased by treatments that directly target the surface. However, the *n*-butane isomerization on the aforementioned catalysts is unstable as evidenced by second order deactivation kinetics measurements (Figs. 2.10 and 2.9). These measurements show an initiation mechanism of the reaction (oxidative dehydrogenation [63]) after 5 to 7 h and further deactivation after more than 250 h on stream. Because of this lack of steady state conditions, it follows for industrial applications that even running an optimized SZ catalyst in the isomerization of light alkanes does not provide an alternative to the more complex hydroisomerization over Pt impregnated promoted SZ.

To study the effect resulting from either direct surface treatments or from bulk structure modification on catalyst performance, we have synthesized two series of catalysts. In the first series – we introduced defects in the bulk structure by the use of varying amounts of thulium as promoter. In the second series, the surface properties were influenced directly by introducing varying amounts of surface sulfate, while keeping the promoter content constant. Both series intersected at the catalyst with the highest performance (2 mol% thulium and 10 wt% sulfate). By automated co-precipitation and subsequent calcination under continuous saturation of the inlet gas flow with oleum, we successfully prepared phase pure tetragonal, promoted and unpromoted samples under identical calcination conditions. It was possible to unambiguously assign the tetragonal phase as a property of the unpromoted SZ catalyst. For promoted SZ catalysts, it was found that the thulium concentration controls the defect density in the bulk and the total pore volume. Defects in the bulk structure linearly correlate with the lattice volume, which in turn correlate with the L/B ratio on the catalysts surface. The L/B ratio, in turn correlates with the long term deactivation rate constant of the *n*-butane isomerization on these catalysts. Therefore defects in the bulk structure influence indirectly the catalytic performance of SZ in the isomerization. High defect concentrations in the tetragonal phase lead to low L/B ratios on the catalysts surface, resulting in high isobutane formation rates and small long-term deactivation rate constants. The effect of thulium in the bulk structure is stronger than the effect of variation of sulfate content. Since the variation of sulfate content systematically changes the unit cell volume, it can be

concluded that sulfate is partly incorporated into the bulk structure or affects the incorporation of the promoter.

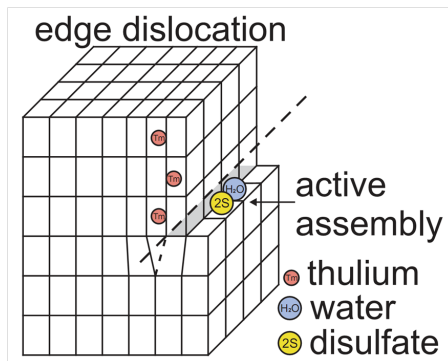


**Figure 9.1.:** Model for Tm promoted SZ

Finally, we could verify our basic hypothesis that defects, as high energy sites on the catalyst surface, are necessary for the formation of active centers. These active centers were investigated by IR spectroscopy and CO adsorption. It was demonstrated that only the water influenced Brønsted acid sites, provided by special disulfate groups (Sect. 6.1.6), contribute to catalytic activity, meaning approximately half of the Brønsted sites. This fact is in line with findings of Bretkopf et al. [100], who assumed that only a fraction of Brønsted sites (3 %) would be relevant. In contrast to their study, however, the percentage of relevant Brønsted sites that we found is much higher (50 %).

The main results of this study are combined in a model shown in Figure 9.1. If the larger Tm substitutes for Zr, it creates a local microstrain field and dislocations. The resulting general strain field is reduced by Tm migrating and being pinned in dislocations lines. Thereby the dislocations are fixed in place (Cottrell atmosphere model) and create a stabilized defect structure, which remains stable even at the reaction temperature of 100 °C. Dislocations result in steps and relaxations on the surface of SZ on which water influenced Brønsted acid sites act as active sites for the isomerization of light alkanes.

Generally, it can be concluded that intrinsic defects in the tetragonal structure, and not the structure itself, determine the surface properties of an active SZ catalyst. Accordingly, the catalytic performance and stability in the isomerization of light alkanes is controlled by lattice imperfections. The defect density inside

---

the tetragonal lattice, as well as the isolation of this phase, can be governed by controlled preparation and calcination. A stabilized defect structure together with a low L/B ratio and a high concentration of water influenced Brønsted acid sites on the surface are the key features of high-performance SZ catalysts. This knowledge can be used as a basis to tailor highly active catalyst materials with specifically desired bulk and surface characteristics for industrial applications. This study provides experimental evidence for a general concept in heterogeneous catalysis, namely that the defect structure in the bulk of nano-sized particles affect their surface properties – leading to a small number of very active metastable surface ensembles. This phenomenon has been discussed for metal-based catalysts like Cu/ZnO/Al<sub>2</sub>O<sub>3</sub>, oxidation catalysts such as mixed MoVTe oxides and has now been extended to acid catalysts, namely sulfated zirconia.





## 10. Outlook

The present study illuminated the influence of lattice imperfections on the surface and therewith on the catalytic performance of SZ in the *n*-butane isomerization as model system. In further studies it would be interesting to investigate this relationship in the stable system. The industrially performed hydroisomerization of light alkanes is more complex since two additional influences, namely the influence of additional platinum impregnation and the use of hydrogen during the reaction, might change the impact of the factors investigated in this study. It is known from literature, that the presence of platinum should not alter the L/B ratio of acid sites on the surface of SZ [120], however the additional contribution of hydrogen in the reaction is still unknown. The use of hydrogen should lead to partial reduction of zirconium on the surface of the catalyst. Therefore it is suggested to compare the state of the catalyst's bulk and surface with the help of TEM/XRD analysis combined with CO adsorption at  $-196\text{ }^{\circ}\text{C}$  and IR spectroscopy – the two successfully applied methods in the present study – in order to investigate their properties before and after hydroisomerization. This should lead to a deeper understanding of the more complex system. Preliminary experiments suggested that the aforementioned results are transferable, however this hypothesis has yet to be confirmed.



# A. Appendix

## A.1. Tables of the deactivation properties

**Table A.1.:** Deactivation: gas flow series

Gas flow (mL)	$c_{deact}$ ( $\cdot 10^{-5}$ g $\mu\text{mol}^{-1}$ )	$R^2/N$	start linear regime (h)
100	2.197	$\frac{0.991}{49}$	7.3
400	2.084	$\frac{0.979}{45}$	8.9
500	2.075	$\frac{0.993}{52}$	7.2
600	2.575	$\frac{0.990}{53}$	7.2
750	2.702	$\frac{0.982}{58}$	5.9
900	2.642	$\frac{0.994}{49}$	6.3

**Table A.2.:** Sample properties: oxygen partial pressure series

Ar content (%)	$c_{deact}$ ( $\cdot 10^{-5}$ g $\mu\text{mol}^{-1}$ )	$R^2/N$	start linear regime (h)
100	2.075	$\frac{0.993}{52}$	7.5
80	2.157	$\frac{0.977}{51}$	6.6
50	2.292	$\frac{0.989}{42}$	9.2
20	2.268	$\frac{0.985}{44}$	7.8
0	2.387	$\frac{0.987}{46}$	7.3

## A.2. Tables of the determination of the sulfate content

**Table A.3.:** Varied parameters

Treatment	Sulfate content / wt%	BET surface area / m <sup>2</sup> g <sup>-1</sup>
optimized	7.9	193
+ sulfuric acid	7.7	184
+ water	6.9	144
+ sulfuric acid	7.7	184
+ Oleum	8.4	174
+ SO <sub>3</sub>	10.8	173
+ Oleum + SO <sub>3</sub>	11.1	147

**Table A.4.:** Varied parameters

Treatment	Sulfate content / wt%	BET surface area / m <sup>2</sup> g <sup>-1</sup>
optimized	7.9	193
+ sulfuric acid	7.7	184
+ water	6.9	144
+ sulfuric acid	7.7	184

### A.3. Aging-correction

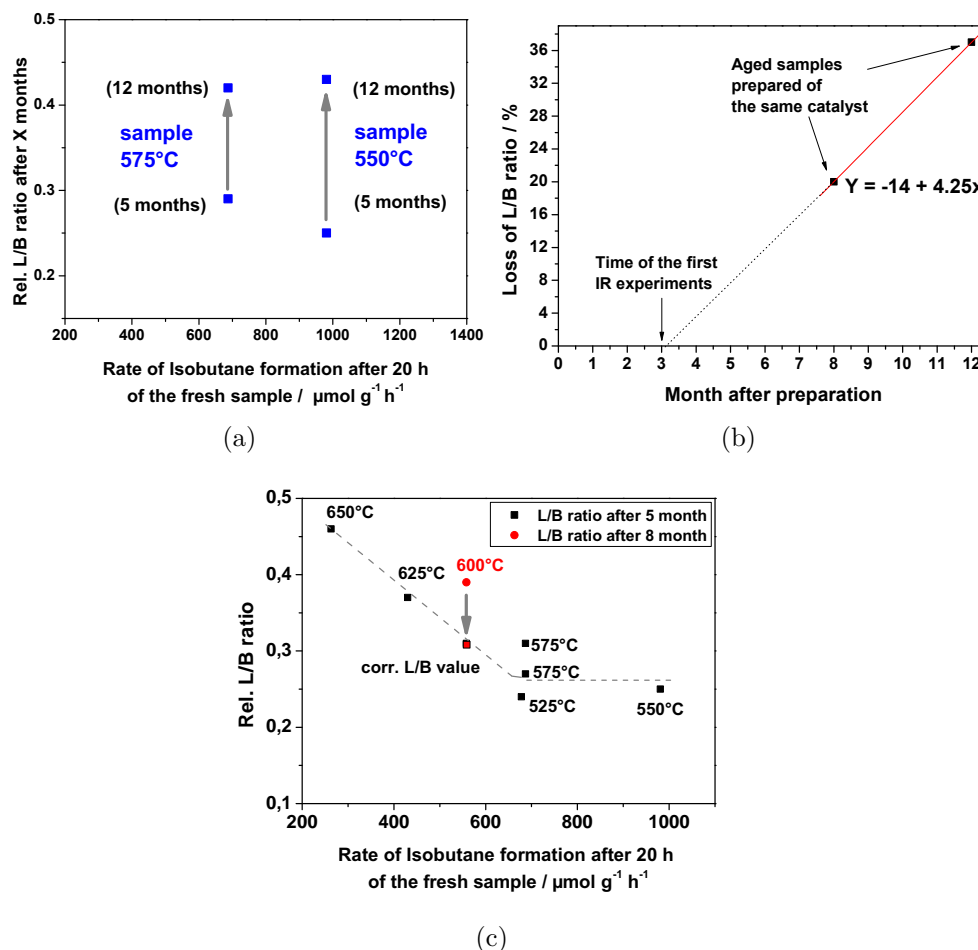


**Figure A.1.:** Corrections for catalyst aging of catalysts which were often in use. This use caused unavoidable contact to humidity. Despite optimized catalysts storage conditions, several catalysts suffered from aging. Since the order of magnitude of the aging effect (Fig. 4.2) is comparable for all investigated samples of the calcination series this effect could be determined and corrected. (a) Change of the rel. L/B ratio with time after calcination versus rate of isobutane formation of the fresh SZ sample for two different samples. (b) Linear fit for the determination of the aging effect. With this linear dependency, the aging effect could be corrected by a percentaged correction factor. (c) The correction was verified with the temperature series: Measured and mathematically corrected value for the 600°C sample. With the exception of this sample, the series was measured after 5 month. After correction, this sample confirms the trend of the temperature series: decreasing relative L/B ratios with increasing catalytic activity with a saturation range around the optimum calcination temperature of 550 °C.

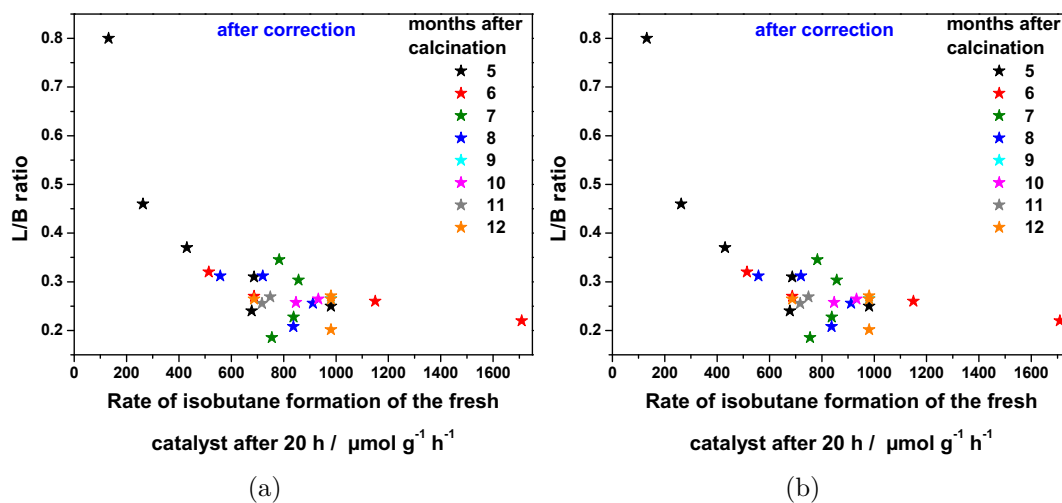


**Figure A.2.:** Relative L/B ratios for all investigated SZ samples of the calcination and gas series versus rate of isobutane formation after 20 h of the fresh sample (a) before aging correction (b) after aging correction as described in Figure A.1. After aging correction the general trend of low L/B ratios for high performance catalysts is better visible.

## A.4. Figures of sulfate series of promoted SZ

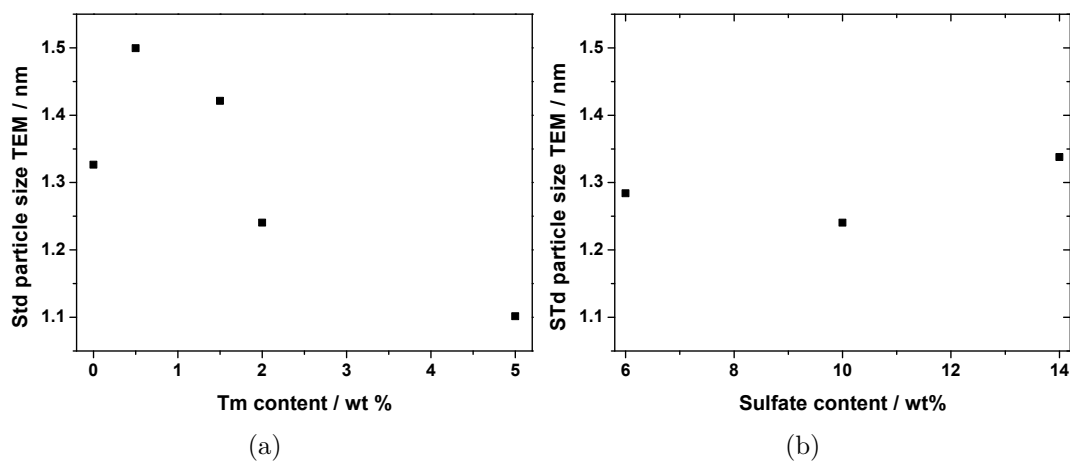


**Figure A.3.:** Standard deviation of the particle size determined by TEM analysis (a) Tm series, (b) sulfate series. The illustrated standard deviations do not show any trend. This is a prerequisite for the use of the TEM particle size diameters for the determination of the apparent faulting probability.

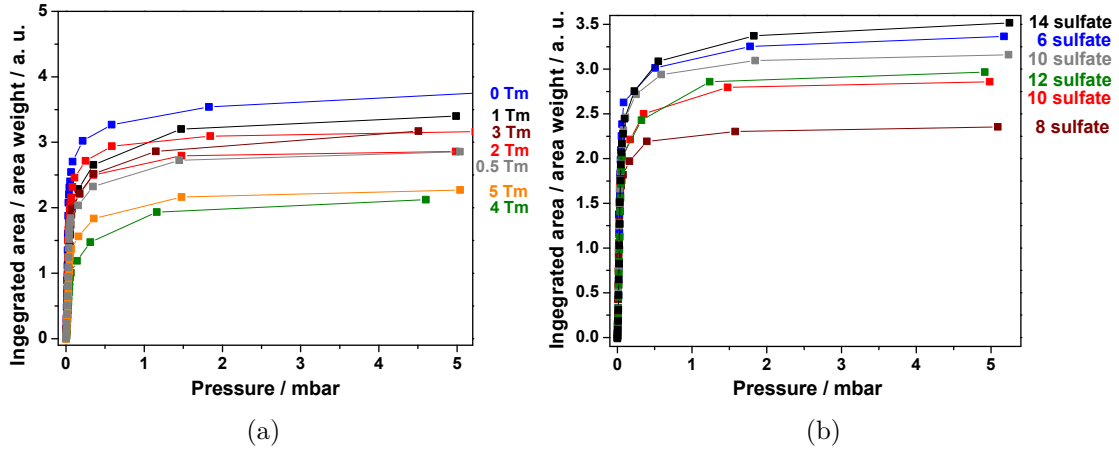


**Figure A.4.:** Saturation of adsorbed CO for (a) the Tm series, (b) sulfate series up to the highest investigated CO partial pressure. At high CO partial pressures the spectra are dominated by physisorbed CO bands. Fitting produces an error due to which is impossible to quantify correctly the Brønsted sites. Therefore high CO partial pressure cannot be used for the determination of the Lewis and Brønsted acid sites.

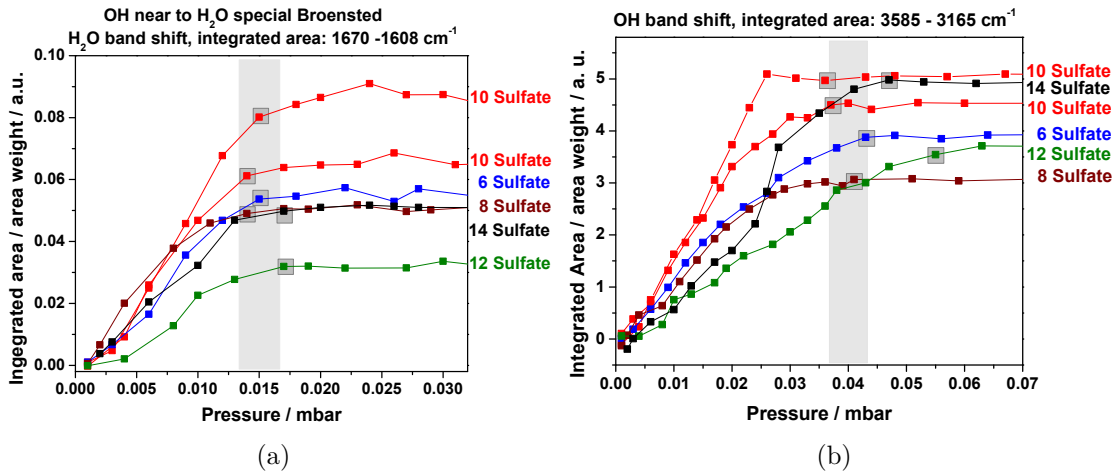


**Figure A.5.:** Integrated peak areas for increasing pressure of CO adsorption on samples with varied sulfate contents. Saturation of (a) H<sub>2</sub>O influenced Brønsted sites at  $\approx 0.015$  mbar, (b) full coverage of Brønsted sites at  $\approx 0.04$  mbar illustrating the individual investigated pressure for the sulfate series. The investigated pressure ranges are comparable the those of the Tm series.

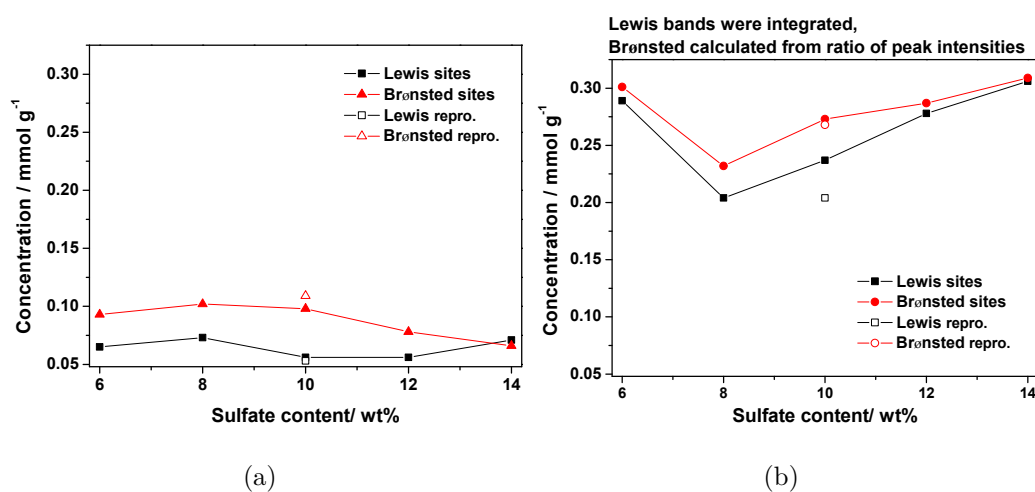


**Figure A.6.:** Concentration of Lewis and Brønsted acids sites versus sulfate content: (a) for H<sub>2</sub>O influenced Brønsted sites, (b) full coverage of Brønsted sites illustrating a decreasing trend of both sites for increasing sulfate contents. The peak areas of Lewis and Brønsted bands were fitted and the side concentrations were calculated by using an extinction coefficient of  $\epsilon_{2187} = 2.5 \text{ cm}/\mu\text{mol}$  selected from the literature. In (b) only the peak areas of Lewis bands could be integrated, Brønsted bands had to be calculated from peak intensities due to overlapping band of physisorbed species.



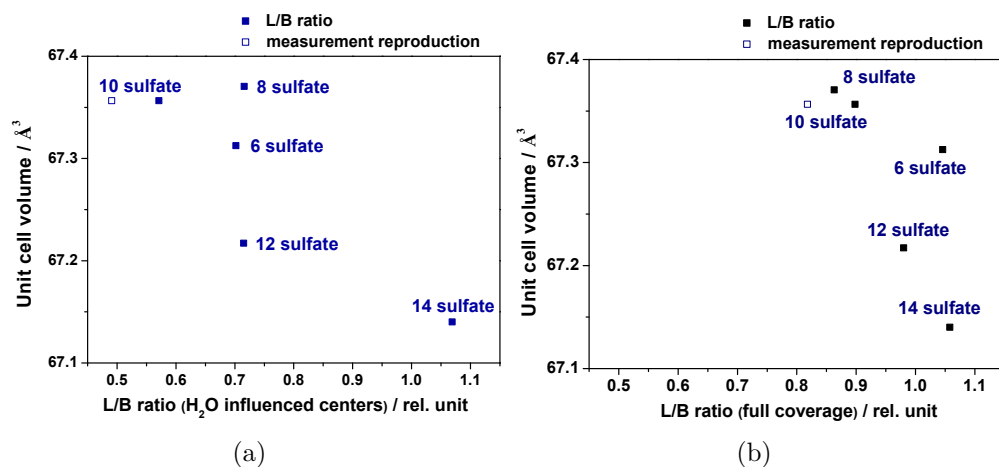


**Figure A.7.:** Correlation between bulk and surface properties: L/B ratio versus unit cell volume for (a) the H<sub>2</sub>O influenced Brønsted sites, (b) full coverage of Brønsted sites. The best catalysts (2Tm) display the lowest L/B ratios. The values were determined using the peak areas of Lewis and Brønsted bands, which appear in the carbonyl stretching vibration region of IR difference spectra after CO adsorption on promoted SZ at  $-196^{\circ}\text{C}$ . Unit cell volumes were determined by Rietveld refinement.

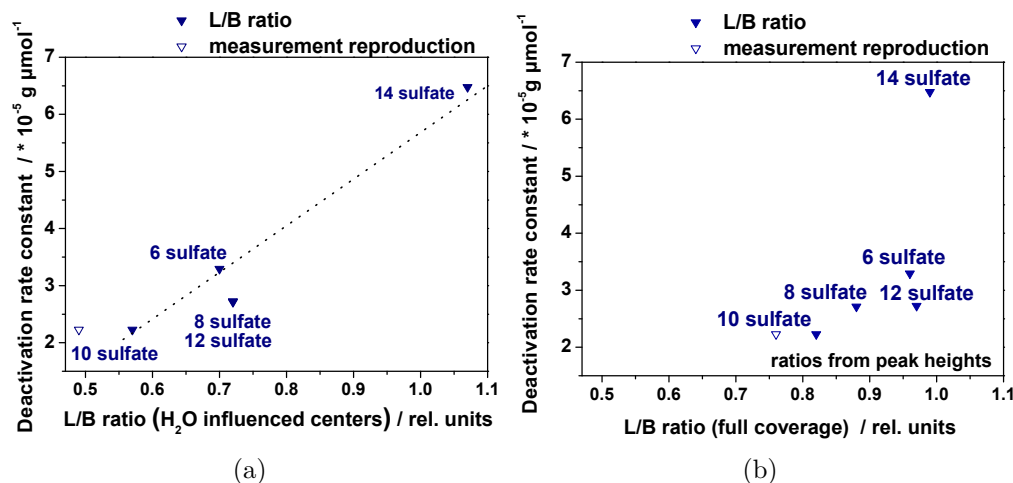


**Figure A.8.:** Correlation between surface properties and deactivation rate constants: L/B ratio versus deactivation rate constant for the sulfate series (a) for H<sub>2</sub>O influenced Brønsted sites, (b) full coverage of Brønsted sites. L/B ratios were determined as described in Figure A.7. Deactivation rate constants were calculated applying a linearized form of a second order deactivation kinetics for the long term deactivation of SZ in the *n*-butane isomerization.

## A.5. Identification of the samples

**Table A.5.:** Evolution

Number	treatment	FHI Database number / SN
1	450°C	4707, 4708
2	480°C	4698, 4699
3	1 sec. before peak max.	4608, 4609
4	1 sec. after peak max.	4696, 4697
5	hold for 1h at 550°C	4701, 4702
6	hold for 2h at 550°C	4705, 4706
7	hold for 3h at 550°C	4703, 4704

**Table A.6.:** Optimization: temperature series

Varied parameter	constant parameters	FHI Database number / SN
525°C	3 h, 500 ml/min, 100% Ar	6752
550°C	3 h, 500 ml/min, 100% Ar	6735
575°C	3 h, 500 ml/min, 100% Ar	6747
600°C	3 h, 500 ml/min, 100% Ar	6741
625°C	3 h, 500 ml/min, 100% Ar	6744
650°C	3 h, 500 ml/min, 100% Ar	6745

**Table A.7.:** Optimization: time series

Varied parameter	constant parameters	FHI Database number / SN
1 h	550°C, 500 ml/min, 100% Ar	6752
2 h	550°C, 500 ml/min, 100% Ar	6735
3 h	550°C, 500 ml/min, 100% Ar	6747
4 h	550°C, 500 ml/min, 100% Ar	6741
6 h	550°C, 500 ml/min, 100% Ar	6744
12 h	550°C, 500 ml/min, 100% Ar	6745
21 h	550°C, 500 ml/min, 100% Ar	6745

**Table A.8.:** Optimization: oxygen partial pressure series

Varied parameter	constant parameters	FHI Database number / SN
0 % Ar	550°C, 3 h, 500 ml/min	6752
20% Ar	550°C, 3 h, 500 ml/min	6735
50% Ar	550°C, 3 h, 500 ml/min	6747
80% Ar	550°C, 3 h, 500 ml/min	6741
80% Ar	550°C, 3 h, 500 ml/min	6744
100% Ar	550°C, 3 h, 500 ml/min	6745

**Table A.9.:** Optimization: gas flow series

Varied parameter	constant parameters	FHI Database number / SN
100 ml/min	550°C, 3 h, 100% Ar	7008
400 ml/min	550°C, 3 h, 100% Ar	6739
500 ml/min	550°C, 3 h, 100% Ar	6735
750 ml/min	550°C, 3 h, 100% Ar	6737
1000 ml/min	550°C, 3 h, 100% Ar	6738

**Table A.10.:** Gas saturation

gas saturated with	during/after calcination	constant parameters	FHI Database number / SN
water	during	550°C, 3 h, 500 ml/min 100% Ar	6862
H <sub>2</sub> SO <sub>4</sub>	during	550°C, 3 h, 500 ml/min, 100% Ar	6863
oleum	during	550°C, 3 h, 500 ml/min, 100% Ar	6867
SO <sub>3</sub>	after	550°C, 3 h, 500 ml/min, 100% Ar	7999
oleum	during	550°C, 3 h, 500 ml/min, 100% Ar	7998
+SO <sub>3</sub>	+ after		

**Table A.11.:** Promoter Series

Name	Tm content / mol%	sulfate content / wt%	FHI Database number / SN
0TmSZ	0	10	7999
0.5TmSZ	0.5	10	8008
1TmSZ	1	10	7072
1.5TmSZ	1.5	10	7863
2TmSZ	2	10	7859
3TmSZ	3	10	8073
4TmSZ	4	10	7861
5TmSZ	5	10	7862

**Table A.12.:** Sulfate series

Name	sulfate content / wt%	Tm content / mol%	FHI Database number / SN
2Tm6SZ	6	2	8011
2Tm8SZ	8	2	8074
2Tm10SZ	10	2	7859
2Tm12SZ	12	2	8012
2Tm14SZ	14	2	8013

# Bibliography

- [1] A. Corma, *Chem. Rev.*, **1995**, 95(3), 559–614.
- [2] V. C. F. Holm, G. C. Bailey; US patent 3 032 599, **1962**.
- [3] M. Hino, S. Kobayashi, K. Arata, *J. Am. Chem. Soc.*, **1979**, 101(21), 6439–6441.
- [4] M. Hino, K. Arata, *Chem. commun.*, **1980**, (18), 851–852.
- [5] K. Arata, H. Matsushashi, M. Hino, H. Nakamura, *Catal. Today*, **2003**, 81(1), 17–30.
- [6] I. Kasatkin, P. Kurr, B. Kniep, A. Trunschke, R. Schlögl, *Angew. Chem. Int. Ed*, **2007**, 46, 7324–7327.
- [7] A. Celaya Sanfiz, T. W. Hansen, D. Teschner, P. Schnörch, F. Girgsdies, A. Trunschke, R. Schlögl, M. Hong Looi, S. Bee Abd Hamid, *J. Phys. Chem. C*, **2010**, 114, 1912–1919.
- [8] A. Trunschke; Department seminar talk, FHI der MPG, AC department, 05.05.2010.
- [9] P. Li, I. W. Chen, J. E. Penner-Hahn, *Phys. rev. B, Condensed matter*, **1993**, 48(14), 10063–10073.
- [10] C. R. Vera, C. L. Pieck, K. Shimizu, J. M. Parera, *Appl. Catal. A: General*, **2002**, 230(1-2), 137–151.
- [11] R. C. Gravie, *J. Phys. Chem.*, **1978**, 82, 218–223.
- [12] I. Molodetsky, A. Navrotsky, M. J. Paskowitz, V. J. Leppert, S. H. Risbud, *J. Non-Cryst. Solids*, **2000**, 262(1-3), 106–113.

- [13] X. Guo, *Chem. Mat.*, **2004**, 16(21), 3988–3994.
- [14] P. Li, I. W. Chen, J. E. Penner-Hahn, *J. Am. Ceram. Soc.*, **1994**, 77(5), 1281–1288.
- [15] T. Yamaguchi, T. Morita, T. M. Salama, K. Tanabe, *Catal. Lett.*, **1990**, 4(1), 1–6.
- [16] T. Van Dijk, K. J. de Vries, A. J. Burggraaf, *Physica status solidi. A, Applied research*, **1980**, 58(1), 115–125.
- [17] B. S. Klose, R. E. Jentoft, A. Hahn, T. Ressler, J. Kröhnert, S. Wrabetz, X. Yang, F. C. Jentoft, *J. Catal.*, **2003**, 217(2), 487–490.
- [18] R. Srinivasan, T. R. Watkins, C. R. Hubbard, B. H. Davis, *Chem. Mat.*, **1995**, 7(4), 725–730.
- [19] I. V. Bobricheva, I. A. Stavitsky, V. K. Yermolaev, N. S. Kotsarenko, V.P. Shmachkova, D.I. Kochubey, *Catal. Lett.*, **1998**, 56(1), 23–27.
- [20] C. R. Vera, C. L. Pieck, K. Shimizu, J. M. Parera; Preparation of supported so42-zro2 for isomerization of n-butane; In *Preparation of catalysts VII*, Vol. 118, pages 369–376, 1998.
- [21] R. Boyse, E. I. Ko, *J. Catal.*, **1998**, 179(1), 100–110.
- [22] P. Nascimento, *Stud. Surf. Sci. Catal.*, **1993**, 75, 1185–1197.
- [23] G. Cerrato, C. Morterra, M. Rodríguez Delgado, C. Otero Areán, M. Signoretto, F. Somma, F. Pinna, *Microporous Mesoporous Mat.*, **2006**, 94(1-3), 40–49.
- [24] Jong Rack Sohn, Tae-Dong Kwon, Sang-Bock Kim, *Bull. Korean Chem.*, **2001**, 22, 1309–1315.
- [25] D. Ward, E. Ko, *J. Catal.*, **1994**, 150(1), 18–33.
- [26] R. A. Comelli, S. A. Canavese, S. R. Vaudagna, N. S. Fígoli, *Appl. Catal. A: General*, **1996**, 135(2), 287–299.

- 
- [27] C. J. Norman, P. A. Goulding, I. Mc Alpine, *Catal. Today*, **1994**, 20(2), 313–322.
- [28] A. Hahn, R. E. Jentoft, T. Ressler, G. Weinberg, R. Schlögl, F. C. Jentoft, *J. Cat.*, **2005**, 236(2), 324–334.
- [29] Y. Murase, E. Kato, *J. Am. Ceram. Soc.*, **1983**, 66(3), 196–200.
- [30] X. Li, K. Nagaoka, L. J. Simon, R. Olindo, J. A. Lercher, *Catal. Lett.*, **2007**, 113(1-2), 34–40.
- [31] F. Haase, J. Sauer, *J. Am. Chem. Soc.*, **1998**, 120, 13503–13512.
- [32] M. Signoretto, S. Melada, F. Pinna, S. Plezzi, G. Cerrato, C. Morterra, *Microporous Mesoporous Mat.*, **2005**, 81(1-3), 19–29.
- [33] E. Frolova, *Diffusion and defect data. Pt. A, Defect and diffusion forum*, **2005**, 242-244, 143–158.
- [34] A. Hahn, T. Ressler, R. E. Jentoft, F. C. Jentoft, *Chem. comm.*, **2001**, (6), 537–538.
- [35] C.-Y. Hsu, C. R. Heimbuch, C. T. Armes, B. C. Gates, *J. Chem. Soc. Chem. Comm.*, **1992**, (22), 1645–1646.
- [36] E. J. Hollstein, J. T. Wei, C.-Y. Hsu; Us patent 4 918 041, **1990**.
- [37] E. J. Hollstein, J. T. Wei, C.-Y. Hsu; Us patent 4 956 519, **1990**.
- [38] M. A. Coelho, D. E. Resasco, E. C. Sikabwe, R. L. White, *Catal. Lett.*, **1995**, 32(3-4), 253–262.
- [39] F. C. Lange, T.-K. Cheung, B. C. Gates, *Catal. Lett.*, **1996**, 41(1-2), 95–99.
- [40] J. C. Yori, J. M. Parera, *Appl. Catal. A: General*, **1996**, 147(1), 145–157.
- [41] C. Miao, W. Hua, J. Chen, Z. Gao, *Catal. Lett.*, **1996**, 37(3-4), 187–191.
- [42] Z. Gao, Y. Xia, W. Hua, C. Miao, *Topics in Catalysis*, **1998**, 6(1-4), 101–106.

- [43] M. Perez-Luna, A. Cosultchi, J. Toledo-Antonio, E. Aree-Estrada, *Catal. Lett.*, **2005**, *102*(1-2), 33–38.
- [44] J. Moreno, G. Poncelet, *J. Catal.*, **2001**, *203*(2), 453–465.
- [45] B. S. Klose, F. C. Jentoft, R. Schlögl, *J. Catal.*, **2005**, *233*, 68–80.
- [46] B. S. Klose, F. C. Jentoft, R. Schlögl, I. R. Subbotina, V. B. Kazansky, *Langmuir*, **2005**, *21*(23), 10564–10572.
- [47] J. A. Moreno, G. Poncelet, *Appl. Catal. A: General*, **2001**, *210*(1-2), 151–164.
- [48] K. Sasaki, J. Maier, *Solid State Ionics*, **2000**, *134*(3-4), 303–321.
- [49] J.-H. Wang, C.-Y. Mou, *Microporous Mesoporous Mat.*, **2008**, *110*(2-3), 260–270.
- [50] V. Adeeva, J. W. de Haan, J. Janchen, G. D. Lei, V. Schunemann, L. J. M. van de Ven, W. M. H. Sachtler, R. A. van Santen, *J. Catal.*, **1995**, *151*(2), 364–372.
- [51] W. Wang, C.-L. Chen, N.-P. Xu, S. Han, T. Li, S. Cheng, C. Y. Mou, *Catal. Lett.*, **2002**, *83*(3-4), 281–285.
- [52] F. C. Jentoft, A. Hahn, J. Kröhnert, G. Lorenz, R. E. Jentoft, T. Ressler, U. Wild, R. Schlögl, C. Häßner, K. Köhler, *J. Catal.*, **2004**, *224*(1), 124–137.
- [53] B. S. Klose, R.E. Jentoft, F.C. Jentoft.
- [54] R. J. Gillespie, M. J. Cohn; Us patent wo 03/020420 a1, **2003**.
- [55] G. A. Olah, Y. Halpern, J. Shen, Y. K. Mo, *J. Am. Chem. Soc.*, **1973**, *95*, 4960–4970.
- [56] R. J. Gillespie, *Accounts of Chemical Research*, **1968**, *1*, 202–209.
- [57] J. B. Nicholas, J. F. Haw, L. W. Beck, T. R. Krawietz, D. B. Ferguson, *J. Am. Chem. Soc.*, **1995**, *117*(49), 12350–12351.
- [58] B. S. Umansky , W. K. Hall, *J. Catal.*, **1990**, *124*(1), 97.



- 
- [59] L. M. Kustov, V. B. Kasansky, F. Figueras, D. Tichit, *J. Catal.*, **1994**, *150*, 143–149.
- [60] F. Babou, B. Bigot, P. Sautet, *J. Phys. Chem.*, **1993**, *97*(44), 11501.
- [61] X. Song, A. Sayari, *Catal. Rev. Sci. Eng.*, **1996**, *38*(3), 329–412.
- [62] S. Kim, J. G. Goodwin, D. Galloway, *Catal. Today*, **2000**, *63*(1), 21–32.
- [63] X. Li, K. Nagaoka, L. J. Simon, R. Olindo, J. A. Lercher, A. Hofmann, J. Sauer, *J. Am. Chem. Soc.*, **2005**, *127*(46), 16159–16166.
- [64] R. L. Marcus, R. D. Gonzalez, E. Kungler, A. Auroux, *Chem. Eng. Comm.*, **2003**, *190*, 1601–1619.
- [65] M. Benistel, O. Saur, J. C. Lavalley, G. Mabilon, *Mater. Chem. Phys.*, **1987**, *17*, 249–258.
- [66] V. S. Komarov, M. F. Sinilo, *Kinet. Catal.*, **1988**, *29*, 605–609.
- [67] F. R. Chen, G. Coudurier, J.-F. Joly, J. C. Vedrine, *J. Catal.*, **1993**, *143*, 616–626.
- [68] T. Jin, T. Yamaguchi, K. Tanabe, *J. Phys. Chem.*, **1986**, *90*, 4794–4796.
- [69] E. C. Sikabwe, M. A. Coelho, D. E. Resasco, R. L. White, *Catal. Lett.*, **1995**, *34*(1-2), 23–30.
- [70] R. Srinivasan, R.A. Keogh, A. Ghenciu, D. Fărcașiu, B.H. Davis, *J. Catal.*, **1996**, *158*(2), 502–510.
- [71] C. Morterra, G. Ceratto, *Phys. Chem. Chem. Phys.*, **1999**, *1*(11), 2825–2831.
- [72] X. Li, K. Nagaoka, L. J. Simon, J. A. Lercher, S. Wrabetz, F. C. Jentoft, C. Breitskopf, S. Matysik, H. Papp, *J. Catal.*, **2005**, *230*(1), 214–225.
- [73] M. Bensitel, O. Saur, J.-C. Lavally, *Mater. Chem. Phys.*, **1988**, *19*, 147–154.
- [74] C. Morterra, G. Cerratoa, V. Bolis, *Catal. Today*, **1993**, *17*(3), 505–515.
- [75] A. Hofmann, J. Sauer, *J. Phys. Chem. B*, **2004**, *108*(38), 14652–14662.

- [76] R. Lloyd; *Investigations on Sulfated Zirconia Model Systems: from Nanocrystalline Thin Films to Rational Design of Powder Catalysts*; PhD thesis, Department of Biology, Chemistry and Pharmacy of Freie Universität Berlin, **2008**.
- [77] R. A. Comelli, C. R. Vera, J. M. Parera, *J. Catal.*, **1995**, *151*(1), 96–101.
- [78] D. Spielbauer, G. A. H. Mekhemer 1, E. Bosch, H. Knözinger, *Catal. Lett.*, **1996**, *36*(1-2), 59–68.
- [79] B. Li, R. D. Gonzalez, *Catal. Today*, **1998**, *46*(1), 55–67.
- [80] C. Li, P. Stair, *Catal. Lett.*, **1996**, *36*(3-4), 119–123.
- [81] K. Ebitani, J. Tsuji, H. Hattori, H. Kita, *J. Catal.*, **1992**, *135*(2), 609–617.
- [82] F. Garin, D. Andriamasindoro, A. Abdulsamad, J. Sommer, *J. Catal.*, **1991**, *131*(1), 199–203.
- [83] K. B. Fogash, Z. Hong and J. A. Dumesic, *Catal. Lett.*, **1998**, *56*(2-3), 85–93.
- [84] M.-T. Tran, N. S. Gnep, M. Guisnet, P. Nascimento, *Catal. Lett.*, **1997**, *47*(1), 57–61.
- [85] A. Sayari, Y. Yang, X. Song, *J. Catal.*, **1997**, *167*(2), 346–353.
- [86] S. R. Vaudagna, R. A. Comelliand, N. S.Figoli, *Catal. Lett.*, **1997**, *47*(3-4), 259–264.
- [87] S. J. Gregg, K. S. W. Sing, *Adsorption, surface area and porosity*; Academic Press Inc., 1982.
- [88] K. K. Unger, J. Rouquerol, K. S. W. Sing, H. Kral, *Characterisation of pourous solids*; Elsevier science publishing company, 1988.
- [89] K. K. Unger, G. Kreysa, J. P. Baselt, *Characterisation of pourous solids V*; Elsevier science publishing company, 2000.
- [90] E. Barrett, L. Joyner, P.Halenda, *J. Am. Chem. Soc.*, **1951**, *73*, 373.

- 
- [91] K. K. Aligizaki, *Pore structure of cement based materials*; Taylor and Francis, 2006.
- [92] S. Brunauer, P. H. Emmet, E. Teller, *J. Am. Chem. Soc.*, **1938**, pages 309–319.
- [93] B. E. Warren, *X-ray diffraction*; New York: Dover Publications, 1990.
- [94] F. Sánchez-Bajo, A. L. Ortiz, F. L. Cumbreira, *Acta Materialia*, **2006**, *54*, 1–10.
- [95] F. Sánchez-Bajo, A. L. Ortiz, F. L. Cumbreira, *Appl. Phys. A*, **2009**, *94*, 189–194.
- [96] A. Corma, V. Fornés, M. I. Juan-Rajadell, J. M. López Nieto, *Appl. Catal. A: General*, **1994**, *116*(1-2), 151–163.
- [97] A. Platon, W. Thomson, *Ind. Eng. Chem. Res*, **2003**, *42*(24), 5988–5992.
- [98] D. Spielbauer, G. Mekhemer, M. Zaki, H. Knözinger, *Catal. Lett.*, **1996**, *40*(1-2), 71–79.
- [99] J. J. Carberry, *Chemical and catalytical reaction engeneering*; Dover Publications, 2001.
- [100] C. Breitkopf, H. Papp, X. Li, R. Olindo, J. A. Lercher, R. Lloyd, S. Wrabetz, F. C. Jentoft, K. Meinel, S. Forster, K.-M. Schindler, H. Neddermeyer, W. Widdra, A. Hofmanne, J. Sauer, *Phys. Chem. Chem. Phys.*, **2007**, *9*(27), 3600–3618.
- [101] X. Li, K. Nagaoka, R. Olindo, X. Li, J. Lercher, *J. Cat.*, **2006**, *238*(1), 39–45.
- [102] P. Canton, R. Olindo, F. Pinna, G. Strukul, P. Riello, M. Meneghetti, G. Cerrato, C. Morterra, A. Benedetti, *Chem. Mat.*, **2001**, *13*(5), 1634–1641.
- [103] S. Wrabetz; *Struktur-Aktivitäts-Verhältnis von rutheniumausgetauschten NaY-Zeolithen*; PhD thesis, TU Berlin, **1999**.
- [104] B. Klose; *Skeletal Isomerization of Butane by Sulfated Zirconia Catalysts -A Branched Field*; PhD thesis, Fakultät II -Mathematik und Naturwissenschaften - der Technischen Universität Berlin, **2005**.

- [105] V. Bolis, G. Magnacca, G. Cerrato, C. Morterra, *Langmuir*, **1997**, *13*(5), 888–894.
- [106] L. K. Dash, N. Vast, P. Baranek, M.-C. Cheynet, L. Reining, *Phys. Rev. B*, **2004**, *70*, 245116–245116.
- [107] C. Morterra, G. Cerrato, M. Signoretto, *Catal. Lett.*, **1996**, *41*(1-2), 101–109.
- [108] C. Morterra, G. Cerrato, F. Pinna, M. Signoretto, *J. Phys. Chem.*, **1994**, *98*(47), 12373–12381.
- [109] C. Breitkopf, S. Matysik, H. Papp, *Appl. Catal. A: General*, **2006**, *301*(1), 1–8.
- [110] O. V. Manoilova, R. Olindo, C. O. Areán, J. A. Lercher, *Catal. Comm.*, **2007**, *8*, 865–870.
- [111] M. Yashima, N. Ishizawa, M. Yoshimura, *J. Am. Ceram. Soc.*, **1992**, *75*(6), 1550–1557.
- [112] R. L. Keiter J. E. Huheyy, E. A. Keiter, *Inorganic chemistry: Principles of structure and reactivity*; 1993.
- [113] R. D. Shannon, *Acta Cryst.*, **1976**, *A32*, 751–767.
- [114] M. Rezaei, S. M. Alavi, S. Sahebdehfar, Zi-Feng Yan, H. Teunissen, J. H. Jacobsen, J. Sehested, *J. Mater. Sci.*, **2007**, *42*, 1228–1237.
- [115] K. J. Range, A. Gietl, U. Klement, K.G. Lange, *Z. Kristallogr.*, **1993**, *208*, 95–96.
- [116] K. J. Range, K. G. Lange, A. Gietl, *Journal of the Less-Common Metals*, **1990**, *158*, 137–145.
- [117] C. Morterra, E. Garrone, V. Bolis, B. Fubini, *Spect. Acta*, **1987**, *43A*, *12*, 1577–1581.
- [118] G. V. A. Martins, G. Berlier, C. Bisio, S. Colucca, H. O. Pastore, L. Marchese, *J. Phys. Chem. C*, **2008**, *112*, 7193–7200.

- [119] S. Wrabetz, X. Yang, G. Tzolova-Müller, R. Schlögl, F. C. Jentoft, *J. Catal.*, **2010**, *269*, 351–358.
- [120] C. Zhang, R. Miranda, B. H. Davis, *Catal. Lett.*, **1994**, *29*(3-4), 349–359.

## Contributions at conferences

### Presentations

#### **Crystallization of sulfated zirconia nanoparticles**

N. Giliard, F. Girgsdies, F. C. Jentoft, R. Schlögl, *86. Jahrestagung der deutschen Mineralogischen Gesellschaft*, September 14-17, 2008, Berlin, Germany

#### **Evolution of an active catalyst material during thermal treatment**

N. Giliard, F. Girgsdies, G. Lolli, M. Behrens, R. Schlögl, F.C. Jentoft, *North American catalysis society meeting*, June 7 to 12, 2009, San Francisco, USA

#### **TEM Investigation of Defect-Rich Sulfated Zirconia: Structure-Performance Relations**

N. Giliard, I. Kasatkin, F. C. Jentoft, M. Behrens, R. Schlögl, *EuropaCat IX*, August 30-September 4, 2009, Salamanca, Spain

### Poster

#### **Highly active and stable Pt-doped Mn-promoted sulfated zirconia isomerization catalysts**

N. Hensel (Giliard), F. C. Jentoft, A. Ghosh, J. A. Lercher, *41. Jahrestreffen deutscher Katalytiker*, February 27-29, 2008, Weimar/Germany

#### **Transformations during calcination of sulfated zirconia catalysts**

N. Giliard, F. C. Jentoft, R. Schlögl, *IDECAT conference on catalysis*, May 31-June 05, 2008, Porquerolles, France

#### **Optimization of the calcination procedure of sulfated zirconia**

N. Giliard, G. Lolli, F. Girgsdies, F. C. Jentoft, M. Behrens, R. Schlögl, *42. Jahrestreffen deutscher Katalytiker*, March 11-13, 2009, Weimar/Germany

#### **Investigations of highly active defect-rich sulfated zirconia**

N. Giliard, I. Kasatkin, F. Girgsdies, M. Behrens, F. C. Jentoft, R. Schlögl, *IDECAT conference on catalysis*, May 19-24, 2009, Porquerolles, France

#### **Thulium promoted sulfated zirconia - bulk versus surface influences on the catalytic performance**

N. Giliard, I. Kasatkin, F. Girgsdies, L. Yao, M. Behrens, J. Kröhnert, F. C. Jentoft, R. Schlögl, September 6-8, 2010, Messina, Italy

## **Danksagung**

Zunächst möchte ich mich bei den drei Gutachtern dieser Arbeit bedanken: Prof. Dr. Robert Schlögl für die interessante wissenschaftliche Fragestellung, die mit dieser Arbeit verbunden war und den vielen entscheidenden Anregungen. Bei Prof. Dr. Martin Lerch bedanke ich mich für seine Unterstützung, die Möglichkeit zur Durchführung von Quenchexperimenten in seinem Arbeitskreis, hilfreiche Diskussionen und die Übernahme des Zweitgutachtens. PD Dr. Thomas Schedel-Niedrig danke ich für die schnelle Übernahme des externen Gutachtens, Prof. Dr. Reinhard Schomäcker danke ich für die Übernahme des Prüfungsvorsitzes.

Prof. Dr. Friederike Jentoft danke ich für ihre fachliche Betreuung und die weit reichenden Freiheiten bei der Durchführung der experimentellen Arbeiten, vielen Dank nach Oklahoma. Ferner gilt mein herzlicher Dank Dr. Malte Behrens für die tatkräftige und kompetente Unterstützung, hilfreichen Diskussionen und das Korrekturlesen.

Herzlichen Dank an Stefanie Kühl für XRD Messungen, die Einarbeitung in den Lab-Max, die tatkräftige Unterstützung während meiner Schwangerschaft und Elternzeit sowie das Korrekturlesen. Besonderer Dank gilt ihr für die Unterstützung beim Kampf gegen Latex. Bei Dr. Frank Girgsdies bedanke ich mich für die XRD-Messungen und vielen Hilfestellungen zur Interpretation von XRD-Messdaten, Edith Kitzelmann für TG-MS Experimente. Beiden danke ich für die angenehme, ruhige Arbeitsatmosphäre in unserem gemeinsamen Büro. Igor Kasatkin danke ich für seine detaillierten HRTEM-Untersuchungen, die Defektberechnungen sowie für die zahlreichen, anregenden Diskussionen, herzlichen Dank nach St. Petersburg. Bei Lénárd-Istvan Csepei bedanke ich mich für Erstellung des Konzeptes der Berechnung der Desaktivierungskonstante, für zahlreiche Diskussionen und die Geduld, die er mit mir hatte. Jutta Kröhnert danke ich für unermüdliche IR-Messungen und deren Auswertungen, die mit vielen Diskussionen und regelmäßigen Überarbeitungen verbunden waren. Bei Christoph Rödel bedanke ich mich für seine tatkräftige Unterstützung bei der Durchführung der Quenching Experimente. Daniel Brennecke danke ich für seine Unterstützung im Labor während meiner Schwangerschaft, Lide Yao für seine TEM-Übersichtsbilder, Gisela Lorenz für BET-Messungen und ihre unvergleichlich erfrischende Art, Giulio Lolli für UV/vis-Messungen, Unterstützung beim Reaktorbau und Diskussionen, Gisela Weinberg für SEM-Bilder, Olaf Timpe für Diskussionen, Julia Engelschalt, Edward Kunkes und Neil Hamilton für Englischkorrekturen.

An der TU-München bedanke ich mich bei Xuebing Li für Diskussionen und die Durchführung von Ionenchromatographiemessungen sowie bei Lin Lin und Hui Shi für deren praktische Ausführung. Des Weiteren bedanke ich mich bei allen anderen, nicht namentlich genannten Mitarbeitern des Fritz-Haber-Instituts die mir mit Rat und Tat zur Seite standen.

Meinem Mann Tim danke ich für seine tatkräftige Unterstützung und seine Liebe, meinen Eltern und Schwiegereltern danke ich für verlässliche, stetige Babysitterdienste und Unterstützung, ohne die die Erstellung dieser Arbeit nicht möglich gewesen wäre.





## Curriculum Vitae

### Persönliche Informationen

Geboren am 26.03.1979 in Berlin, verheiratet, ein Sohn

### Ausbildung

#### Seit 03/2006

Promotion und Arbeit am Fritz-Haber-Institut (FHI) der Max-Planck-Gesellschaft in Berlin und der Technischen Universität Berlin, Fachgebiet Festkörperchemie, Thema: „Synthese und Charakterisierung von Zirkoniumdioxidkatalysatoren“.

- Von 2007 bis 2009 Gleichstellungsbeauftragte am FHI
- Von 09/2009 bis 08/2010 in Elternzeit

#### 2005 bis 2006

Arbeit am Fritz-Haber-Institut der Max-Planck-Gesellschaft in Berlin, Abteilung Chemische Physik, Präparation von Probenoberflächen für die Untersuchung von Modellsystemen mit Tieftemperatur-Rastertunnelmikroskopie und -spektroskopie.

#### 2004 bis 2005

Diplomarbeit in der Angewandten Mineralogie der TUB in Zusammenarbeit mit dem GFZ Potsdam.

Thema: „Experimentelle Untersuchungen zur Stabilität und Mischkristallbildung im System  $\text{SiO}_2$ - $\text{AlPO}_4$ “

#### 1998 bis 2005

Studium an der Technischen Universität Berlin mit Abschluss als Dipl.-Ing. für Geoingenieurwissenschaften Hauptvertiefungsrichtung: Angewandte Mineralogie

#### 2000 bis 2004

Tutorin bei Prof. Franz im Bereich Petrologie und Frau Prof. Abs-Wurmbach im Bereich Mineralogie am Fachbereich Angewandte Geowissenschaften der Technischen Universität Berlin. Abhalten von Übungen, Vorbereitung von Vorlesungen, Hausaufgabenkorrektur, Prüfungsvorbereitung, Pflege der Lehrsammlungen, Studierendenbetreuung